Master's thesis

Electrical detection study of inverse spin Hall effect induced by spin pumping

by

Yuriy Aleksandrov

from

Targovishte

March 2012

Contents

List of Figures

List of Tables

Abstract

Spintronics is devoted to the investigation of electronic transport manipulation by means of the electronic spin. In spintronics, the spin-Hall effect and its reciprocal, the inverse spin-Hall effect (ISHE), is of crucial importance since these effects allow the mutual conversion between a charge current and a spin current.

Recently, a strong mutual interaction between magnetization dynamics and spin polarized electronic transport has been shown and investigated. It has been predicted and later experimentally proven that the spin polarized current can drive magnetization dynamics via a spin torque mechanism, and that in the reciprocal process, resonant magnetization dynamics can lead to a generation of spin current which is related to the spin pumping mechanism - the spintronic analog of a battery in conventional electronics-.

In this work, we have investigated the ISHE induced by spin pumping in a simple ferromagnetic/paramagnetic bilayer system ($Ni_{81}Fe_{19}/Pt$). Spin pumping driven by ferromagnetic resonance injects a spin current through the ferromagnetic/paramagnetic interface into the paramagnetic layer. This spin current gives rise to a transverse electromotive force (V_{ISHE}) perpendicular to the applied magnetic field and the microwave field. The electromotive force is created by the ISHE which is defined by the spin orbit interaction in the paramagnetic layer. In other words, the ISHE is a mechanism which converts a spin current into a charge current.

We have fabricated several Py films with and without Pt capping layers on a thermally oxidized Si substrate by using either electron beam lithography or metal mask and evaporating by electron beam. We performed ferromagnetic resonance (FMR) measurements a observed the FMR linewidth enhancement for the samples with Pt capping layers. FMR linewidth enhancement is partly due to the transfer of angular momentum from the precessing local spins to the conduction electrons. This is the generation of a spin current by the spin pumping mechanism. We have developed several experimental setups and sample holders to measure and observe the variation of V_{ISHE}. We observed that the electromotive force varies systematically by changing the microwave power and frequency, magnetic-field angle, and temperature; being consistent with the prediction based on the Landau–Lifshitz–Gilbert equation combined with the models of the ISHE and spin pumping.

elektrische Detektion des inversen Spin Hall Effektes hervorgerufen durch Spin Pumping

Die Spintrokik widmet sich der Untersuchung der Manipulation des elektronischen Transports mittels des elektronischen Spins. In der Spintronik sind der Spin Hall Effekt (SHE) und der inversen Spin Hall Effekt (ISHE) von entscheidender Wichtigkeit. Diese Effekte ermöglichen die wechselseitige Konvertierung zwischen einem Ladungstrom und einem Spinstrom. Vor kurzem wurde eine starke wechselseitige Interaktion zwischen der Magnetisierungsdynamik und polarisertem elektronischem Transport gezeigt und untersucht. Es wurde vorausgesagt und experimental bewiesen, dass ein spinpolarisierter Strom die Magnetisierungsdynamik über einen Spindrehmomentmechanismus beinflussen kann und das im gegenseitigen Prozess die resonante Magnetisierungsdynamik zur Erzeugung eines Spinstroms führen kann. Dies ist mit dem Spin Pumping Mechanismus verbunden.

In dieser Arbeit haben wir den durch Spin Pumping induzierten ISHE in einem einfachen 2-Schichtsystem aus einem Ferromagneten und einem Paramagneten untersucht. Der Ferromagnet wurde durch eine Permalloyschicht gebildet und der Paramegnet durch eine Platinschicht. Ein Spinstrom wird dabei durch die Grenzschicht vom Ferromagneten in den Paramagneten mittels spin pumping induziert. Als Antrieb für den spin pump Prozess dient die ferromagnetische Resonanz, welche durch ein Mikrowellenfeld geeigneter Frequenz im GHz-Bereich angeregt wird. Der Spinstrom verursacht eine transveral elektromotorische Kraft V_{ISHE} senkrecht zu einem extern angelegten magnetischen Feld und dem Mikrowellenfeld. Diese elektromotorische Kraft wird durch den ISHE hervorgerufen, welcher widerum die Spin-Bahn-Wechselwirkung in der paramagnetischen Schicht als Ursache hat. Mit anderen Worten, der ISHE ist ein Mechanismus welhcer einen Spinstrom in einen Ladungstrom umwandelt.

In der Arbeit wurden mehrere Py Filme mit und ohne Pt Deckschichten auf einem termisch oxidierten Si-Substrat hergestellt. Dazu wurden sowohl Elektronenstrahllitographie als auch Metallmasken in Kombination mit Elektronenstrahlverdampfung verwendet. Es wurden an allen Proben Untersuchungen mittels winkelabhängiger Ferromagnetischer Resonanz durchgeführt. An den Proben mit Pt-Abdeckschicht wurde eine Erhöhung der Linienbreite des Resonanzsignals im Vergleich zu den nicht abgedeckten Proben beobachtet. Die Erhöhung der FMR Linienbreite ist zum Teil auf eine Übertragung des Drehmomentes der präzedierenden lokalen Spins auf Leitungselektronen zurück zu führen, was der Erzeugung eines Spinstroms durch den Spin-Pumpmechanismus entspricht. Es wurden verschiedene experimentelle Aufbauten und Probenhalter für die Messung und Beobachtung entwickelt. Es wurde festgestellt, dass die elektromotorische Kraft systematisch varriert, wenn die Mikrowellenleistung, die Frequenz, der Orientierung des externen Magnetfeldes zur Probe und die Temperatur variiert wird. Dies ist in Einklang mit der Landau Lifschitz Gilbert Gleichung unter Berücksichtigung der Modelle des ISHE und des spin pump Prozess.

1 Introduction

1.1 Motivation and objectives

In today's electronics, information in semiconductor electronic devices and data storage technologies is mainly transported and manipulated by charge currents. With integrating more amounts of transistors in the same space, heat dissipation and power consumption become significant handicaps to further technological developments [27]. In a hard disk, for example, large currents are used to generate magnetic fields to switch the magnetization of the nano-regions on which binary data are stored. Continuing miniaturization of storage is a challenging task because the reduction in particle volume must be compensated by an increase in its magnetic anisotropy, to prevent undesirable switching by thermal fluctuations. However, the consequence of that is larger fields, and therefore larger currents, are needed for writing. The search for alternative technologies that solve or at least ease these problems are among today's very hot research topics. One of the most promising candidate to replace existing charge-based technologies is based on using spin currents which is called as spintronics [5]. The new development of spintronics aims at utilizing the spin degree of freedom for electronic applications such as the generation, manipulation, and detection of a spin current.

Spintronics mainly deals with two current types: the spin polarized current and pure spin current. In this study, we are emphasizing the latter one. Pure spin current, a directed flow of angular momentum that are not accompanied by a net charge current, offer several advantages in applications, such as less power dissipation, absence of stray Oersted fields, and decoupling of spin and charge noise [20]. Pure spin currents can be created by spin pumping from a precessing ferromagnet.

Through th spintronics researches, great theoretical and experimental interests have been focused on the spin-Hall effect[19, 47, 14], which refers to the generation of spin currents from charge currents via the spin-orbit interaction. The SHE couples a spin current with a charge current in a solid, and thus is crucial for the integration of spin-current

technology into conventional electronics based on a charge current [3]. The spin-orbit interaction responsible for the SHE is also expected to cause the inverse process of the SHE: the inverse spin-Hall effect (ISHE), a process that converts a spin current into an electric current.

In this work, we study the spin-pumping-induced electrical voltage due to the inverse spin Hall effect in a ferromagnetic/paramagnetic metal bilayer system, namely, the Py/Pt bilayer. The spin pumping mechanism requires only a simple ferromagnetic-paramagnetic system, and this simplicity makes it a very important tool for exploring spin currents in a wide range of materials and for developing future spintronic devices [4]. The cycle generating the ISHE voltage works as follows: The magnetization precession excited by the applied microwave injects a pure dc spin current with a spin polarization σ, parallel to the magnetization precession-axis, into the paramagnetic layer under the FMR condition. In other words, the magnetization of the ferromagnetic layer is driven into ferromagnetic resonance (FMR) and can relax by emitting a spin current into the adjacent normal-metal layer. This injected spin current is converted into a dc electric voltage using the inverse spin-Hall effect (ISHE) in the paramagnetic layer and can be detected electrically by measuring the electric voltage between the electrodes attached to the both ends of Pt layer. We systematically measured this dc voltage induced by spin pumping together with the inverse spin Hall effect as a function of angle of the applied magnetic field direction; as well as the microwave frequency and power. We have also investigated the temprature dependence of the induced electric voltage.

1.2 Overview

Chapter 2 begins with a brief introduction to the theory of magnetization dynamics and ferromagnetic resonance. After magnetization dynamics is introduced, the spin pumping mechanism driven by ferromagnetic resonance is discussed. Finally, with spin Hall effect and inverse spin Hall effect we complete the cycle of generation and detection of electric current induced by spin pumping in a ferromagnetic-paramagnetic metallic system.

Chapter 3 covers the sample preparation steps and related techniques. In this chapter, the experimental setups which were developed for this work are also presented, including a new sample stage and holders as well the waveguide-Microwave-cable assembly which allowed us to measure the electrical signal by inserting the leads wire into the microwave

cavity.

In chapter 4, the experimental results are shown and discussed. These comprise the observation of the systematic variation of V_{ISHE} as a function of the microwave power and frequency, magnetic-field angle, and temperature.

2 Theoretical Background

2.1 The magnetization dynamics and ferromagnetic resonance

In paramagnetic isolators, for atoms in the presence of an external magnetic field, the degeneracy of energy levels is lifted with regard to spin and orbital quantum numbers. This displacement of the energy levels gives the multiplet splitting of the spectral lines which are called Zeeman multiplets. Each energy level is split into $2j + 1$ levels, corresponding to the possible values of m_j. The level splitting (the energy shift) relative to the position of the unsplitted energy level, can be written

$$\Delta E = gm_j \left(\frac{e\hbar\mathbf{B}}{2m_e} \right) = gm_j\mu_B\mathbf{B} \tag{2.1}$$

where g, called the Landé g factor, μ_B the Bohr magneton and $\mathbf{B}$ the magnetic field. The electron paramagnetic resonance (EPR) monitors the transition between adjacent levels. In ferro and ferrimagnetic materials the exchange interaction between neighboring spins leads to a collective excitation of the spin system called spin waves or magnons. This is called ferromagnetic resonance (FMR). FMR is basically the precession of the materials magnetization $\mathbf{M}$ about a static effective magnetic field $\mathbf{B}_{eff}$. In this thesis, the magnetic induction $\mathbf{B} = \mu_0\mathbf{H}$ refers to the magnetic field. $\mathbf{B}_{eff}$ includes not only the external field $\mathbf{B}_{ext}$ but also the inner fields which are caused by the electron spin system. Due to the spin-orbit interaction, the spin system is coupled to the lattice. Thus, $\mathbf{B}_{eff}$ differs in magnitude and direction from the external field.

In a ferromagnetic material, below the Curie temperature, the unpaired electron spins are coupled by the exchange interaction for the energetically favourable parallel alignment. The superposition of these individual spin magnetic moments create the magnetization of body. The basic theory of FMR was developed by Landau and Lifshitz in 1935 [23]. Before starting with the equation of motion of magnetization, we start with the torque $\mathbf{T}$ which is exerted by an effective magnetic field. The total magnetic moment of the

body $\mathbf{m} = V\mathbf{M}$, where V is the volume of the the magnetic solid, experiences a torque $\mathbf{T} = \mathbf{m} \times \mathbf{B}_{eff}$ when $\mathbf{m}$ and $\mathbf{B}_{eff}$ are not parallel. $\mathbf{T}$ is an axial vector perpendicular to both magnetic moment $\mathbf{m}$ and field $\mathbf{B}_{eff}$ with units [Nm]. According to Newton's classical equation of motion, the torque causes the vector of angular momentum $\mathbf{L}$ to precess

$$\frac{d\mathbf{L}}{dt} = \mathbf{T} = \mathbf{m} \times \mathbf{B}_{eff}. \tag{2.2}$$

2.1.1 Precession of moments

The relationship between $\mathbf{m}$ and the angular moment $\mathbf{L}$ is written in terms of the gyromagnetic ratio γ as $\mathbf{m} = \gamma\mathbf{L}$, where $\mathbf{L}$ is given in units of $[Nms]$. The gyromagnetic ratio is written as $\gamma = \frac{g\mu_B}{\hbar}$. By using $\mathbf{m} = \gamma\mathbf{L}$, one can obtain the equation of motion for the free, undamped precession of the magnetization about an effective magnetic field $\mathbf{B}_{eff}$ as

$$\frac{d\mathbf{m}}{dt} = -\gamma[\mathbf{m} \times \mathbf{B}_{eff}]. \tag{2.3}$$

The gyromagnetic ratio leads to the Larmor precession of $\mathbf{m}$ about the magnetic field $\mathbf{B}_{eff}$ at the angular frequency $\omega = \gamma\mathbf{B}_{eff}$. It is now possible to derive the Larmor precession frequency from equation 2.3. The magnetization can precess about $\mathbf{B}_{eff}$ only when $\mathbf{m}$ has a component perpendicular to the field. The precession frequency does not depend on the angle between the magnetic field and the magnetic moment. This yields that ω is independent of the component of the magnetic moment perpendicular to the axis of precession.

The precession-cone angle θ, between $\mathbf{B}_{eff}$ and $\mathbf{m}$, and the magnitude of $\mathbf{m}$ does not change during the precession. Therefore, the energy $E = -\mathbf{m} \cdot \mathbf{B}_{eff} = -mB_{eff}\cos\theta$ is constant and not at its minimum state. This contradicts with experience, since after sufficient time the magnetization will turn to the direction of the field, as shown in Fig. 2.1. To achieve this damping, an additional torque is needed which is perpendicular to $\mathbf{m}$ and $\mathbf{T}$. This additional torque $\mathbf{T_D}$, is given by

$$\mathbf{T}_D = C \left[\mathbf{m} \times \frac{d\mathbf{m}}{dt} \right], \tag{2.4}$$

where C is a phenomenological constant, similar to a friction coefficient in linear motion. The damping torque causes the magnetization to precess towards the $+z$ axis. Here, the damping term describes an unspecified dissipative process in the material.
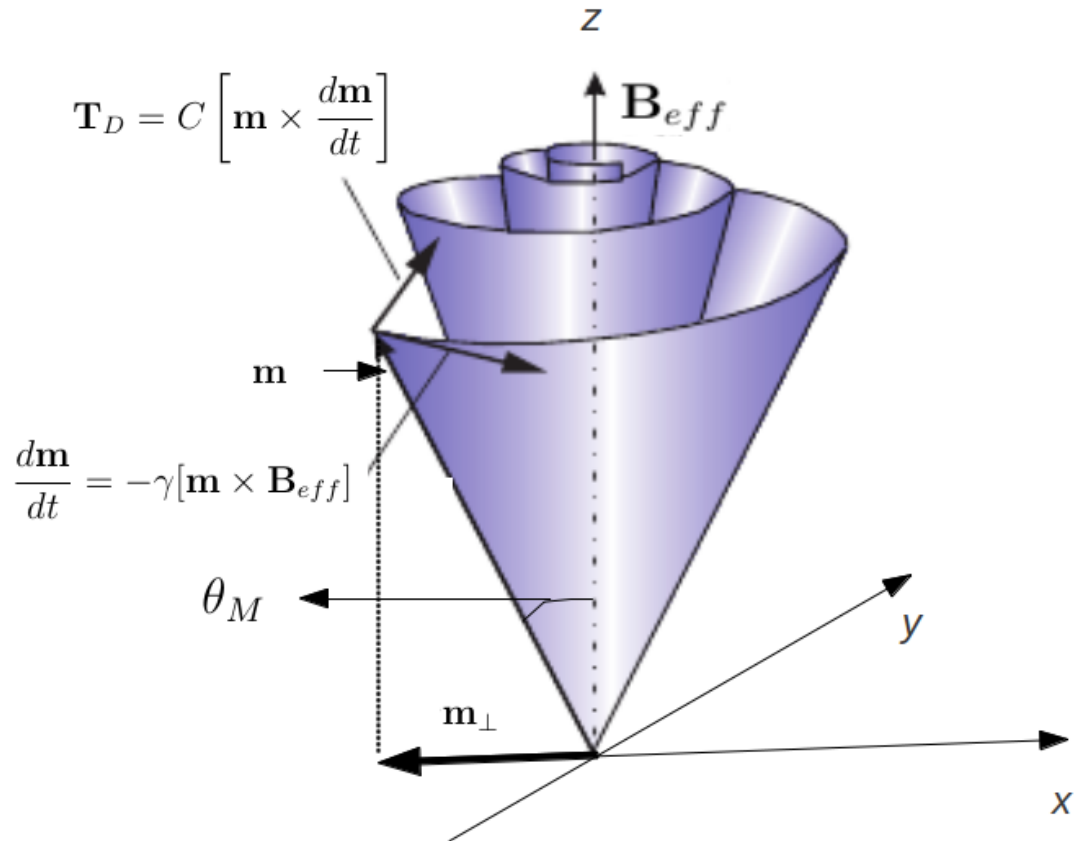
Figure 2.1: The magnetization precession with damping is depicted in the presence of $\mathbf{B}_{eff}$ in z direction. The damping torque causes the magnetization to precess towards the $+z$ axis with damping torque $\mathbf{T}_D$. The direction of movement of magnetization is given by $-[\mathbf{m} \times \mathbf{B}_{eff}]$. [38]

The realistic equation of motion for $d\mathbf{m}/dt$ which includes damping as well is called *the Landau-Lifshitz-Gilbert* (LLG) equation. The LLG equation has the form

$$\frac{d\mathbf{m}}{dt} = -\gamma[\mathbf{m} \times \mathbf{B}_{eff}] + \frac{\alpha}{|\mathbf{m}|}\left[\mathbf{m} \times \frac{d\mathbf{m}}{dt}\right], \qquad (2.5)$$

where α is the so-called damping parameter and denotes all unspecified dissipative processes. At the right side of equation 2.5, the first term describes the rotation of $\mathbf{m}$ about the field $\mathbf{B}_{eff}$ with a constant angle θ due to the torque $\mathbf{T} = \mathbf{m} \times \mathbf{B}_{eff}$ into the direction $\frac{d\mathbf{m}}{dt} = \gamma\mathbf{T}$. The second term which is the relaxation term, however describes the change of angular momentum or, shortly, the damping of the precessional motion of $\mathbf{m}$. With a positive damping parameter in a sufficient time period due to the damping torque, the magnetic moment $\mathbf{m}$ will eventually spiral into the magnetic field direction.

In order to describe the dynamics of the magnetization, one can also use *the Landau-Lifshitz-Equation*

$$(1 + \alpha^2)\frac{d\mathbf{m}}{dt} = \gamma[\mathbf{m} \times \mathbf{B}_{eff}] + \frac{\alpha\gamma}{|\mathbf{m}|}[\mathbf{m} \times (\mathbf{m} \times \mathbf{B}_{eff})], \qquad (2.6)$$

where the term $(1 + \alpha^2)$ is approximately 1 for small α.

By damping, the magnetic moment spirals into the field direction and thus changes its angular momentum. However, according to the conservation of angular momentum, this difference in angular momentum has to be transferred to some another reservoir. The flow of energy and angular momentum out of the spin system ultimately ends up in the lattice, the so called spin-lattice relaxation.

So far, the total magnetic moment was denoted as $\mathbf{m}$ with a constant absolute value $|\mathbf{m}|$. The LL and LLG equations are valid only in this ansatz. The LL and LLG equations describe the dynamics of a magnetic body unless the magnitude of the macromoment changes in time. This ansatz is valid for small excitations (small precession-angles) below the Suhl instability. For paramagnetic materials without exchange interaction, this dephasing of magnetization is considered by an additional time constant. This case is described by the Bloch-equation [8].

In ferromagnetic resonance measurements, the applied static magnetic field $\mathbf{B}_{dc}$ causes the total magnetic moment to precess with a Larmor frequency around the direction of the local field $\mathbf{B}_{eff}$. If the sample is exposed with a transverse microwave field b_{MW},

and if the microwave frequency matches the Larmor frequency, the resonance condition is fulfilled, and the microwave power is absorbed by the sample.

More details on resonance conditions and magnetization dynamics in thin films is given in section 2.4.

2.2 Spin pumping in ferromagnetic resonance

An electron carries elementary charge e. Coherent motion of electrons may circulate an electric current, which can transport energy and information. Although electrons also hold intrinsic spins, the spin orientations of the charge carriers in traditional electronic devices are completely random. It does not show any spin related effect. Today, conventional electronic devices ignore the spin property of the electron, but new devices are now being built that rely on the spin currents [48]. In order to understand what a spin current is, the electron current can be considered as one which flows through a channel and contains only up-spin polarized electrons. After adding to this a similar current in which all electrons are down-spin polarized flowing in the opposite direction, the result is a current of spins only; thus there is no net particle transfer across any cross section of the channel.

The spin current is a movement of spins in a system, and it is a vector flow (see Fig. 2.2). A vector flow includes two quantities: the linear velocity $\vec{\nu}(r,t)$ and the angular velocity $\vec{\omega}(r,t)$, in order to describe the translational and rotational motions, respectively [42]. Here a magnetic moment with its magnitude $|\vec{m}|$ is the quantity that is transported and is constant in time. By using the linear and angular velocities, the translational motion and the rotational motion of the classical vector $\vec{m}$ is described as $j_s = \vec{\nu}\vec{m}$ and $\vec{j}_\omega = \vec{\omega} \times \vec{m}$ respectively. j_s and $\vec{j}_\omega$ are named as linear and angular current densities . In order to describe the scalar flow such as charge, one local current $\vec{j}_s(\mathbf{r},t)$ is sufficient, because, the scalar quantity only has translational motion, but the vector quantity has both translational and rotational. The difference in the case of vector transport in the linear regime is that the linear vector current is not conserved. The linear spin current density $j_s(\mathbf{r},t)$ is identical to the conventional spin current. From the linear spin current density, one can calculate the linear spin current $\vec{I}_s$ flowing through the surface S as $\vec{I}_s^S = \int \int_S d\vec{S} \cdot j_s$ as shown in Fig. 2.2. However, the behavior for the angular spin current is different. From the density $\vec{j}_\omega(\mathbf{r},t)$, it is meaningless to determine how much angular spin current flows through a surface S since it is a current in angular space [42].

A spin current can induce magnetization motion through a spin transfer torque and the inverse process is also possible: a moving magnetization in a ferromagnet can emit a spin current into an adjacent conductor. This effect is the so-called spin pumping, proposed by Tserkovnyak and co-workers [45, 44]. Spin pumping is a mechanism where a pure spin current, which does not involve net charge currents, is emitted from the ferromagnet/paramagnet interface into a paramagnetic region as illustrated in Fig. 2.3.
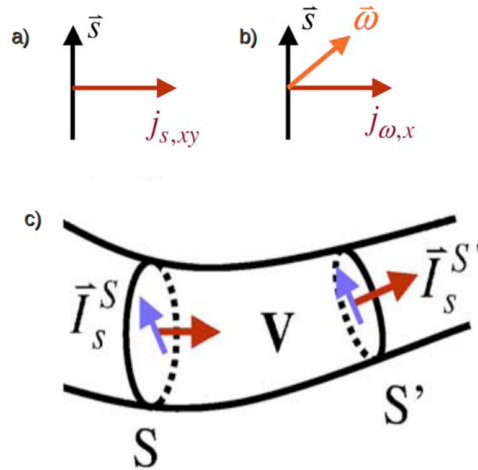
Figure 2.2: a) and b) are the schematic diagram for the translational motion and the rotational motion of the classic vector $\vec{m}$, respectively. c) The spin current carried by a velocity of V in a quantum wire [42]

This has been demonstrated in ferromagnetic resonance experiments with multilayers consisting of ferromagnetic/paramagnetic (we also refer paramagnet as nonmagnet or normal-metal) thin films [25] to appear as an enhancement of the Gilbert damping constant in magnetization dynamics. It was suggested that the mechanism behind the enhanced damping was due to a spin current pumped from the ferromagnet into the normal metal, since the pumped current corresponds to an angular momentum or a spin torque transfer to a paramagnetic reservoir [44].

According to the Stoner model, at equilibrium in a ferromagnetic body F, there is a large population of spins in the direction of magnetization than antiparallel to it i.e., two separate bands or channels for up and down spins split by exchange energy. When the magnetization direction is changed, the bands immediately shift in energy. This is an excited state for the system, and in order to turn back to the equilibrium state there has to be spin transfer from one spin band to other (also called spin relaxation). This can either be within the ferromagnet or in the vicinity of an adjacent paramagnetic layer acting as a reservoir to which spins can be transfered into. Therefore, the spin transfer process for F is modified when it is in contact with a paramagnet, and the entire process depends on the spin relaxation properties of the paramagnet. The magnetization direction can be changed in time by putting F into FMR. Applied magnetic fields periodically change the direction of magnetization vector, thus the magnetization begins to precess. As a result, the magnetization is switched back and forth under oscillating magnetic

field and eventually emits a spin current into the paramagnetic layer through the F-N (ferromagnet-paramagnetic) interface. This process can be also seen as the polarization of conducting electrons in the paramagnetic material. Tserkovnyak has also found that in addition to the ac spin current, a dc current is also emitted [44]. The dc part of the emitted spin current plays a crucial role in spin pumping in F-N bilayer systems. The spin pumping phenomenon requires only a simple ferromagnetic/paramagnetic system, and this simplicity makes it a very important tool for exploring spin currents in a wide range of materials and for developing future spintronic devices [4].

Spin pumping can be mathematically described analogous to that of adiabatic pumping of charges in mesoscopic systems [9]. Charge and spin transport through a nanoscale condutor can be obtained in absence of a transport voltage by periodically varying in time at least two of its parameters. If the time dependence of the system is slow compared to its characteristic response time, this transport mechanism is labeled as adiabatic pumping [41]. In ferromagnetic-nonmagnetic system the pumping cycle is provided by varying the x-y component of the magnetization vector in time when the external field is applied in z-direction, which is basically the precession.

The spin current at the F-N interface I_s^{pump} pumped by the (resonant) precession of a ferromagnet magnetization into an adjacent paramagnetic metal was defined by Tserkovnyak using a scattering matrix approach [13]:

$$I_s^{pump} = \frac{\hbar}{4\pi} g_{\uparrow\downarrow} \mathbf{m} \times \frac{d\mathbf{m}}{dt}, \tag{2.7}$$

where $g_{\uparrow\downarrow}$ is the real part of the mixing conductance which is a dimensionless quantity, and $\mathbf{m}$ is used as a unit vector which represents the magnetization direction. The mixing conductance is a material parameter and describes the spin transport at the interface that is noncollinear to the magnetization direction and is proportional to the torque acting on the ferromagnet in the presence of a noncollinear spin accumulation in the normal metal [13]. The spin current I_s^{pump} produced by spin pumping at the interface is perpendicular both to the magnetization direction $\mathbf{m}$ and to the change of $\mathbf{m}$ in time, $d\mathbf{m}/dt$ (see Fig. 2.3). It should be noted that this current is an instantaneous description of the current being emitted. The vector $\mathbf{m} \times \frac{d\mathbf{m}}{dt}$ is time dependent. However, the z-component of the vector product which is along the steady-state magnetization direction is constant and gives rise to the dc part of I_s^{pump} and propagates into N normal to the interface. The ac part of the spin current vanishes due to dephasing of spins in a very short distance from the interface. It is schematically depicted in Fig. 2.3. The blue

arrows represents the dc part of I_s^{pump}.
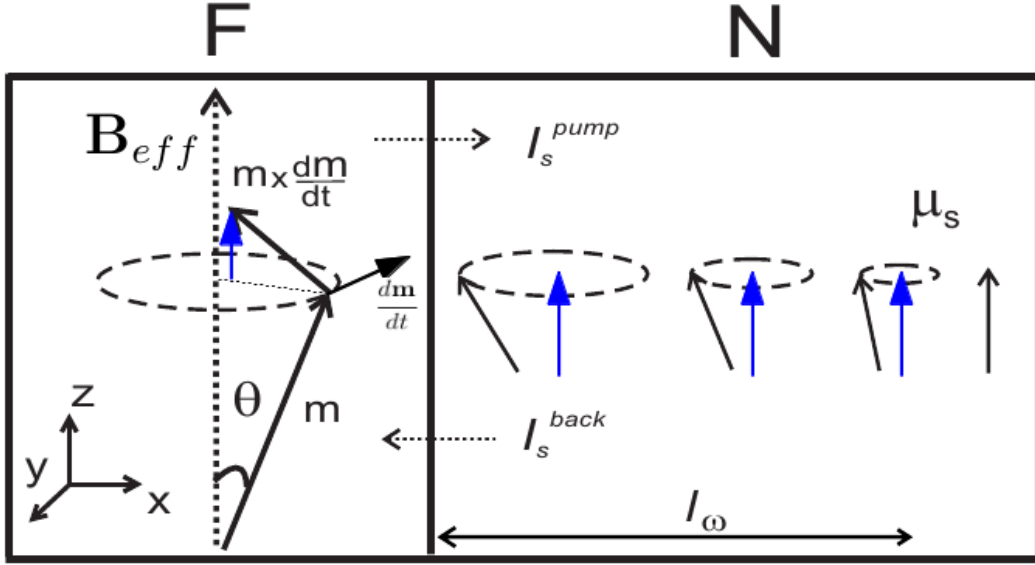
Figure 2.3: The F/N structure in which the resonant precession of the magnetization direction **m** pumps a spin current Is pump into N. A spin accumulation μ_s might also be built up in N and that drives a spin current I_s^{back} back into the F. The parallel component of I_s^{back} to **m** can enter into F whereas perpendicular component dissipates at interface. [13]

According to the spin-related properties of the nonmagnetic layer, the incoming spin current is reacted in two different ways. The first way is the case that the paramagnetic layer is a perfect spin sink. If the spin relaxation (spin flip) time τ_N of the spins in paramagnetic layer is smaller than the magnetization precession period $2\pi/\omega$, which is also the period of spin pumping, the generated spin current diffuses into the paramagnetic layer and dissipates within the spin diffusion length, l_{sd}. The relaxation of the spin current in the nonmagnetic layer corresponds to a loss of angular momentum in the ferromagnetic layer and results in an increase in the effective Gilbert damping of the magnetization precession. The pumped current to the interface can be calculated in an adiabatic approximation, since the period of precession $2\pi/\omega$ is typically much larger than the relaxation times [44]. The opposite regime is the case that the spin relaxation time is longer than the magnetization precession period $2\pi/\omega$. In this case, the time for relaxation is not short enough, and thus, the spin injection rate is greater than the dissipation rate. This situation gives rise to a net local spin accumulation μ_s on the nonmagnetic layer. The produced spin accumulation has to diffuse. The diffusion can either be into the nonmagnet or back to the ferromagnet. The latter is called the back-flow current I_s^{back} and is given by [13],

$$I_s^{back} = \frac{g_{eff}^{\uparrow\downarrow}}{2\pi N}[\mu_{\mathbf{s}} - \mathbf{m}(\mathbf{m} \cdot \mu_{\mathbf{s}})], \qquad (2.8)$$

where N represents the one-spin density of states, and $\mu_{\mathbf{s}} = \hbar\omega$. Here instead of $g^{\uparrow\downarrow}$, $g_{eff}^{\uparrow\downarrow}$ is used because in vicinity of back-flow current, the mixing conductance has to be normalized.

The difference in the damping parameter is determined by the FMR linewidth for ferromagnetic samples without capping layer and for the samples in which the capping paramagnetic layer is sufficiently thick to fully dissipate the pumped magnetic moment. The enhancement of damping is attributed to the loss of spin momentum in F due to relaxation of the spin accumulation in N. Therefore, the additional damping is the quantity which normalizes $g_{eff}^{\uparrow\downarrow}$. The effective mixing conductance can be experimentally calculated from the FMR spectra as [28],

$$g_{eff}^{\uparrow\downarrow} = \frac{4\pi\gamma M_s t_F}{g\mu_B \omega_f}(\Delta H_{F/N} - \Delta H_F), \qquad (2.9)$$

where t_F is the thickness of F layer, M_s is the saturation magnetization of ferromagnet, μ_B is the Bohr magneton, and ΔH is the FMR linewidth.

The spin accumulation which causes the back-flow spin current can be calculated by solving the spin diffusion equation in nonmagnetic layer[13],

$$\frac{\partial\mu_{\mathbf{s}}}{\partial t} = D_N \frac{\partial^2 \mu_{\mathbf{s}}}{\partial x^2} - \frac{\mu_{\mathbf{s}}}{\tau_N}. \qquad (2.10)$$

Here μ_s is the spin accumulation in N, τ_N is the spin flip time, and D_N is the diffusion coefficient in N.

During their propagation into the paramagnetic layer, the injected spins continue to precess in a short interface region. However, if we assume that the equilibrium magnetization in the ferromagnet points in the z-direction, precessing spins eventually loose their time dependent x-y components due to dephasing in the spin precession length $l_\omega = \sqrt{D_N/\omega}$, where ω is the precession frequency. The remaining z-component along the static magnetic field direction is constant in time. The spin diffusion length is much larger than l_ω, i.e., $\lambda_N = \sqrt{D_N/\omega} \gg l_\omega$. The dephasing leads to a time-averaged spin accumulation as $\langle\mu_{\mathbf{s}}\rangle_{\mathbf{t}} = \mu_{\mathbf{z}}\mathbf{z}$, and in N, close to the interface spin accumulation, it can be written as [13]

$$\mu_{0,z} = \hbar\omega \frac{\sin^2\theta}{\sin^2\theta + \eta}, \tag{2.11}$$

where θ is the precession cone angle, and η is a reduction factor determined by the ratio between injection time and spin-flip relaxation time.

After defining the pumped current from the ferromagnet and the back-flow current into the ferromagnet, the spin-current matching can be constructed at the interface. For the matching there are three currents with their components. First, the spin pumping current is given by [13],

$$I_{s,\perp}^{pump} = g^{\uparrow\downarrow} \sin\theta\hbar\omega. \tag{2.12}$$

The back flow current has two components parallel and perpendicular to $\mathbf{\hat{m}}$, and since the back-flow current is due to the spin accumulation, it can be written in terms of μ_0 (Note that this is a spin accumulation at the interface.) [13],

$$\begin{aligned} I_{s,\parallel}^{pump} &= g_F\mu_{0,\parallel} \\ I_{s,\perp}^{pump} &= g^{\uparrow\downarrow}\mu_{0,\perp}, \end{aligned} \tag{2.13}$$

where g_F is the conductance of the bulk ferromagnet over a spin diffusion length. The sum of equations 2.12 and 2.13 gives the total spin current at the ferromagnetic side of the interface. The missing current is the spin current on the nonmagnetic side of the system. Finally the last current can be obtained by solving the Bloch equation for the spin accumulation at N. The current at the interface reads [13]

$$I_s^N = g_\omega \begin{pmatrix} \mu_{0,x} - \mu_{0,y} \\ \mu_{0,x} + \mu_{0,y} \\ \frac{g_N}{g_\omega}\mu_{0,z} \end{pmatrix} \tag{2.14}$$

in terms of μ_0 at the interface. In this equation the z-component is determined only by the usual spin-flip process. However, for the x and y components there are two important effects. The first one is the precession, which results in mixing of the two components, depending on the time spent in N; and the second effect is the averaging which reduces the total amplitude of the components. The spin accumulation μ_0 is obtained by matching the currents at the interface, and the resulting net current at F-N

interface in this case reads $I_s^N = I_s^F = I_s^{pump} + I_s^{back}$.

Ellipticity correction

In a real magnetic thin film, the magnetization precession is not circular but elliptical. This is due to the strong demagnetizing fields, which force the magnetization into the film plane. The time-dependent precession cone angle modifies the dc component of the pumped spin current by an ellipticity correction factor P as derived and measured by Ando et al.[4]. For an in-plane equilibrium magnetization, $j_{s,dc}^{eff} = P j_{s,dc}^{circ}$ with [28],

$$P = \frac{2\omega_f(\gamma 4\pi M_s + \sqrt{(\gamma 4\pi M_s)^2 + (2\omega_f)^2})}{(\gamma 4\pi M_s)^2 + (2\omega_f)^2} \tag{2.15}$$

Modified LLG equation

According to the conservation of angular momentum, the spin torque on the ferromagnet resulting from spin pumping modifies the damping term of the Landau-Lifshitz-Gilbert equation. In other words, the interface spin current corresponds to the torque $\tau = -\mathbf{I_s}$ [45] with units $[\,\mathrm{J}\,]$ or $[\,\mathrm{Nm}\,]$. As a result, this is the source of enhancement of the resonance line-width in the FMR spectra. After including this term, in the vicinity of spin pumping through the ferromagnet-nonmagnet interface,the LLG equation for the magnetization in the ferromagnet can be written as [45],

$$\frac{d\mathbf{m}}{dt} = -\gamma \mathbf{m} \times \mathbf{B_{eff}} + \frac{\alpha_0}{|\mathbf{m}|}\left[\mathbf{m} \times \frac{d\mathbf{m}}{dt}\right] + \gamma \mathbf{I}_s, \tag{2.16}$$

where $\mathbf{I}_s$ is the total spin current and includes the back-flow current as well; $I_s = I_s^{pump} - I_s^{back}$. $\mathbf{B}_{eff}$ is the effective magnetic field and the intrinsic bulk constant α_0 is smaller than the total Gilbert damping $\alpha = \alpha_0 + \alpha'$. The additional damping constant α' is caused by the spin pumping [45].

2.3 Hall effect for charge and spin

2.3.1 Ordinary Hall effect

The ordinary Hall effect describes the generation of a voltage (Hall voltage) across a conductor transverse to an electric current under the presence of a magnetic field (see Fig. 2.4). The Hall voltage is the accumulation of the charge carriers on one side of the sample. When a magnetic field is applied, the paths of moving charges between collisions are curved because of the Lorentz force, $\mathbf{F} = q[\mathbf{E} + (\mathbf{v} \times \mathbf{B})]$. Therefore, a charge imbalance between the sample edges, perpendicular to the current and magnetic field direction is built up.
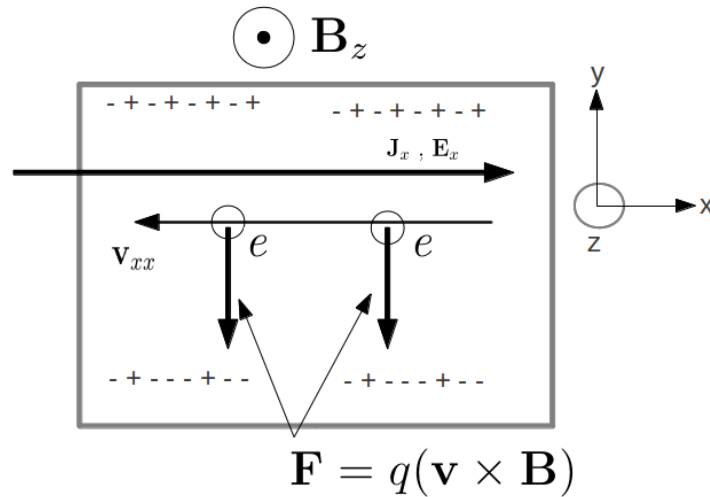
Figure 2.4: The illustration of ordinary Hall effect. The magnetic field is applied along +z axes. Due to the Lorentz force, moving negative charges bent their paths toward the sample edges.

After the discovery of the Hall Effect in 1881, Hall reported that the effect in ferromagnetic iron is ten times larger than in non-magnetic conductors. The dependence of the Hall resistivity ρ_H on a field $\mathbf{B}_z$ applied perpendicular to the sample plane is qualitatively different in ferromagnetic and non-magnetic conductors. The effect that is observed in ferromagnetic conductors is called the anomalous Hall effect (AHE). In non-magnetic materials, ρ_H increases linearly with $\mathbf{B}_z$ due to the Lorentz force. In ferromagnets, however, it increases gradually in weak magnetic fields but saturates at a large value that is nearly $\mathbf{B}_z$-independent [11].

2.3.2 Anomalous Hall effect in ferromagnetic materials

In ferromagnetic materials, the spin orbit interaction (SOI) between the spin of conduction electrons and the impurities leads to the anomalous Hall effect. In order to explain this effect, two main interaction mechanisms were suggested, i.e., skew scattering and side jump effect. As a result of these interactions incident electrons are scattered into the preferential transverse directions with respect to the incoming direction. In ferromagnetic metals, this scattering mechanism and the equilibrium polarization of the conduction electrons (due to the band structure) can lead to a potential drop transverse to an applied electric field, even in the absence of magnetic field. This effect is also called the extraordinary Hall effect. Two interaction mechanisms which causes this effect are briefly discussed below.

Skew scattering

In Fig. 2.5 at lower image the skew scattering mechanism is illustrated. Several theories have been suggested for the skew scattering. One of them suggested by Kondo[22] is based on the s-d exchange model where the conduction electrons couple to the localized spins. When a conduction electron scatters on an impurity atom with strong spin-orbit interaction, the behavior of the scattering depends on the spin orientation of the electron. The presence of the SOI results in the asymmetry of the scattering cross section, because the scattering is characterized by a difference between the probabilities of scattering to the right and to the left (the right and the left are the directions + and - of the axis perpendicular to the incident direction and to the moment of the magnetic impurity) [1], even though the overall spin-dependent potential of the atom is central [34]. The asymmetry is due to terms of the scattering potential which involve the orbital angular momentum of the conduction electrons. The skew scattering is mainly considered as an intrinsic contribution to the anomalous Hall Effect due to the Berry phase of the Bloch wave function (for further details see Ref. [29]).

Side jump effect

Similar to skew scattering, the side jump effect causes an asymmetry in scattering between the left and right approach relative to the scattering center (whereas the skew scattering is associated with different scattering probabilities [49]). The center of mass of a wave packet experience a sideways displacement at the scattering. This is because

the scattering depends on or governed by an orbital momentum dependent potential [6]. According to the spin orientation of electrons, each spin orientation experiences different delay times and this time delay causes the spatial displacement. The side-jump mechanism therefore contribute to the Hall conductivity [30]. Illustration of skew scattering and side jump scattering mechanisms are shown in Figure 2.5.
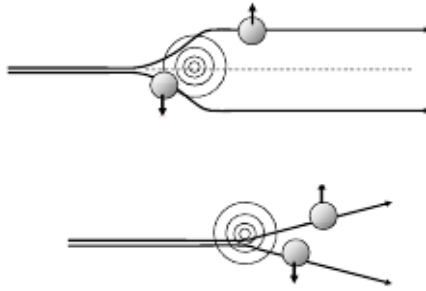
Figure 2.5: Illustration of skew scattering and side jump mechanisms. Upper case; Side jump: The electron velocity is deflected in opposite directions. The time-integrated velocity deflection is called as side jump. Lower case; Skew scattering: Asymmetric scattering due to the effective spin-orbit coupling of the electron and the impurity[30].

In 1930, Pugh [36] found that the Hall resistivity ρ_H is includes two terms,

$$\rho_H = R_0 \mathbf{B} + R_s 4\pi \mathbf{M}(T, \mathbf{B}), \tag{2.17}$$

where $R_0 \mathbf{B}_z$ describes the ordinary contribution (due to the Lorentz force) and $R_s 4\pi \mathbf{M_z}$ describes the anomalous contribution to the Hall effect (AHE). $\mathbf{M}(T, \mathbf{B})$ is the magnetization averaged over the sample. The ordinary Hall coefficient R_0 depends mainly on the density of carriers and tends to be temperature independent. On the other hand, the extraordinary Hall coefficient R_s was found to depend on a variety of material specific parameters and, especially, on the longitudinal resistivity ρ_{xx}. Moreover, R_s is usually very temperature dependent. This temperature dependence is originated from the skew scattering, since it is suggested that the skew scattering is a strongly temperature dependent phenomenon [31]. Moreover, in the absence of $\mathbf{B}$, a magnetic single domain in ferromagnetic body breaks down into many domains. The anomalous Hall coefficient

in Eq. 2.17 is proportional to the AHE in a single domain but even in the absence of applied field the AHE is still measurable. However the origin of this is still an ongoing debate [31].

2.3.3 Spin Hall effect in paramagnetic materials

In paramagnetic materials, moving electrons with spin and magnetic moment still experience the same scattering mechanisms that give rise to the anomalous Hall Effect(AHE) as in ferromagnetic systems. These scattering mechanisms can lead to spin transport in a perpendicular direction and spin accumulation at lateral boundaries. The effect is called spin Hall effect (SHE) and analogy to the AHE, the SHE does not require an applied magnetic field.
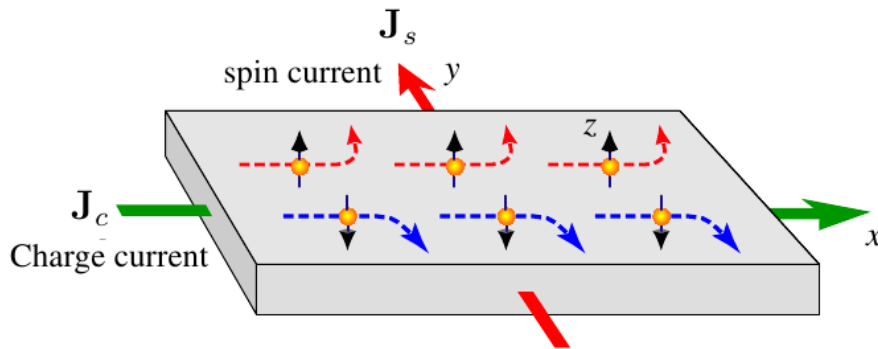
Figure 2.6: A schematic illustration of the transversal charge-current-induced spin in-balance at paramagnetic film; The spin Hall effect. $\mathbf{J}_c$ and $\mathbf{J}_s$ indicate the chare and the spin currents, and black arrows represents the spin polarization direction of electrons. [43]

In Fig. 2.6, the schematic illustration of the spin Hall effect is shown. The above mentioned scattering mechanisms give rise to the effect, and the process can be understood as regarding an unpolarized electron beam incidents on a spin-less scatterer, with an associated potential [19]

$$V = V_c(r) + V_s(r)\sigma \cdot \mathbf{L}, \tag{2.18}$$

where σ is the electron's spin and $\mathbf{L}$ orbital angular momentum. $V_s(r)$ represents the spin orbit scattering potential which is proportional to the gradient of scattering potential. As a consequence, the incident beam will be scattered by the polarization vector[19]

$$\mathbf{P}_f = \frac{fg^\star + f^\star g}{|f|^2 + |g|^2} \hat{\mathbf{n}}, \tag{2.19}$$

with $\hat{\mathbf{n}}$ is a unit vector perpendicular to the scattering plane in direction $\mathbf{k_i} \times \mathbf{k_f}$ where $\mathbf{k_i}, \mathbf{k_f}$ are incident and scattered wavevectors, respectively. f and g are the spin-independent and spin-dependent scattering parts of the scattering amplitude, respectively[19]. The sign of $\hat{\mathbf{n}}$ changes for the particles scattered in opposite directions, from the potential. Therefore, a spin dependent asymmetry is built up in the transverse direction towards the scattered beam.

There are several methods in use to detect spin Hall effect both in metallic or semiconductor systems. For instance, Kato and his coworkers reported on the optical detection of the spin Hall effect in thin films of the semiconductors i.e. GaAs and InGaAs. They showed the presence of electron spin accumulation at the edges of the samples by using Scanning Kerr rotation measurements (see Fig. 2.7)[21].

In the ordinary Hall Effect, the Hall voltage V_H is the charge imbalance which causes a difference in Fermi levels of both sides of the sample and can be measured by a voltmeter. Similarly in the spin Hall effect, the Fermi levels for each spin channels differ on both edges due to the spin imbalance. This is shown on the right side of the Figure 2.8.

In addition to the optical methods, one can also measure the spin imbalance by connecting both edges with a connector to measure the spin current. However this measurement is not a trivial technique.

A relatively trivial SHE experiment was proposed by J. E. Hirsch in Ref. [19]. The sample geometry can be seen in Figure 2.8. The charge current flows along the x direction with a current density j_x. The sample width L is smaller than the spin diffusion length. When the current is composed of only spin up electrons as shown in Figure 2.8 in the upper case, all the electrons are scattered in one direction thus the spin accumulation creates a local magnetization $M = n_\uparrow \mu_B$ only at one side of the sample. Here $n_\uparrow$ is the density of spin up electrons and μ_B is the Bohr magneton. By this experiment one can build not only spin imbalance between edges but also charge imbalance.

The anomalous Hall voltage along y-axes is given as: $V_H = 4\pi R_s L j_x n_\uparrow \mu_B$. This voltage is also equivalent to the spin Hall voltage of spin up electrons, since the voltage is generated only by spin up electrons. When the spin down electrons are also included
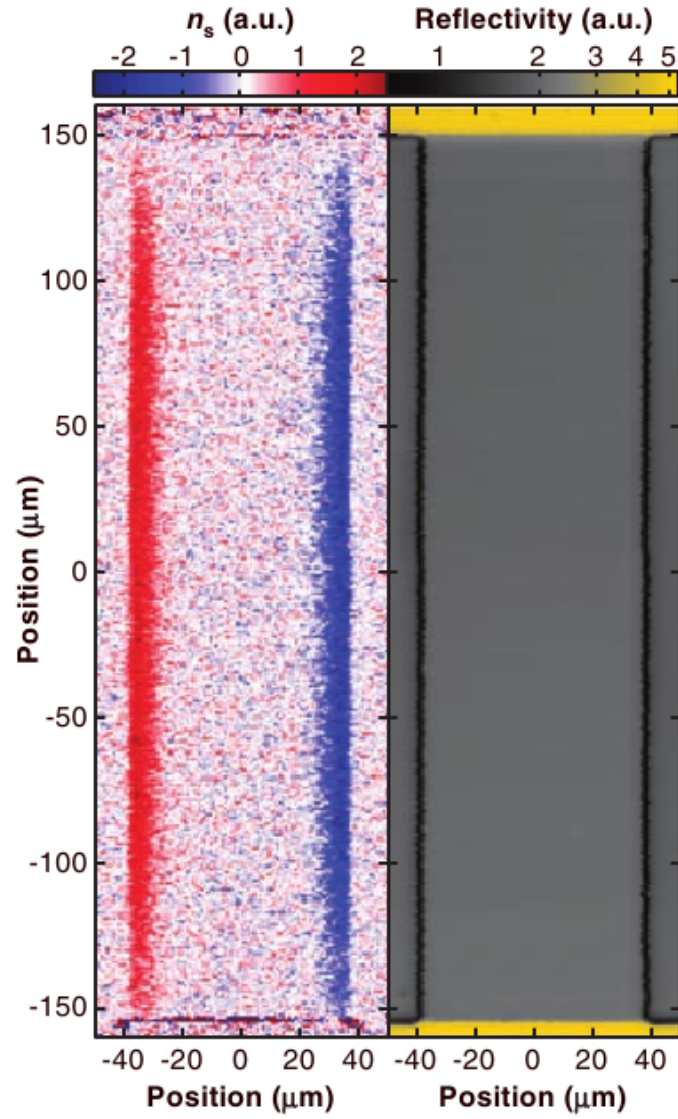
Figure 2.7: Two-dimensional images of spin density n_s and reflectivity R, respectively, for the unstrained GaAs sample measured at $T = 30\,K$. Blue and red color indicate opposite spin states. [21]
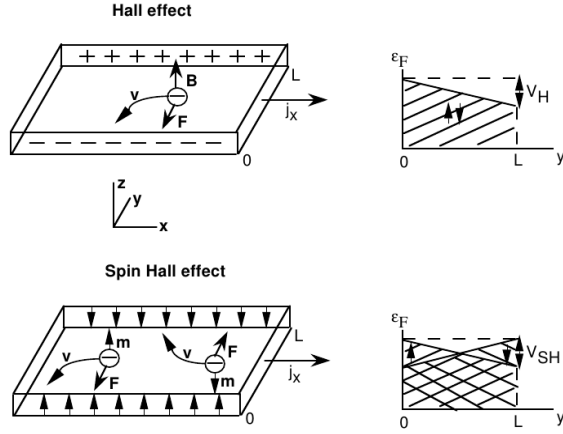
Figure 2.8: The spin Hall effect sample geometry.[19]

in the current, spin down electrons would scattered in the opposite direction and would give the same voltage but with opposite sign. The total spin Hall voltage then reads[19]

$$V_{SH} = 2\pi R_s L j_x n \mu_B. \tag{2.20}$$

Here n is the total conduction electron concentration. The case that both spin up and spin down electrons contribute to the spin Hall voltage can be seen in the lower part of Fig 2.8.

If the two edges of the sample are connected by a transverse metal strip as depicted in Figure 2.9, a spin current flows through the strip with a current density for each spin orientation $j_\sigma = V_{SH}/\rho L$. However, the same scattering mechanisms still affects each spin polarized current, and as a result, electron accumulation is built up only at one side of the strip because the spin polarized currents flow in opposite directions . The resulting spin Hall voltage transverse to the strip is given as [19],
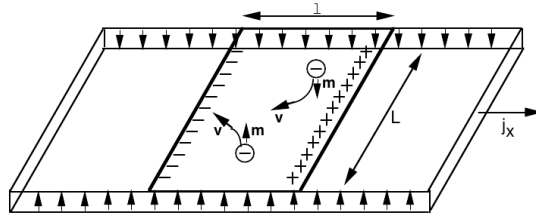
Figure 2.9: The spin Hall effect measurement by a transverse strip.[19]

$$V_{SC} = 8\pi^2 R_s^2 l \frac{(n\mu_B)^2}{\rho} j_x, \tag{2.21}$$

where l is the width of the strip. Although the sample width L is not included in equation (2.21), when L becomes comparable to the spin diffusion length, V_{SC} decreases [19] (sample width dependence of SHE is discussed in following section).

Recently, the giant spin Hall effect in ordinary gold was claimed to be observed by Seki et al. [40]. In their experiment, a substrate doped with iron impurities was used. They achieved to produce a large transverse Hall voltage one or two orders of magnitude greater than the comparable effect in other heavy metals. The so-called giant SHE was argued to be driven by electrons that scatter off iron impurities in the gold [16]. According to Guo et al.[16], the spin Hall conductivity of gold should scale with the iron concentration, and therefore, one might expect the iron atoms to produce a large anomalous Hall effect [12]. It is also argued in Ref [16] that the skew scattering mechanism for a giant spin Hall effect should be even stronger for rare-earth impurities, rather than transition metal impurities. This seems to be a promising area for future experiments.

2.4 Inverse spin Hall effect induced by spin pumping in ferromagnetic/paramagnetic bilayer system

In section 2.1 we have explained the magnetization dynamics in ferromagnetic systems, and later in section 2.2 we have shown the spin current generation from the precessing magnetization of the ferromagnetic layer in the vicinity of a nonmagnetic layer through the F-N interface. Afterwards, in section 2.3, the spin Hall effect was discussed which is the generation of a spin current from the charge current via the spin-orbit interaction in a paramagnetic system. The spin-orbit interaction which causes the spin Hall effect (SHE) is also responsible for the inverse process of the SHE in paramagnetic systems. The charge current production from a spin current is called the inverse spin Hall effect (ISHE). In this section we will use the model for the spin current in which the electrons with opposite spins travel in opposite directions along the spin-current spatial direction $\mathbf{J}_s$. According to this assumption there is no net charge current but only a spin current.
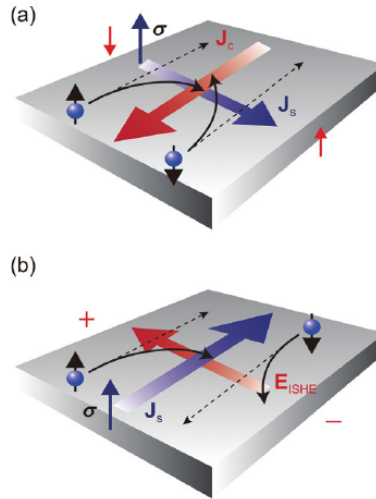
Figure 2.10: The spin Hall effect sample measurement by a transverse strip.[3]

The spin Hall effect and inverse spin Hall effect are shown in Figure 2.10 where σ is the spin polarization vector of the spin current. The trajectories of two electrons which are propagating in opposite directions bend in the same direction due to the spin orbit interaction. This gives rise to an electron accumulation on one side of the sample transverse to the spin current and polarization vector. The ISHE relation among $\mathbf{J}_s$, $\mathbf{J}_c$ and σ is given by [39][3],

$$\mathbf{J}_c = D_{ISHE}\mathbf{J}_s \times \sigma, \tag{2.22}$$

$$E_{ISHE} \propto \mathbf{J}_s \times \sigma, \tag{2.23}$$

where D_{ISHE} is the ISHE efficiency coefficient in a material and E_{ISHE} is the induced electric field by the transversal charge accumulation (ISHE). Coexistence of ISHE and SHE enables the reciprocal conversion between spin and charge currents, which is essential in combining spintronics with conventional electronics [39]. Here the direction of the spin polarization vector can be obtained from the magnitude and sign of the induced charge current $\mathbf{J}_c$.

The ISHE system in this work is a ferromagnetic-paramagnetic metallic bilayer system investigated with the spin-pumping method operated by ferromagnetic resonance. The ferromagnetic layer is polycrystalline Py $(Ni_{81}Fe_{19})$ which is a soft ferromagnet. As a nonmagnetic metallic layer, Pt is chosen due to the strong spin-orbit interaction. Heavy paramagnetic metals such as Pt and Pd allows the observation of ISHE at room temperature because of the high efficiency in converting the pumped spin current into charge current.
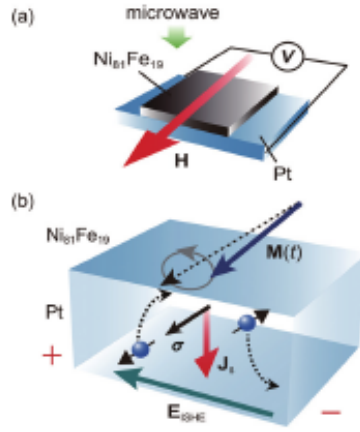
Figure 2.11: a) A schematic illustration of the system that is used in detection of the inverse spin Hall effect measurement. b)precessing magnetization pumps spin current into the Pt layer and due to the spin orbit interaction the trajectories of two electrons bend in the same direction due to the spin orbit interaction. This gives rise to an electron accumulation in one side of the sample transverse to the spin current and polarization vector. [3]

In Figure 2.11, a schematic illustration of the system used to detect the inverse spin Hall effect measurement is shown. Due to precessing magnetization at the FMR condition, the Py layer pumps spin current into Pt layer resonantly, and the induced transverse electric current causes a charge accumulation. This leads to a potential difference between the edges of Pt perpendicular to both applied magnetic field and microwave fields. The potential difference is measured by the electrodes attached to both sides of Pt.

2.4.1 Observation of ISHE Induced by spin pumping

By investigating the FMR spectra of Py, Py/Pt, and Pt/Py/Pt films one can easily see a clear enhancement in FMR linewidth by attaching the Pt capping layers as shown in figure 2.12. Since the spectral width is proportional to the Gilbert damping constant α, one can conclude that the enhancement in the damping constant is due to the magnetization precession relaxation or, in other words, the emission of a spin current from the magnetization precession created by spin pumping. As discussed in section 2.2 a spin current carries spin-angular momentum and therefore spin-current emission leads an additional magnetization-precession relaxation or enhanced α.

Layer 1	Layer 2	Layer 3	Linewidt
7nmPt	3nmPy	10nmPt	16.0mT
7nmPt	3nmPy	-	14.9mT
-	3nmPy	-	11.7mT
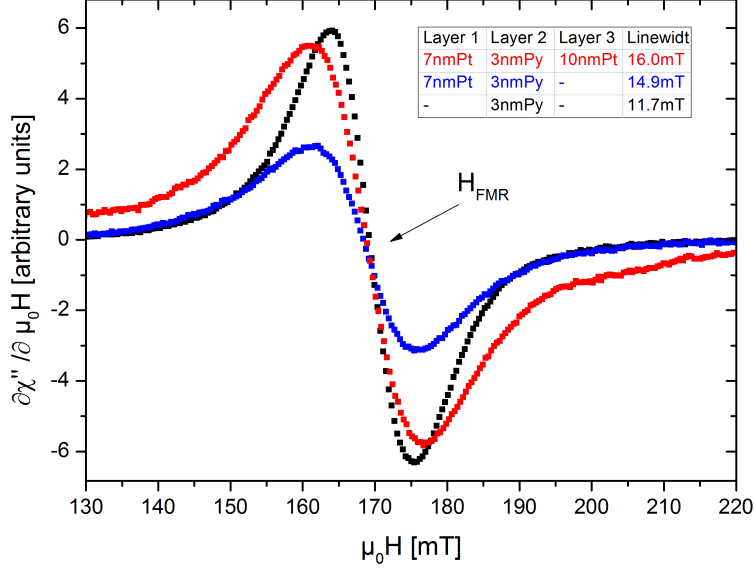
Figure 2.12: The magnetization precession relaxation was compared for Py films with and without capping layer as an applied external field (H parallel to the film plane) dependence of the FMR spectra $\partial\chi''/\partial\mu_0 H$ for the $Ni_{81}Fe_{19}/Pt$, $Pt/Ni_{81}Fe_{19}/Pt$ and the $Ni_{81}Fe_{19}$ film. the resonance positions for each sample ware very close, in order to compare the shift in the FMR line-widths I have moved the spectra to have their H_{FMR} met. Here, χ'' denotes imaginary part of the complex magnetic susceptibility and H_{FMR} is the ferromagnetic resonance field. The peak to peak value ΔH_{pp} corresponds to the FMR line-width. Gilbert damping constant α increases with capping layers. Since the spin-orbit interaction plays a key role in the enhancement due to the spin pumping, this results show a crucial role of the spin-orbit interaction in ISHE.

In the following, we will mention some variables that effects the V_{ISHE} signal.

2.4.2 The microwave power and angular dependence of ISHE

The dc component of a spin current generated by the spin pumping is proportional to the projection of $\mathbf{m}(t) \times d\mathbf{m}(t)/dt$ onto the the magnetization precession axis. Geometrically, this projection $\mathbf{m}'(t)$ is proportional to the square of the magnetization-precession amplitude. Therefore, the induced spin current or the electromotive force due to the ISHE is proportional to the square of the magnetization-precession amplitude, and thus linearly proportional the microwave power P_{MW} [3] since the magnetization-precession amplitude is proportional to $P_{MW}^{1/2}$. This gives the relation among V_{ISHE}, $\mathbf{J}_c$, $\mathbf{J}_s$ and

29

P_{MW}

$$\mathbf{J}_s \propto \mathbf{J}_c \propto V_{ISHE} \propto P_{MW}. \tag{2.24}$$

The electromotive force V_{ISHE} has a strong angular dependence. This is consistent with the prediction of ISHE and spin pumping; spin pumping generates a spin current with the spin-polarization-vector σ parallel to the magnetization-precession-axis into the paramagnetic layer.
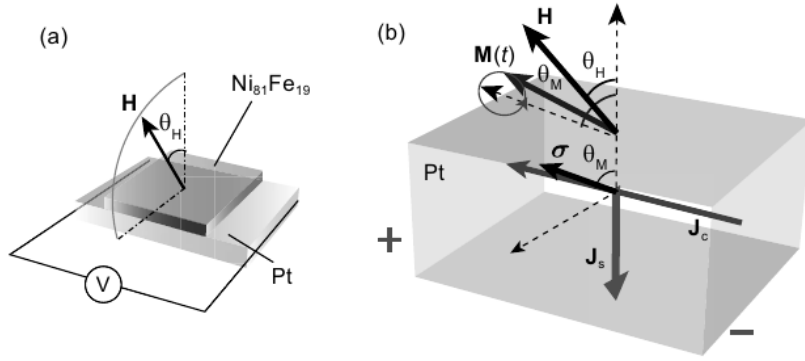
Figure 2.13: a) θ_H is the angle that external field and magnetization precession makes to the normal vector of the film plane. b) a schematic illustration of V_{ISHE} [2]

The angles θ_H and θ_M are the angles between the external field and magnetization precession with respect to the normal vector of the film plane. The electromotive force reaches a maximum when θ_H is 90° because in this case, the maximum spin current is emitted perpendicular to the interface. When $\theta_H = 0°$, the effect is zero due to the loss of spin current, and the applied magnetic field reverses its direction towards $-90°$. $\mathbf{J}_c$ and V_{ISHE} changes its direction and sign, respectively and finally has a maximum amplitude once again at $\theta_H = -90°$.

In order to define the relation between V_{ISHE} and θ_M, one needs to consider the θ_H dependence of the electromotive force and the FMR resonance field H_{FMR}. θ_M is calculated from the angular dependency of H_{FMR} using the LLG equation. In equilibrium, namely $\mathbf{M}_{eff} \times \mathbf{H}_{eff} = 0$, the relationship between θ_M and θ_H is given by [2]

$$\left(\frac{H}{4\pi M_s}\right) \sin(\theta_M - \theta_H) = \sin\theta_M \cos\theta_H, \tag{2.25}$$

where H is the external magnetic field and M_s refers to the saturation magnetization.

$\omega = 2\pi f$ is the angular frequency of the microwave. The resonance condition can be obtained by neglecting the ac field (namely, the microwave field and the modulation field if any), and the damping term. The resonance condition is given by [2]

$$\left(\frac{\omega}{\gamma}\right)^2 = [H_{FMR}\cos(\theta_M - \theta_H) - 4\pi M_s \cos 2\theta_M] \times [H_{FMR}\cos(\theta_M - \theta_H) - 4\pi M_s \cos^2 \theta_M].$$
(2.26)

Here, for soft ferromagnetic materials such as Py, the magnetization is aligned with the external field when $\theta_H = 0°$ and $\theta_H = 90°$. The only anisotropy contribution is assumed to be the shape anisotropy. Therefore one can obtain the resonance conditions at these angles as [2]

$$\left(\frac{\omega}{\gamma}\right)^2 = (H_{FMR} - 4\pi M_s)^2,$$
(2.27)

at $\theta_H = 0°$ and

$$\left(\frac{\omega}{\gamma}\right)^2 = (H_{FMR} + 4\pi M_s)^2 H_{FMR},$$
(2.28)

at $\theta_H = 90°$. By using the out-of-plane angular dependence measurement H_{FMR} values one can determine the the effective magnetization M_{eff} and as well the constant ω/γ. Substituting the measured H_{FMR} values and M_{eff} in equation (2.26), we obtained the dependency function $\theta_M(\theta_H)$ as shown in Fig. 2.14.
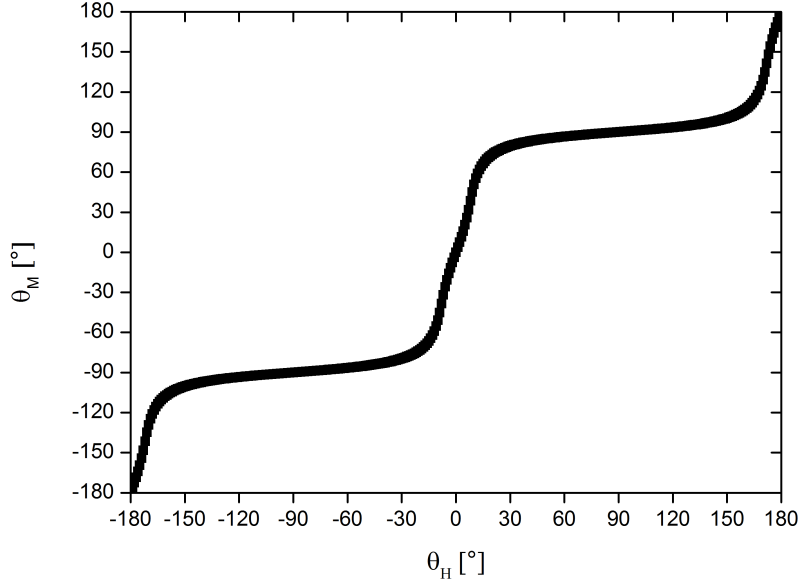
Figure 2.14: θ_H dependence of θ_M. Note that at $0°, 90°, -90°$ the magnetization and the applied field vectors are parallel.

The spin polarization of the spin current produced by the spin pumping is proportional to $\mathbf{m}(t) \times d\mathbf{m}(t)/dt$. Therefore, in the system as depicted in Figure 2.15 the dc electromotive force V_{ISHE} induced by spin pumping is proportional to the projection of $\mathbf{m}(t) \times d\mathbf{m}(t)/dt$ on z-axis.
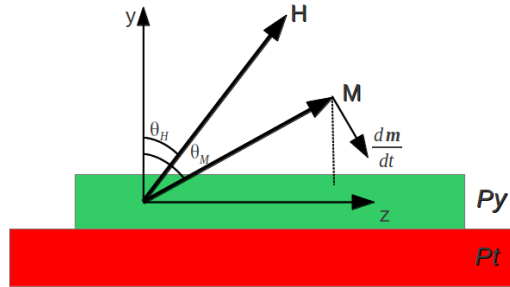
Figure 2.15: Pt/Py bilayer system with magnetization vector orientations

The instantaneous magnetization is described as the vector sum of static and dynamic components as $\mathbf{M}(t) = \mathbf{M} + \mathbf{m}(t)$. By taking into account the external magnetic field, the static demagnetizing field, the dynamic demagnetization field, and the external ac field (superposition of all is the effective magnetic field, H_{eff}), one can write the equation for the x and y components of $\mathbf{m}(t)$ by ignoring the second-order contribution of the precession amplitude as [2]

32

$$m_x(t) = \frac{h_{ac}(i\tilde{\omega}(\alpha/\gamma)) + [\tilde{H}\cos(\theta_M - \theta_H) - \cos 2\theta_M])}{4\pi\cos(\theta_M - \theta_H)[2\tilde{H}\cos(\theta_M - \theta_H) - (\cos 2\theta_M + \cos\theta_M^2)]} \frac{e^{i\omega t}}{\tilde{H} - \tilde{H}_{FMR} + i\frac{\alpha\tilde{\omega}}{\cos(\theta_M - \theta_H)}}$$

$$m_y(t) = \frac{i\omega h_{ac}}{4\pi\cos(\theta_M - \theta_H)[2\tilde{H}\cos(\theta_M - \theta_H) - (\cos 2\theta_M + \cos\theta_M^2)]} \frac{e^{i\omega t}}{\tilde{H} - \tilde{H}_{FMR} + i\frac{\alpha\tilde{\omega}}{\cos(\theta_M - \theta_H)}},$$

(2.29)

where $\tilde{\omega} = \frac{\omega/\gamma}{4\pi M_s}$ and $\tilde{H} = \frac{H}{4\pi M_s}$. Since $V_{ISHE} \propto \langle Re(\mathbf{m}(t)\times d\mathbf{m}(t)/dt)\rangle_z = -\omega\cos\theta_M Im(m_x m_y)$ [2], and the spin current as a function of θ_M is given as [3],

$$j_s = \frac{g_r^{\uparrow\downarrow}\gamma^2 h^2\hbar\left[4\pi M_s\gamma\sin^2\theta_M + \sqrt{(4\pi M_s)^2\gamma^2\sin^4\theta_M + 4\omega^2}\right]}{8\pi\alpha^2\left[(4\pi M_s)^2\gamma^2\sin^4\theta_M + 4\omega^2\right]},$$

(2.30)

where h_{ac} is the microwave field, $g_r^{\uparrow\downarrow}$ is the mixing conductance. The θ_M dependence of j_s is shown in Figure 2.16.
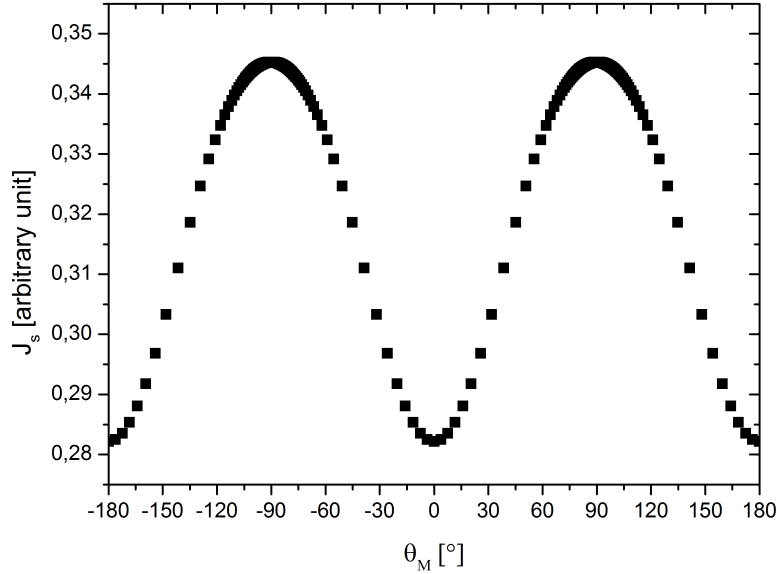
Figure 2.16: The θ_M dependence of j_s

The electromotive force induced by spin pumping is then clearly proportional to the projection of θ_M on the film plane which gives the spin polarization direction, namely $V_{ISHE} \propto J_s\sin\theta_M$ due to the relation $\mathbf{E}_{ISHE} \propto \mathbf{J}_s \times \sigma$. As a result, the θ_M dependence of the electromotive force can be written as [3]

$$V_{ISHE} \propto \frac{g_r^{\uparrow\downarrow}\gamma^2 h^2 \hbar \sin\theta_M \left[4\pi M_s \gamma \sin^2\theta_M + \sqrt{(4\pi M_s)^2 \gamma^2 \sin^4\theta_M + 4\omega^2}\right]}{8\pi\alpha^2 \left[(4\pi M_s)^2 \gamma^2 \sin^4\theta_M + 4\omega^2\right]}, \qquad (2.31)$$

where h_{ac} is the magnitude of the microwave field.
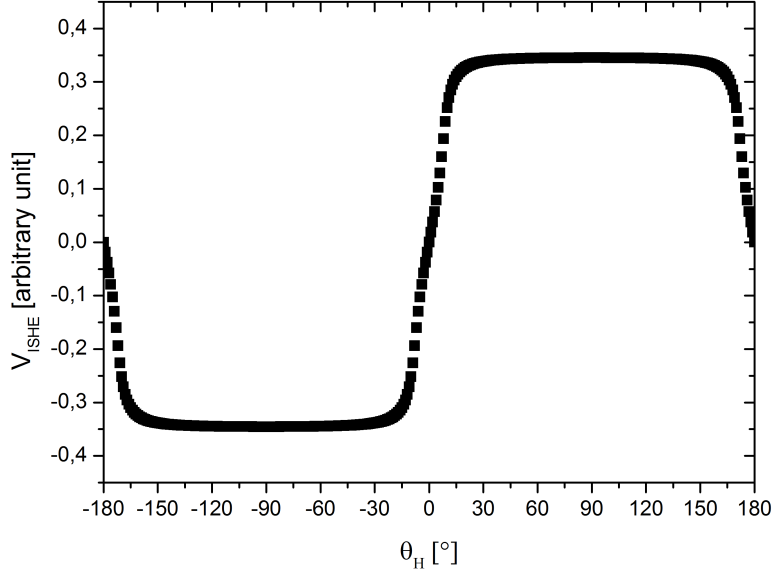
Figure 2.17: The θ_H dependence of electromotive force V_{ISHE} according to equation (2.31). Here V_{ISHE} changes sign when the external field changes its direction across zero. This is obviously due to the change in orientation of spin polarization vector σ which is parallel to the magnetization- precession axis. Therefore $\mathbf{J}_c$ and $\mathbf{J}_s$ is reversed if the magnetic field is inverted.

2.4.3 The temperature and frequency dependence of ISHE

In figure 2.18, the amplitude of the V_{ISHE} signal is plotted for Py/Pt and Py/Au bilayer metallic systems as a function of temperature.
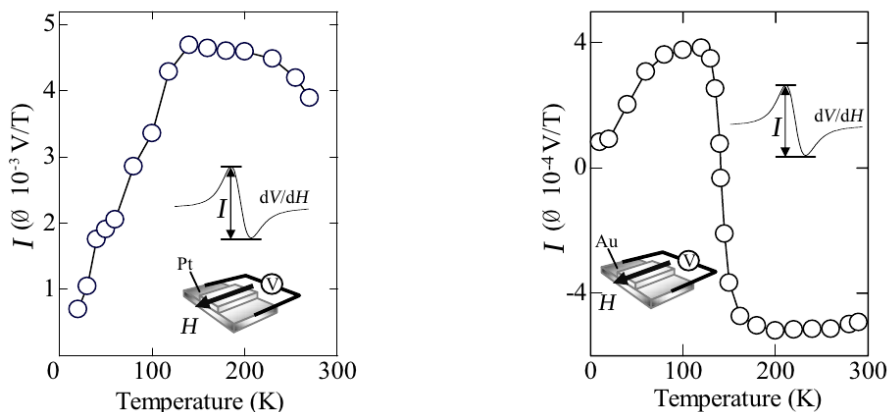
Figure 2.18: The variation of V_{ISHE} signal for a Py/Pt and Py/Au bilayer metallic systems as a function of temperature [49].

At low temperatures, the V_{ISHE} amplitude decreases. At these temperatures, the inelastic scattering of conduction electron, including the electron scattering due to phonons, is incapable for generating the Hall voltage; because, phonons and other fluctuations are suppressed [49]. This explains the low temperature behavior of both Pt and Au. However, around $140\,\text{K}$, the electromotive force signal changes its sign for Au sample. This behavior suggests a coexistence of two different contribution with different signs in this extrinsic mechanism of the inverse spin-Hall effect; the skew-scattering mechanism and the side-jump mechanism are the candidates for the two different contribution, and over the temperature range the dominant effect is different [32]. As a conclusion, the inverse spin Hall effect has a temperature dependence but this dependence is also material dependent.

V_{ISHE} amplitude varies by the ferromagnetic resonance frequency f_{FMR} as proven experimentally in this thesis. The systematic relationship of resonance frequency between f_{FMR} and resonance field is well explained by Kittels formula,

$$(\omega/2\pi) = (\mu_0\gamma_{eff})\sqrt{H_{FMR}(H_{FMR} + M_{eff})}, \tag{2.32}$$

where γ_{eff} is the effective gyromagnetic ratio. With an ansatz that the microwave-absorption power P_{ab} by the ferromagnetic layer at f_{FMR} is proportional to the incident microwave power P_{in}, one can express the rf-field amplitude h as [17]

$$h^2 = \frac{P_{ab}}{\nu\pi f_{FMR}\mu_0\chi''_{FMR}}, \tag{2.33}$$

where ν is the volume in which the irradiated microwave is absorbed and χ''_{FMR} is the

imaginary part of the complex magnetic susceptibility under FMR conditions which is given as [17]

$$\chi''_{FMR} = \frac{\sqrt{1 + 4\tilde{\omega}^2} + 1}{2\alpha\tilde{\omega}\sqrt{1 + 4\tilde{\omega}^2}}. \tag{2.34}$$

Here $\tilde{\omega} \equiv 2\pi f_{FMR}/(\gamma_{eff}\mu_0 M_s)$. Experiments show that V_{ISHE} decrease slightly with increasing $\tilde{\omega}$. This result expresses that spin current induced by the spin pumping decreases with increasing f_{FMR}. However spin current is expected to increase with increasing f_{FMR} [17]. The decrease in the spin current and thus V_{ISHE} is due to the fact that the magnetization-precession frequency and the spin current generated by a cycle of the precession j_s^1 compensates each other, and both depend on the frequency, but with a relation $j_s = f_{FMR} \cdot j_s^1$, where [17]

$$j_s^1 \equiv \frac{\hbar}{2} g_r^{\uparrow\downarrow} \frac{1}{M_s^2} \int_0^{(1/f_{FMR})} \frac{1}{2\pi} \langle \mathbf{M}(t) \times \frac{d\mathbf{M}(t)}{dt} \rangle_z dt. \tag{2.35}$$

Here $\langle \mathbf{M}(t) \times \frac{d\mathbf{M}(t)}{dt} \rangle_z$ is the z-component of $\mathbf{M}(t) \times d\mathbf{M}(t)/dt$ where z is the direction of the magnetization-precession axis. By substituting equation (2.35) in the Landau-Lifshitz-Gilbert equation, j_s reads [17],

$$j_s = \frac{h^2 g_r^{\uparrow\downarrow} \gamma_{eff}\mu_0}{4\pi\alpha^2 M_s} \frac{(\sqrt{1 + 4\tilde{\omega}^2} + 1)}{2(\sqrt{1 + 4\tilde{\omega}^2})}. \tag{2.36}$$

The decrease in V_{ISHE} is explained with decrease in j_s^1, because j_s^1 is proportional to the area of the magnetization-precession trajectory S which decreases with increasing f_{FMR}. This is due to the decrease in the magnetization precession angle with the increase in ferromagnetic resonance field H_{FMR}. This fact leads to the conclusion that the spin-current density decreases slightly with increasing precession frequency, which is consistent with the spin pumping model [17].

2.4.4 Influence of sample shape on ISHE

The electromotive force generated in a paramagnetic layer from an injected spin current occurs only in the skin depth of the spin flip length [27]. For a Pt/Py system studied in this thesis, the Py layer acts as a short and reduces the voltage difference between the electrodes attached to the paramagnetic Pt ends. The induced electric field component along the measurement direction (y-axis) is given as [27],

$$E_y = \frac{P g_{eff}^{\uparrow\downarrow} \sin\alpha \sin^2\theta \gamma e \omega_f \lambda_{sd}}{2\pi(\sigma_N t_N + \sigma_{Py} t_{Py})} tanh\left(\frac{t_N}{2\lambda_{sd}}\right), \tag{2.37}$$

where P is the elipcticity correction factor, e is the electron charge, α is the angle between external field H and the waveguide axis (along y), γ is the spin Hall angle, and σ_N and σ_{Py} are the charge conductivities in the N layer (e.g., Pt) and Py. t_N and t_{Py} correspond to the thicknesses of the N and Py layers. The resulting voltage is calculated as [27]

$$V_{ISHE} = \frac{LPg_{eff}^{\uparrow\downarrow}\sin\alpha\sin^2\theta\gamma e\omega_f\lambda_{sd}}{2\pi(\sigma_N t_N + \sigma_{Py}t_{Py})}tanh\left(\frac{t_N}{2\lambda_{sd}}\right),$$ (2.38)

where L is the length of the ferromagnetic layer. It must be noted that the generated voltage depends on the sample length. Therefore, the generated voltage can be increased by increasing the sample length. Moreover, the other important point is the thickness of the paramagnetic layer. Since t_N is comparable to the spin flip length λ_{sd}, the measured voltage depends only very weakly on either value, since $(t_N/2\lambda_{sd})tanh(t_N/2\lambda_{sd})$ is nearly constant [27]. Paramagnetic layer thickness on the other hand is important when the layer is not a perfect spin sink, since bad spin sink materials reflect the spin current from the N/Vacuum interface back into the ferromagnetic layer, and thus the effective spin pumping is reduced. Moreover, in Ref. [32] by an equivalent circuit model, it has been shown that V_{ISHE} is inversely proportional to the Pt thickness. In this case the Pt thickness is beyond the spin diffusion length. In this regime, the V_{ISHE} and Pt thickness d_N are related with a formula [32],

$$\frac{1}{V_{ISHE}} = \frac{\omega_N}{I_C\rho_N l_N}d_N,$$ (2.39)

where ω_N, ρ_N, l_N are the width, the resistivity and the length of the Pt layer, respectively, and I_C, is the charge current in the equivalent circuit.

The shape of the films influence also the magnetization-precession trajectory. As it is experimentally shown in Ref [27] for Pt/Pt bilayer system, the ferromagnetic resonance occurs around $200\,\text{Oe}$ at $4\,\text{GHz}$. At this field, the precession of magnetization is strongly disturbed and is highly elliptical. They also show that the correction factor P increases by factor 3 in the range $3\,\text{GHz}$ to $12\,\text{GHz}$. These results show that the most effective spin pumping and V_{ISHE} is produced not with circular precession but with elliptical trajectory of magnetization precession [27].

3 Experimental Procedure

Figure 3.1 shows a schematic illustration of a sample and the circuitry used in this thesis which is a $Ni_{81}Fe_{19}/Pt$ bilayer film system with $10\,\mathrm{nm}$ Pt and $10\,\mathrm{nm}$ Py deposited on a thermally oxidized silicon substrate. Both layers have a rectangular surface area, $0,4\,mm \times 1,2\,mm = 0,48\,mm^2$ for ferromagnetic Py and $0,4\,mm \times 2,2\,mm = 0,88\,mm^2$ for paramagnetic Pt layers. These layers were patterned either using metal masks or electron beam lithography (EBL). The Pt layer was evaporated by electron beam evaporation on a thermally oxidized Si substrate. Subsequently the $Ni_{81}Fe_{19}$ layer was evaporated on the Pt layer in the same ultra high vacuum chamber $(4 \times 10^{-8}\,mbar)$ using a different mask. Next, the substrate is placed on a sample stage. Two different sample holders were produced for different measurement purposes. The first one is for the measurements which were performed in a cavity, and the second sample holder was produced for the multifrequency measurement. The same sample stage is used for both sample holders. For the measurements that we performed with a cavity, we used only one sample in order to avoid any extra material or production artifacts.
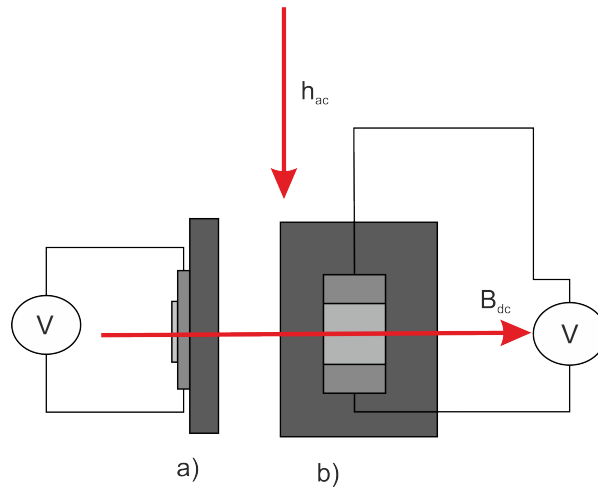
Figure 3.1: ac microwave field and dc static magnetic fields are shown with red arrows a)a side view and b)an overview of Py/Pt/Si heterostructure

In this section, the thin film fabrication, the sample stage, the sample holders, the

ferromagnetic resonance measurement method, and V_{ISHE} measurement setups will be discussed in detail.

3.1 Sample preparation

The $Ni_{81}Fe_{19}/Pt$ bilayer film system with 10 nm Pt and 10 nm Py was deposited on a thermally oxidized silicon substrate. For thin film deposition it is very essential to have a clean substrate. Si substrates a were supplied from a cut Si wafer. Each substrate has a 3.8×4 mm size. In order to clean the surface, the substrate was placed in acetone and placed on ultrasonic cleaner for 10 minutes. After ultrasonic treatment, each substrate was checked by a light microscope in the dark field mode for a contamination free surface. Usually 10 minutes ultrasonic cleaning is enough to remove contaminants such as dust, dirt, oil, grease, polishing compounds, etc. When the substrate surface was clean, the Py/Pt bilayer was evaporated.

3.1.1 Film deposition by the electron beam evaporation

In order to fabricate Pt and Py thin films structures on a clean substrate, the electron beam evaporation method was used. The evaporation setup works under high vacuum for several reasons such as longer mean free path of evaporant particles and contaminat free surfaces. In our set up, different metals and alloys such as Ni, Co, Fe, Py,Cu, Ti, Au or Pt can be evaporated. The evaporants have $> 99.99\%$ purities.

In electron beam evaporation, the substrate is located inside a vacuum chamber in which the evaporant material is also placed. The evaporant is heated until it boils and consequently evaporates. The evaporated particles spread out in every direction and condense on the chamber walls and substrate surface. This is the principle in all evaporation methods. The difference between each method comes from the heating mechanism of source material. In electron beam evaporation method the heating of the source material is provided by an electron beam emitted from a heated thermionic filament. The beam is then accelerated and focused by magnetic fields and hits the surface of the evaporant source material causing a local heat increase and evaporation. With this method, a wide variety of materials can be evaporated. Since in this method a large amount of heat is concentrated on a very small area, high rates of deposition can

be achieved. A schematic diagram of a typical system for e-beam evaporation is shown in the figure 3.2.
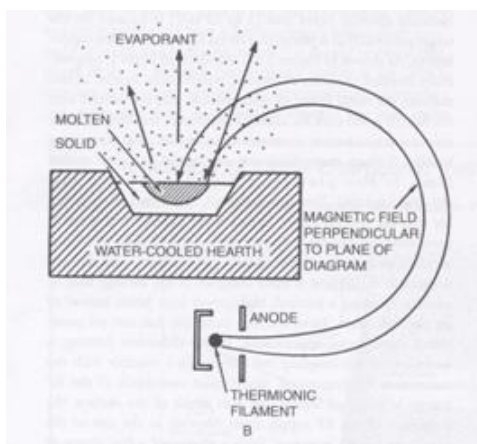
Figure 3.2: Diagram of an electron-beam evaporation system. (From M. J. Madou, "Fundamentals of Microfabrication)

The evaporation setup that is used for the thin film evaporation can be seen in Figure 3.3.

Figure 3.3: The electron beam evaporation setup that is used for thin film evaporation. The main chamber is on the right which is covered with aluminum film. On the left the transfer rod can be seen. (Uni Duisburg Essen / AG Farle)
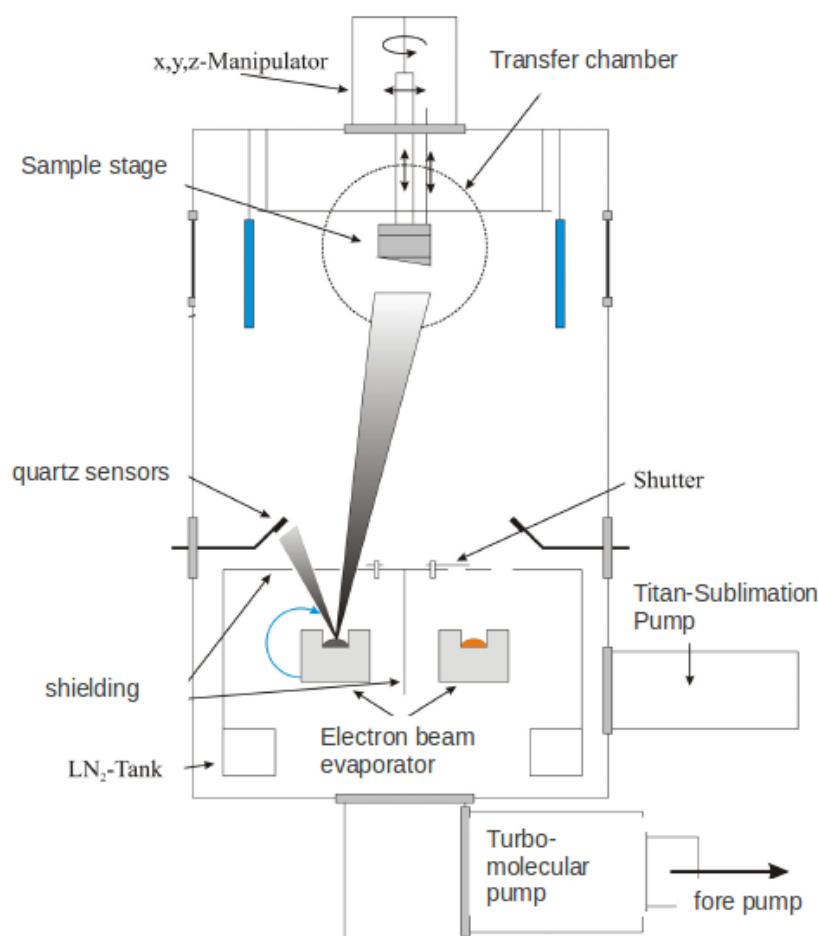
Figure 3.4: Schematic illustration of the electron beam evaporation setup [35]

When the clean sample is placed on a sample stage, it can be attached to the transfer rod. This is done in the transfer chamber. After closing the transfer window, the air in the chamber is removed until the vacuum reaches 10^{-6} $mbar$. Then the valve between the transfer chamber and the main chamber is opened, and the sample stage is attached to the evaporation position which can be manipulated in 3 dimensions. The source materials are positioned at two opposite sides of the chamber floor as shown in figure 3.4, and the stage has to be directed to an appropriate orientation by manipulating in the x-y plane. Once everything is ready the electron beam can be switched on. The evaporant is closed with a shutter which is used to control the growth of thin film and to shield it from the initial burst of "cord" that comes off the evaporant when it first melts. One has to wait before opening shutter until the stable desired rate of deposition is reached. The suitable rate of 0.15 Å per second is the same for Pt and Py and it is. By controlling the melted source visually through the chamber window, the deposition

can be carried out. Usually, a 10 nm deposition takes about 20 minutes. When the film reaches the desired thickness, the shutter is closed, and the electron beam is switched off. At that moment, the substrate is kept under high vacuum for about 20 more minutes for slow cooling. Then the sample can be transfered back to the transfer chamber and finally outside of the setup.

In order to pattern structures, one has to use specific masks. In structure production, we used two different methods. The first method is evaporating with a metal mask made of steel processed by a laser. The second method is electron beam lithography.

Film fabrication with a metal Mask

We fabricated several masks for Pt and Py layers. After laser cutting the masks, they were polished and cleaned in acetone-ethanol solution in an ultrasonic bath. The cleaned mask was then attached onto the sample stage for electron beam evaporation on which the substrates were placed beforehand. The mask was fixed to the stage with two screws. For each evaporation layer, there is a different mask with different dimensions, thus for every step specific a mask was used.

Film fabrication with Electron Beam Lithography

The second method for structure patterning on a substrate is electron beam lithography. The electron beam lithography (EBL) refers to a lithographic process that uses a focused beam of electrons to form the patterns needed for material deposition or removal from the substrates. Electron lithography provides high patterning resolution because of the short wavelength possessed by the 10-50 keV electrons that it employs. EBL system does not need additional masks to perform its task. Instead a small diameter focused beam of electrons scan over a substrate surface. EBL uses positive and negative resists, which is referred to as electron beam resists (or e-beam resists). Electron beam resists are the recording and transfer media for e-beam lithography. The usual resists are polymers dissolved in a liquid solvent. Liquid resist is dropped onto the substrate, which is then spin-coated at 1000 to 6000 rpm. An EBL system simply writes or draws the pattern over the resist wafer using the electron beam as its drawing pen. For each desired sample thickness, one needs to use a specific resist or resist combinations.
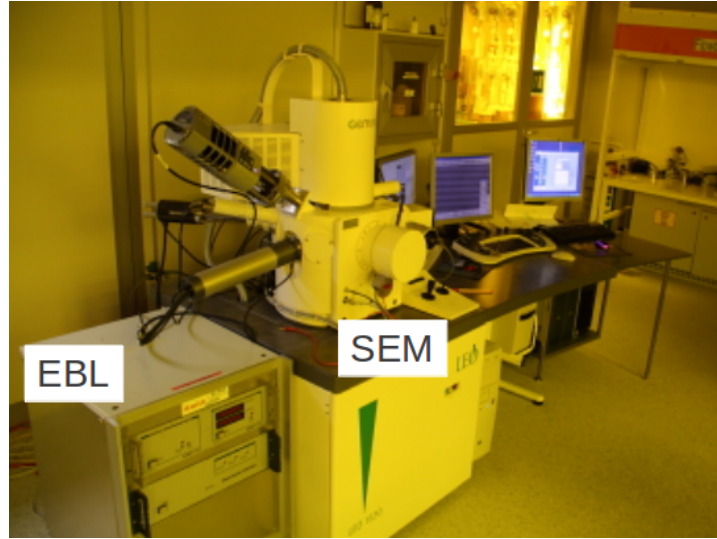
Figure 3.5: LEO 1530 Scanning electron microscope with Raith ELPHY Plus EBL unit.(clean room, Ag Farle, University of Duisburg Essen)

Patterning a thin film structure with EBL is performed in a clean room environment in order to avoid surface contaminations. A thermally oxidized silicon substrate with specific resistance $\rho > 1\,\Omega$ was used. The substrate was cleaned for 10 minutes in acetone in an ultrasonic bath. The electron resist (Polymethyl methacrylate (PMMA)), which is a long-chained polymer in a liquid solvent (type 600K 4 %) was dropped on a substrate and spun for 30 seconds at 6000 rpm. In EBL, it is very essential to have a homogeneous resist thickness over the substrate. Then the substrate was baked at 150 °C for 10 minutes to evaporate the solvent. Later on, another PMMA type 950K 1 % was dropped and spun and baked at 150 °C for 5 minutes. This resist combination is well known for structures with less than 20 nm thickness. After this using a scanning electron microscope (Zeiss, model LEO 1530) with an integrated EBL unit (RAITH, Elphy Plus), the structure was patterned on the resist by a 20 kV e-beam exposure. The electron beam-substrate-PMMA interaction is shown in figure 3.6. Basically, the electron beam exposure breaks the polymer into fragments that are dissolved preferentially by a developer. As a result, the structure layout which is defined beforehand is transferred to the substrate.
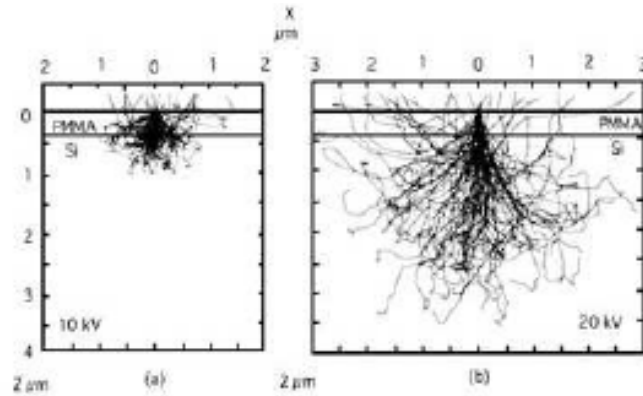
Figure 3.6: Monte Carlo simulation of electron scattering in resist on a silicon substrate at a) 10 KeV and b) 20 KeV. (From Kyser and Viswanathan)(Electron beam lithography,Hans-Georg Braun, September 22, 2008)

In order to remove exposed resist from the substrate, a developer and a stopper solution were utilized. The developer (Allresist, type AR600-56) is a solution of 25 % Methylisobutylketon (MIBK) and 75 % Isopropanol (IPA). The developing lasts 2 minutes and the process is stopped by a stopper solution in 30 seconds. The stopper solution is from the same company, type Typs AR600-60. After developing, the sample was transfered into the electron beam evaporation chamber. After the evaporation process, the sample was placed into boiling acetone at $83\,^{\circ}$C for the liftoff process. In the liftoff process, all remaining resist was washed away. Typical EBL steps are shown in Fig. 3.7.
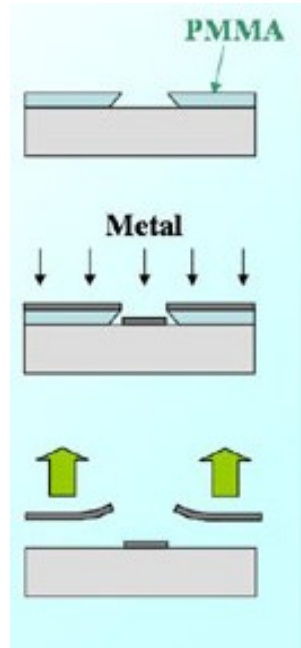
Figure 3.7: With a suitable developer, exposed PMMA can be dissolved, and new metal layer can be evaporated. The resulting pattern in the resist can be transferred to the sample using metal lift-off with lift-of the remaining resist is dissolved in aceton and as a result unwanted metal is lifted off. [33]

In this section, two techniques have been explained that were utilized for thin film patterning. Although using a mask is a faster method than using EBL, the structure shape that is produced by mask is more rough. EBL provides sharp and straight sample edges. The mask is produced by laser cutting with a laser beam of 0.4 mm diameter, and the width of the sample is also 0.4 mm. Therefore, the mask and thus the structure have curved corners. A scanning electron microscopy image is shown for the sample which is patterned by a metal mask in Fig. 3.8 and patterned by an EBL in Fig. 3.9.
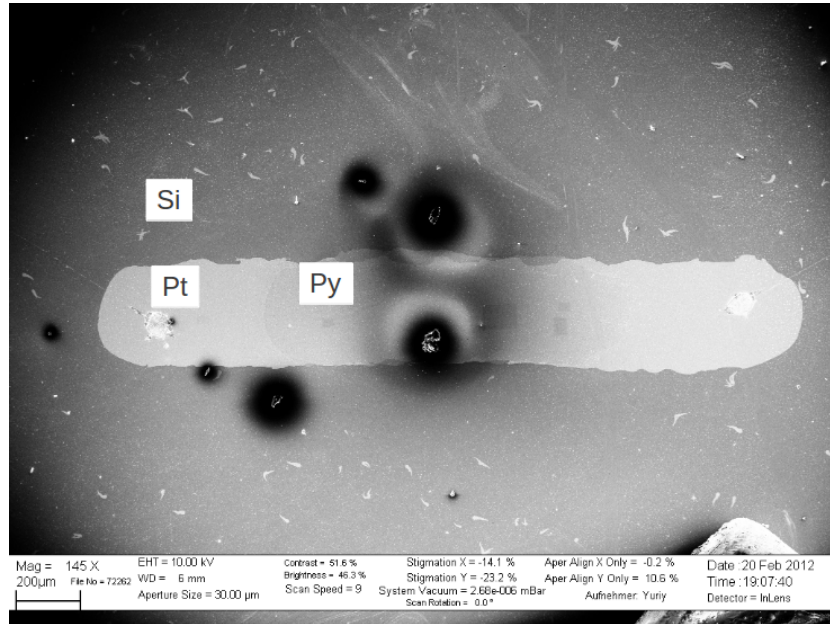
Figure 3.8: Py/Pt bilayer on Si substrate patterned by a metal mask
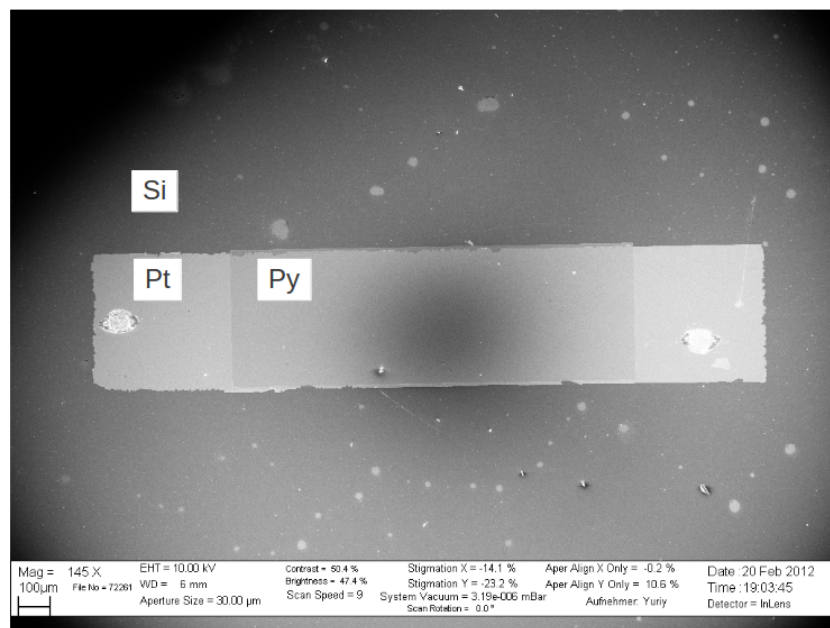
Figure 3.9: Py/Pt bilayer on Si substrate patterned by electron beam lithography

For this thesis, we have installed an additional shutter into the evaporation chamber which allowed us to evaporate the Py layer of the samples with and without Pt capping layer simultaneously. By this, we were sure that the Py layer are identical with thickness and material composition. We have used this samples to investigate the enhancement

46

of FMR linewidth which is directly related to spin pumping efficiency of Py layer.

Material and structure characterization

For the material characterization of the bilayer system, Energy-dispersive X-ray spectroscopy (EDX) was used. The EDX detector (Oxford Instruments, X-Max Silicon Drift Detector) is connected to the scanning electron microscope which also includes EBL unit. In order to detect and material inhomogeneity, several measurement on different positions have been taken. Concentrations in at % are given in table 3.1 for each spectrum.
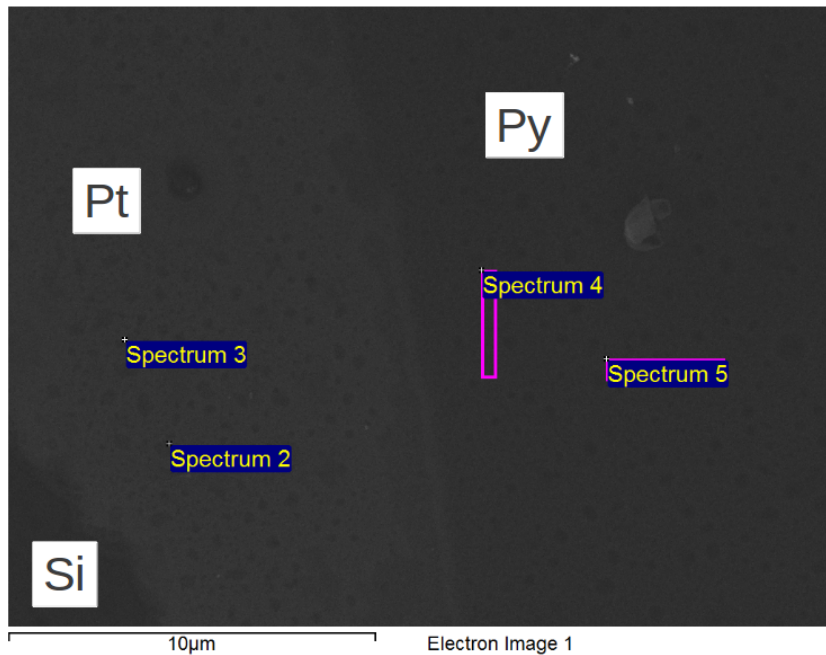
Figure 3.10: Different layers are recognizable by the color contrast. Four EDX measurements in different positions has been taken. Spectrum 2 and 3 were point-scanned, and spectrum 4 and 5 were area-scanned.

Spectrum	Fe	Ni	Pt
Spectrum 2	0	0	100.00
Spectrum 3	0	0	100.00
Spectrum 4	24.77	75.23	-
Spectrum 5	26.87	73.13	-

Table 3.1: EDX results , performed with $20\,\mathrm{kV}$ beam voltage.

As seen in table 3.1, the permalloy that was evaporated is not homogeneous. This is also proven by FMR measurements. The FMR signal was not symmetric, and the

out-of-plane signal consist of two separate signals.

The layer thickness of the Py/Pt bilayer was measured by an atomic force microscope (AFM) (Park systems, XE-70) in a noncotact mode. The Pt layer is 8 nm thick whereas the Py layer is 14 nm thick with an 1 nm error. They supposed to have 10 nm thickness. This unexpected results is probability due to a faulty calibration in electron beam evaporation. The results are shown in figure 3.11 and 3.12.
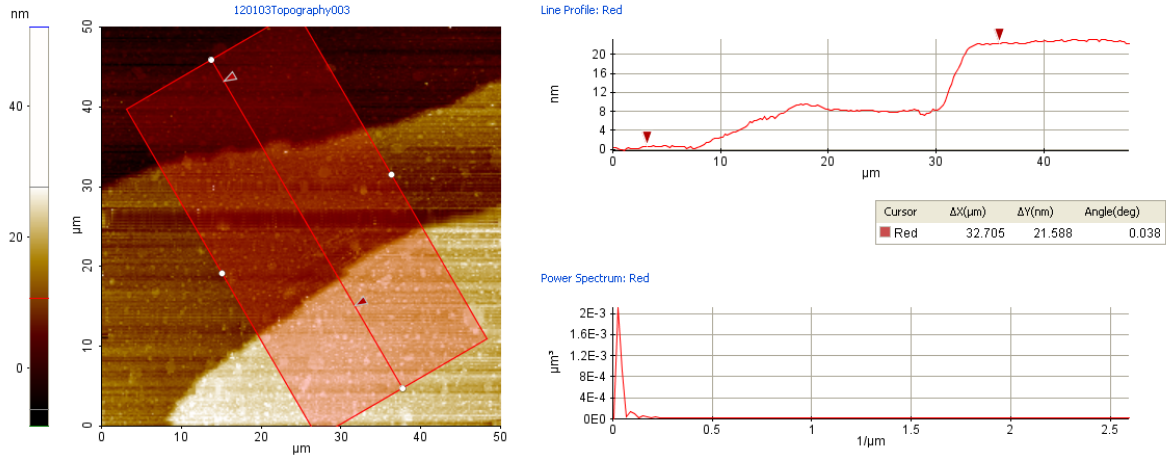
Figure 3.11: AFM of the Py/Pt bilayer on Si substrate. AFM line scanning indicates that the Pt layer is 8 nm thick whereas the Py layer is 14 nm thick. However we expected 12 nm Pt and 10 nm Py thicknesses.
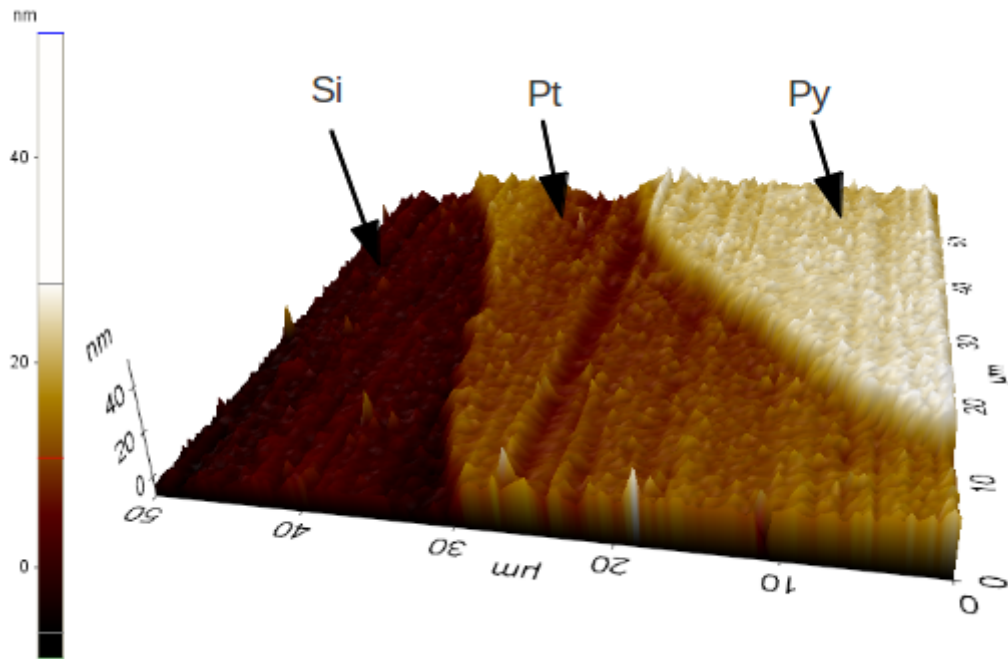
Figure 3.12: $50\,\mu m \times 50\,\mu m$ AFM scan of the Py/Pt/Si. Unwanted surface defets were removed by the AFM user interface program. In the 3-D image the color conrast indicates the height. Pt. Py and Si layers are recognizable.

3.1.2 Sample stage and sample holders

For the electrical measurements of ISHE, we designed and produced two different sample holders: one for the measurements which was done in microwave cavity and other for multifrequency measurements. However, we used only one sample stage for those sample holders. The stage is shown in Fig. 3.13.
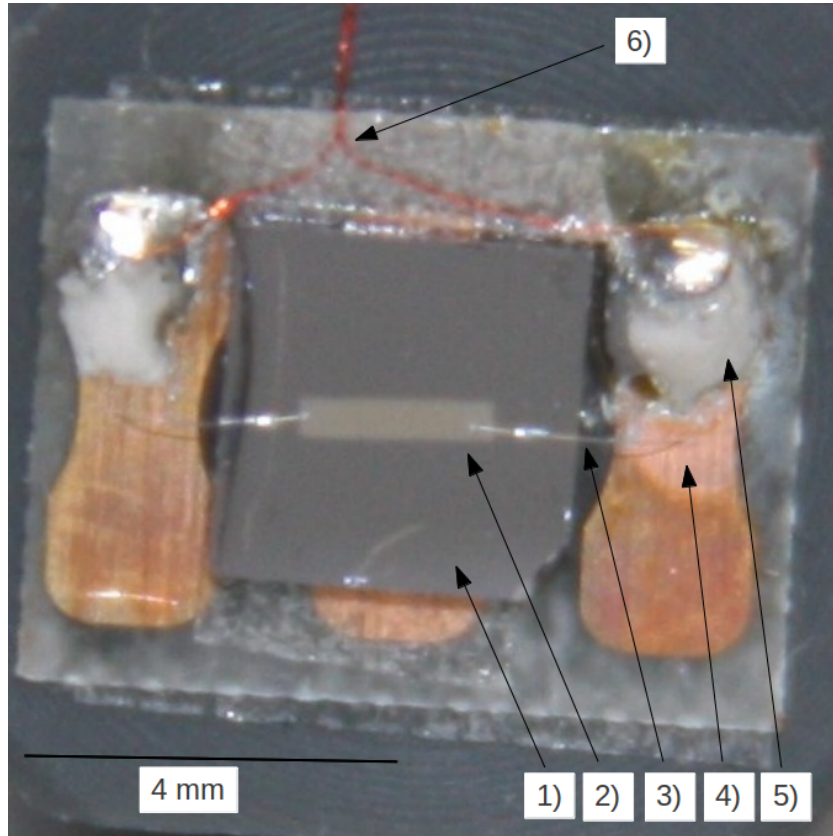
Figure 3.13: The sample stage; 1) thermally oxidized silicon substrate 2) Pt/Py bilayer 3) $15\,\mu m$ Al electrodes 4) Cu bondable terminals 5) Sn/Pb solder 6) $15\,\mu m$ Cu leadwires

Firstly, approximately $6 \times 6\,$mm piece from bondable terminals with epoxy backing (Micro-measurements, type; CEG-75C) was cut and cleaned with ethanol. The bondable terminals have a $0.036\,$mm thick copper foil laminated on epoxy-glass laminate. The insulator layer on the copper foil on the wire bonding position was polished. Then the silicon substrate with the Pt/Py bilayer system was fixed on the terminal by a double sided tape (Tesa AG, type; Doppelband Fotostrip). The electrodes ($25\,\mu$m diameter AlSi-wire (Heraeus, DR-1%Si) were attached between the edges of Pt and the copper foils by a wire bonding machine (Kulicke and Soffa Industries INC.). Finally the $30\,\mu$m diameter copper leads were soldered onto the copper foils on the terminal. Before sol-

dering, the leads were fixed on the terminal base (laminate surface) in order to avoid any circular cable loop, and only the ends of the cables are moved onto the copper foil.

The major advantage of using a such stage is that, one does not need to remove the contact bonds from the sample in order to carry out the measurements with different sample holders. Melting the solder joints is enough to free the entire stage from the sample holder, and the same stage can be attached to another position.

Sample holder for microwave cavity measurements
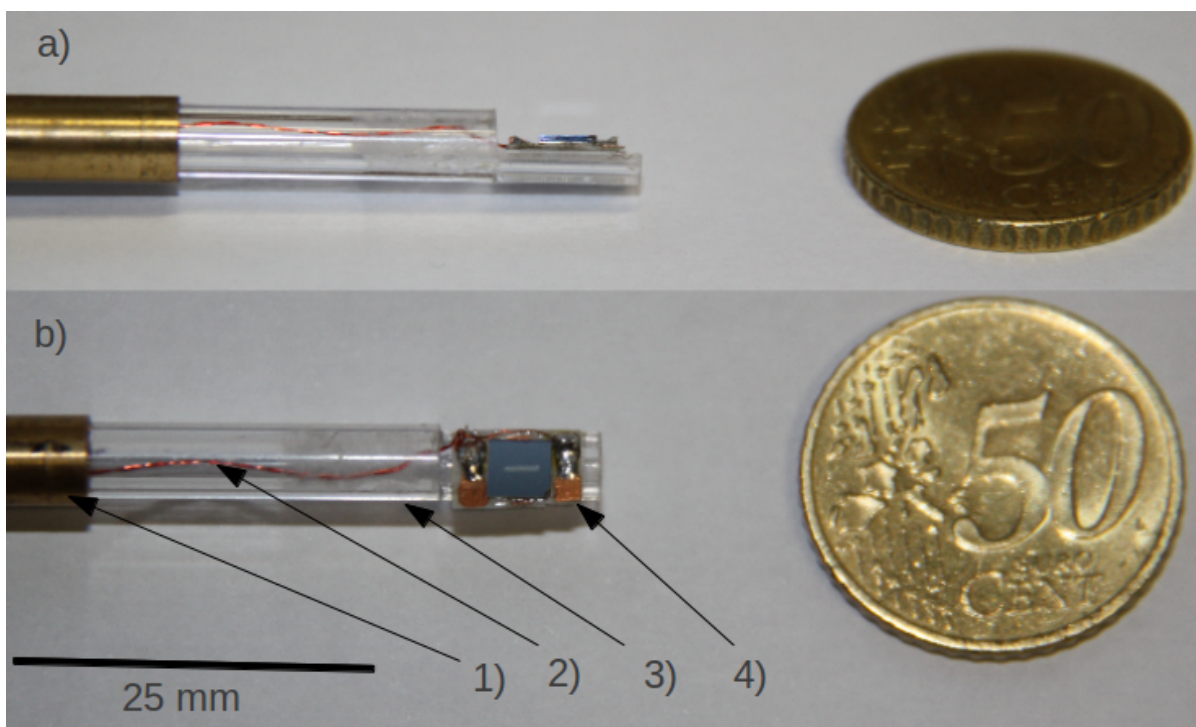
Figure 3.14: a) side view of the sample holder b) over view of te sample holder 1) brass tube 2)twisted copper leadwires 3) plexiglass tube 4) sample stage

Angular, temperature, and microwave power dependent measurements were carried out in a microwave cavity in which the sample is placed in the center of the cavity. The sample holder that is shown in Fig. 3.14 was produced for this purposes. Firstly, a $20\,cm$ long and a $6\,mm$ diameter brass tube was cut, and one end of the tube was polished for enlarging the inner diameter. Half of the first $6\,mm$ of the $6\,cm$ plexiglass tube ($5\,mm$ diameter) was removed and polished and cleaned. Then, the plexiglass tube was fixed to the brass part, and the twisted leadwires ($0,1\,mm$ diameter) were inserted into the

tube. The sample stage was attached to the half-cut plexiglass surface, and finally the twisted wires were soldered to the copper foils.

With this design, we were able to measure the V_{ISHE} signal which was produced by the bilayer film system inside the microwave cavity.

Sample holder for multifrequency measurement
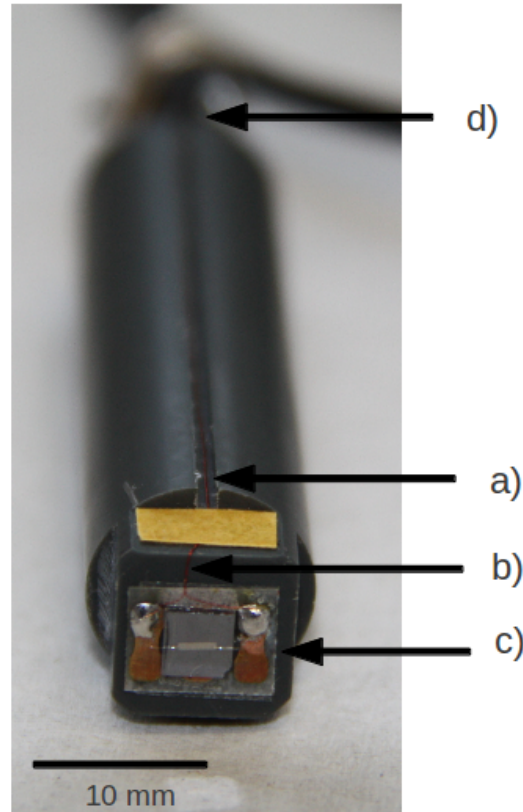
Figure 3.15: The sample stage holder for frequency dependence measurement. a) 1 mm wide and depth, lead wire-guide b) 0.05 mm copper leads c)sample stage d)copper leads to coaxial cable connection.

We have constructed the sample holder that is shown in Fig. 3.15 for frequency dependence measurements. Firstly, a PVC-Polyvinyl chloride rod with a 13 mm diameter was cut with a 55 mm length. A rectangular shape was given to the front part, on which the sample stage was fixed by a double sided tape. A wire-guide along the rod was opened for the copper leads. The leads were soldered to the sample stage at the front and soldered to the coaxial cable which was connected to the Lock-in amplifier.

3.2 Ferromagnetic resonance spectrometer

FMR is a spectroscopic technique to probe the magnetic properties by detecting the precessional motion of the magnetization in a ferromagnetic sample. In a macroscopic view, the applied static magnetic field H_{dc} causes the total magnetic moment to precess with a Larmor frequency around the direction of the local field H_{eff}. If the sample is exposed with a transverse microwave field h_{MW}, and if the microwave frequency matches the Larmor frequency, the resonance condition is fulfilled, and the microwave power is absorbed by the sample. The magnetization dynamics in this process is described by the Landau-Lifshitz-Gilbert equation 2.5 as discussed in section 2.1.
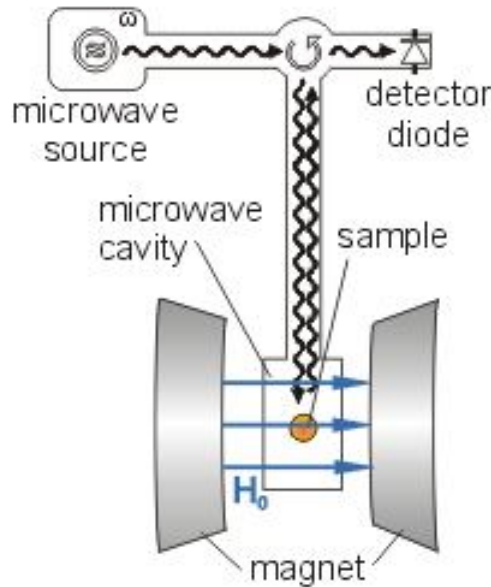
Figure 3.16: The basic FMR spectrometer. [7]

With this technique, the microwave power absorption is measured. The resonance signal has a Lorentzian lineshape and the resonance field H_{FMR} depends on the angular orientation between sample plane and the magnetic field direction, film-anisotropy parameters, g-factor, and the magnetization of the sample.

The FMR spectrometer consist of following main components: a source of electromagnetic radiation (microwave source), microwave cavity, electromagnet, detector. To acquire a spectrum under a fixed microwave frequency, one can sweep the static magnetic field and measure the amount of radiation which passes through the sample with a detector to observe the spectroscopic absorption.

In conventional FMR measurements, a microwave bridge houses the microwave source and the diode (detector). The microwave cavity is connected to the bridge by a waveguide. The cavity is placed in the center of the electromagnet poles. When the microwave source is switched on, the waves travel along the waveguide and reach the microwave cavity. When the frequency of microwaves is tuned to the cavity, the cavity resonates. The incoming waves are stored and some are absorbed by the side walls of the cavity by producing electrical eddy currents. No microwaves are reflected back. The ratio of stored to dissipated energies give the efficiency or the quality factor Q of the cavity:

$$Q = \frac{2\pi(\text{energy stored})}{\text{energy disipated}}.$$

(3.1)

Inside the cavity, a standing wave is built up as a consequence of resonance. Standing electromagnetic waves have their electric and magnetic field components exactly out of phase. This means that, inside the cavity where the electric field is maximum the magnetic field is minimum and vice versa. Therefore, the sample must be placed in the position where the magnetic field is maximum, since the magnetic field drives the absorption in FMR. This particular position gives the largest signal and the highest sensitivity.
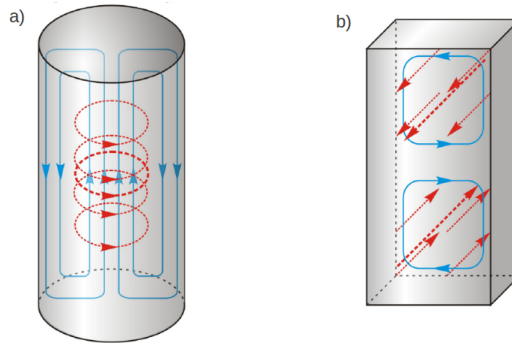
Figure 3.17: The spectral distribution of the electric (red) and magnetic field lines (blue) inside a) cylindrical and b) the rectangular microwave cavities.[35]

By an additional part called iris which is positioned between waveguide and the cavity, microwaves are coupled into the cavity. The iris controls the microwave amount that will stay inside or will be reflected by the cavity by matching or transforming the impedance of the waveguide and the cavity.

When the resonance conditions are fulfilled for the ferromagnetic sample, the sample absorbs the microwave energy and as a result, the coupling differs since the absorbing sample changes the impedance of the cavity. The cavity is therefore no longer critically coupled and the microwaves are reflected back to the waveguide and construct there a standing wave. Due to the microwave circulator the reflected microwaves can only travel toward the detector diode and by diode the microwaves are converted into an electric signal. Therefore, the reflected power actually is the one which is measured in this technique.

Signal processing

In FMR spectroscopy, phase sensitive detection technique is used, in order to increase the spectrometer sensitivity. A Lock-in amplifier (phase sensitive detector) is employed on for purposes. With this technique, the noise from the detection diode can be significantly reduced. Moreover, the baseline instabilities due to the drift in DC electronics can be eliminated. An additional advantage is that the lock in amplifier encodes the FMR signal to make it distinguishable from the source of noise or the environmental interference.

The signal processing works as follows: at least one quantity, either microwave amplitude or the magnetic field is modulated at a modulation frequency. In conventional FMR experiments, the modulated quantity is usually the magnetic field. In this case the external magnetic field has two components; one is the static magnetic field and other is the alternating field with much smaller in amplitude and sinusoidal shape. At resonance, the field modulation quickly sweeps through a part of the signal, and the microwaves reflected from the cavity are amplitude modulated at the same frequency. Therefore, the FMR signal, which is nearly linear over an interval of modulation amplitude, is transfered to a sine wave with an amplitude proportional to the the slope of the signal. As a result, one obtains the first derivative of the microwave absorption signal. Therefore, the lock-in amplifier requires a reference signal from the modulated quantity and then produces a dc signal proportional to the amplitude of the modulated FMR signal. Basically, it compares the modulated signal with a reference signal and accepts only the same frequency and phase as the modulation and other frequencies and phases are cut out by the inner electronics. The technique increases the sensitivity, but the modulation amplitude, frequency and the time constant must be chosen correctly.

In the following, the experimental setups for each measurements are shown.

3.2.1 Conventional FMR spectrometer with a microwave bridge
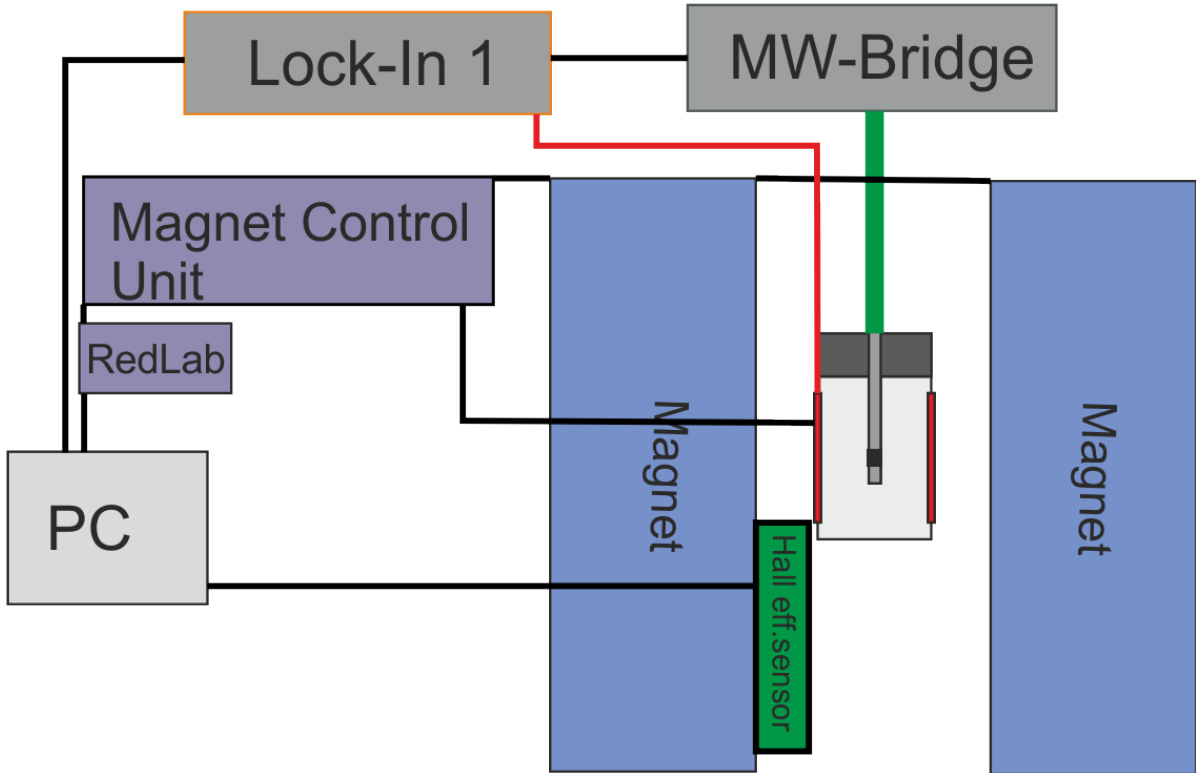
Figure 3.18: The block diagram of the conventional FMR Spectrometer with microwave bridge is shown. The black, red and green connectors represent the electrical cables, the reference signal cable and the waveguide respectively.

Conventional Ferromagnetic resonance measurements were performed using the setup block diagram that is shown in Fig. 3.18. The main elements in this setup are:

- Electromagnet with an air gap of 18 cm powered with a power supply Brucker B-MN 120/125. The power supply is controlled by the computer through a control unit. The computer communicates with the control unit via a dc/ac converter (RedLab USB DAQ Unit from the company Meilhaus Electronics). The magnet can produce at the center nearly 1.4 T uniform static magnetic field. It is cooled by water.

- A dual phase, digital Lock-in Amplifier Stanford Research SR830

- A digital gaussmeter (LakeShore 425) to measure the magnetic field via a Hall effect sensor

- A Varian E102 Microwave Bridge which includes an X-Band reflection type klystron, a reference arm, an attenuator, a microwave detector and an AFC-Automatic frequency control unit. The bridge generates microwave radiations in a frequency range of 8.8 to 9.6 GHz with a power up to 200 mW.

- A microwave cavity, with field modulation coils on the side walls

- A goniometer with 0.5° resolution

- The PC is used to control and read the lock-in Amplifier, the gaussmeter, and the magnet.

An electromagnet was used as a dc magnetic field source. The electromagnets can produce up to 1.4 T uniform dc magnetic field at the center. The sample holder was inserted into the cavity, and the waveguide was constructed between the cavity and the microwave bridge. In order to reduce mechanical vibrations, waveguide stabilizers were used to fix the waveguide between the magnets. As shown in Fig. 3.18 a Hall effect sensor was placed close to the air-gap center, where the cavity is located, and monitored by the gaussmeter. The gaussmeter which reads the magnetic field was then connected to the computer via a USB port. The modulation frequency, in the field modulation technique, is supplied by the modulation coils on the cavity, and the modulation frequency can be set by the control unit of the magnet. These coils were connected to the Lock-in amplifier reference input and the Lock-in was connected to the computer via a GPIB port. In our measurements we used 100 kHz modulation frequency and a 10 G modulation amplitude unless otherwise mentioned. The diode inside the bridge which measures the reflected microwave power was connected to the lock-in, and this signal is the one which is measured in conventional FMR measurements.

After tuning the cavity to its resonance frequency, we set the dc magnetic field sweep range, and the field modulation frequency, the amplitude, and started the conventional FMR measurements with a chosen microwave power. The whole system was controlled via a computer program (custom Labview program by Florian Römer) and the resulting spectra were monitored by the Labview user interface.

3.2.2 Signal generator-based setup
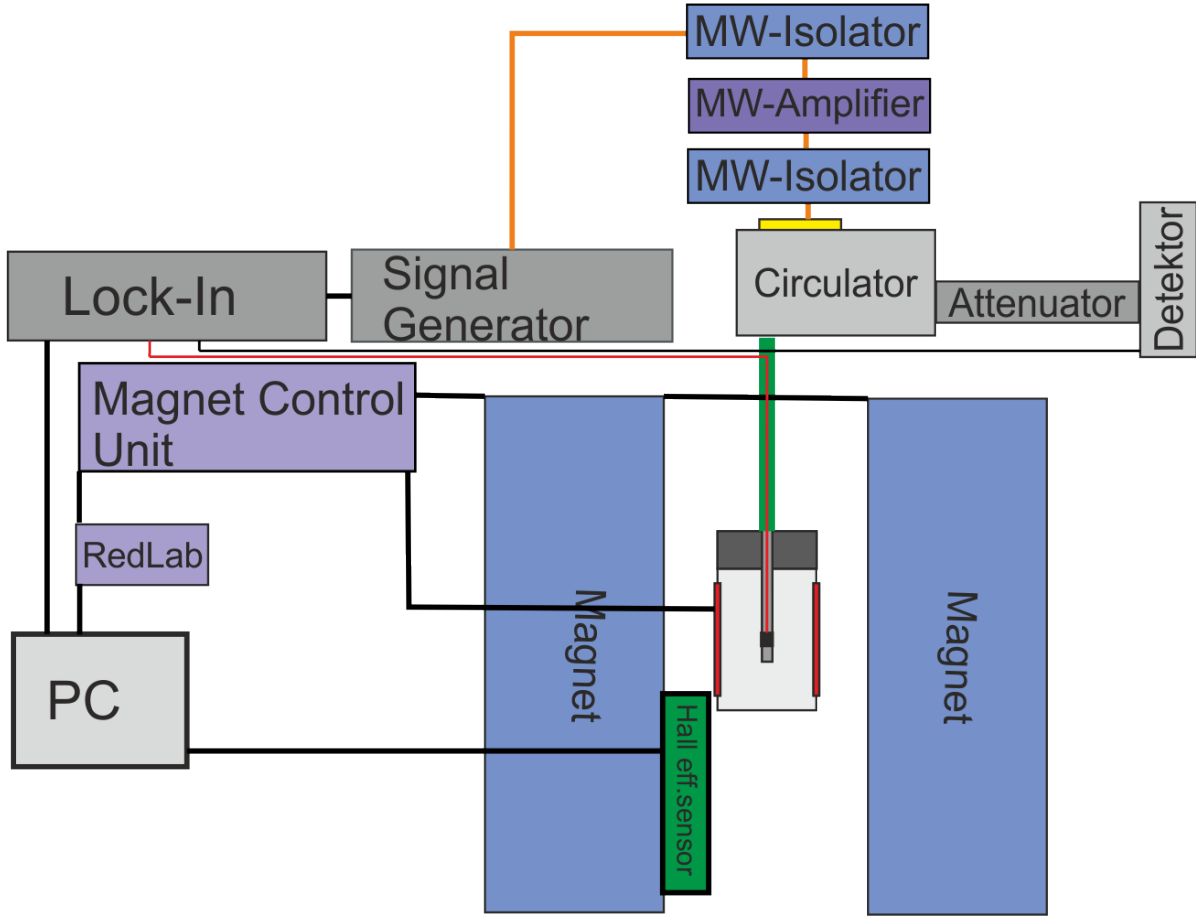
Figure 3.19: The block diagram of the setup for the V_{ISHE} measurements is shown. The black, red and green connectors represent the electrical cables, the reference signal cable and the waveguide respectively. In this setup we also used microwave cable which is shown with orange color. The yellow box indicates the right angle waveguide to coaxial adapter.

The setup that is depicted schematically in Fig. 3.19 was used for the angular, temperature and power dependence of V_{ISHE} measurements. The main structural difference is, instead of microwave bridge as a microwave source, a signal generator was employed, and the microwave waveguide system was modified with several microwave circuit elements. The reason for using this system is because we wanted to use microwave amplitude-modulation as the measurement technique instead of magnetic field modulation.

Similar to the previous setup shown in Fig. 3.18, an electromagnet, a Lock-in amplifier, a gausmeter and Hall effect sensor, cavity, control unit and PC were employed in this setup. Additionally, we have used following instruments:

- Signal generator (Rohde & Schwarz, SMR 20) with 10 MHz to 20 GHz frequency range

- Microwave power amplifier, X-band GaAs FET power amplifier (Kuhne Electronics, Type: KU 093 MM) with 8.5-10 GHz frequency range

- SN/01 right angle waveguide to coaxial adapter

- Microwave isolator (Aerotek, I12-1L1FF) in a range 7-12 GHz and 17 dB isolation

- Microwave attenuator and a circulator

The setup was built up and operated as follows: The signal generator which produces the microwaves is connected to a microwave power amplifier by a 50 Ohm coaxial rf-cable (Harbour Industries, Type; CXC FT4) which transports the microwaves. A microwave isolator is placed between the cable and the amplifier in order to avoid any reflected wave to enter the signal generator. The amplifier amplifies the microwave power. The amplified microwaves are transported to the right angle waveguide to the coaxial adapter via an other rf-coaxial cable. An additional isolator is placed between cable and the amplifier. The adapter is connected to a microwave circulator. The circulator is a three -port device used to control the direction of the signal flow. The first port is the microwave entrance for the incoming waves, the second is for the waveguide which is connected to the cavity and the last port is for the reflected microwaves which come from the cavity and are directed into, first to the attenuator and then to the detector. In the absence of resonance in the cavity, all microwave power is either stored or absorbed by the cavity. However, at resonance the reflected power passes the circulator with indicated direction only (rotation only) and is eventually absorbed by the detector. This detection is the conventional FMR measurement with microwave amplitude modulation.

In V_{ISHE} measurements that we have performed with this setup, we insert the sample holder into the cavity. Here, instead of measuring the reflected microwave power by the detector, we measured the V_{ISHE} signal electrically between both ends of the Pt layer as shown in Fig. 3.20. Therefore, the measured signal is the potential between the leads instead of the reflected microwave power on diode. The measurements are carried out as follows: After tuning the cavity, 70 % microwave amplitude modulation is switched on. Because the modulated quantity is the microwave amplitude, the reference signal for the lock-in was taken from the signal generator (low frequency output) and the V_{ISHE} signals is monitored. the same steps done for each temperature, microwave power and

sample -magnetic field orientations for related measurements.
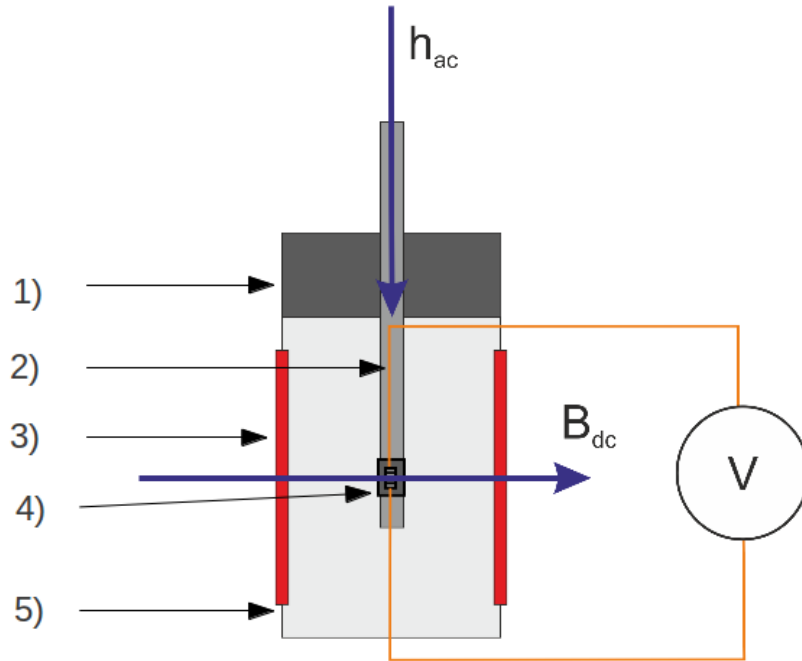
Figure 3.20: The block diagram of the electrical measurement in cavity. The applied magnetic fields (h_{ac} indicates the microwave field and B_{dc} is the static magnetic field), the cavity parts, sample and the sample holder and measurement circuit are shown. 1) the goniometer, 2) the sample holder, 3) field modulation coils, 4) Py/Pt/Si sample 5) microwave cavity

The angular manipulation of the sample holder is done manually by a goniometer, which is attached to the top of the cavity (as is shown in Fig. 3.20). Both leads are carried out of the cavity through the sample holder tube as described earlier.
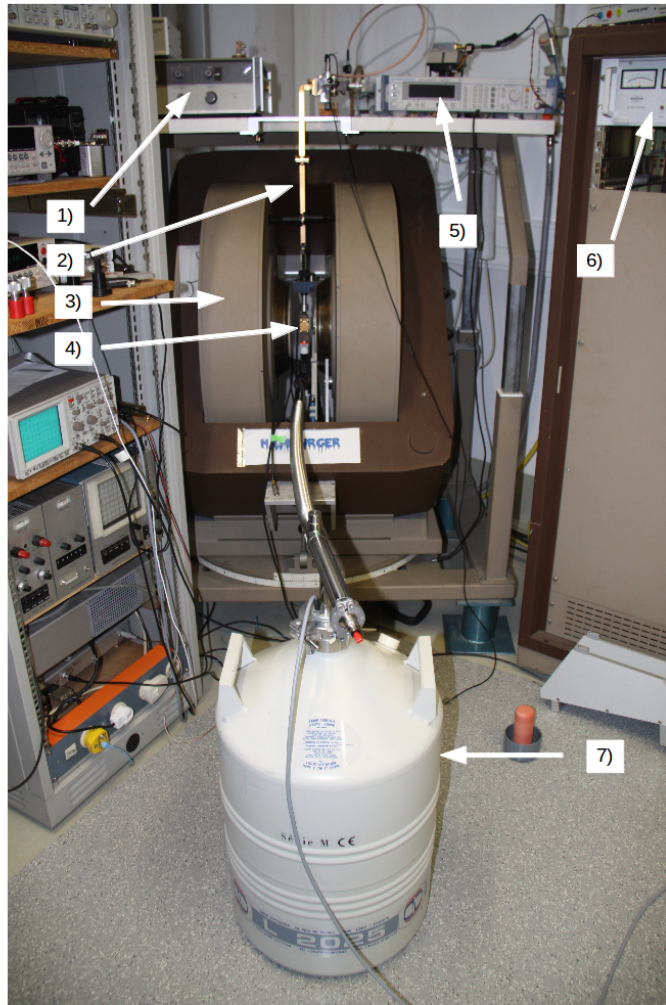
Figure 3.21: Temperature dependeny measurement setup 1)Microwave bridge 2) waveguide 3)electromagnet 4) cavity in the air gap of the magnets 5) the signal generator 6) power unit of magnet 7) nitrogen container

In order to manipulate the temperature inside the cavity for temperature dependent studies or, in order to keep the cavity temperature constant in power dependent measurement to eliminate additional heating with increase in power, we have used several additional equipments. The setup is shown in Fig. 3.21, where the setup that is shown in Fig. 3.19 is modified with following equipments:

- Thermocouple

- Nitrogen container

- Temperature regulator.

This cooling system utilizes liquid nitrogen which is allowed to evaporate. The temperature of the cavity is measured with thermocouple, and the temperature is monitored by a temperature regulator unit. When the temperature set point is below the ambient temperature of the cavity, the cryogenic control valve opens and nitrogen gas enters the cavity. The nitrogen flow is maintained by the exit holes in the cavity.

3.2.3 Frequency dependent measurements with a semi-rigid cable
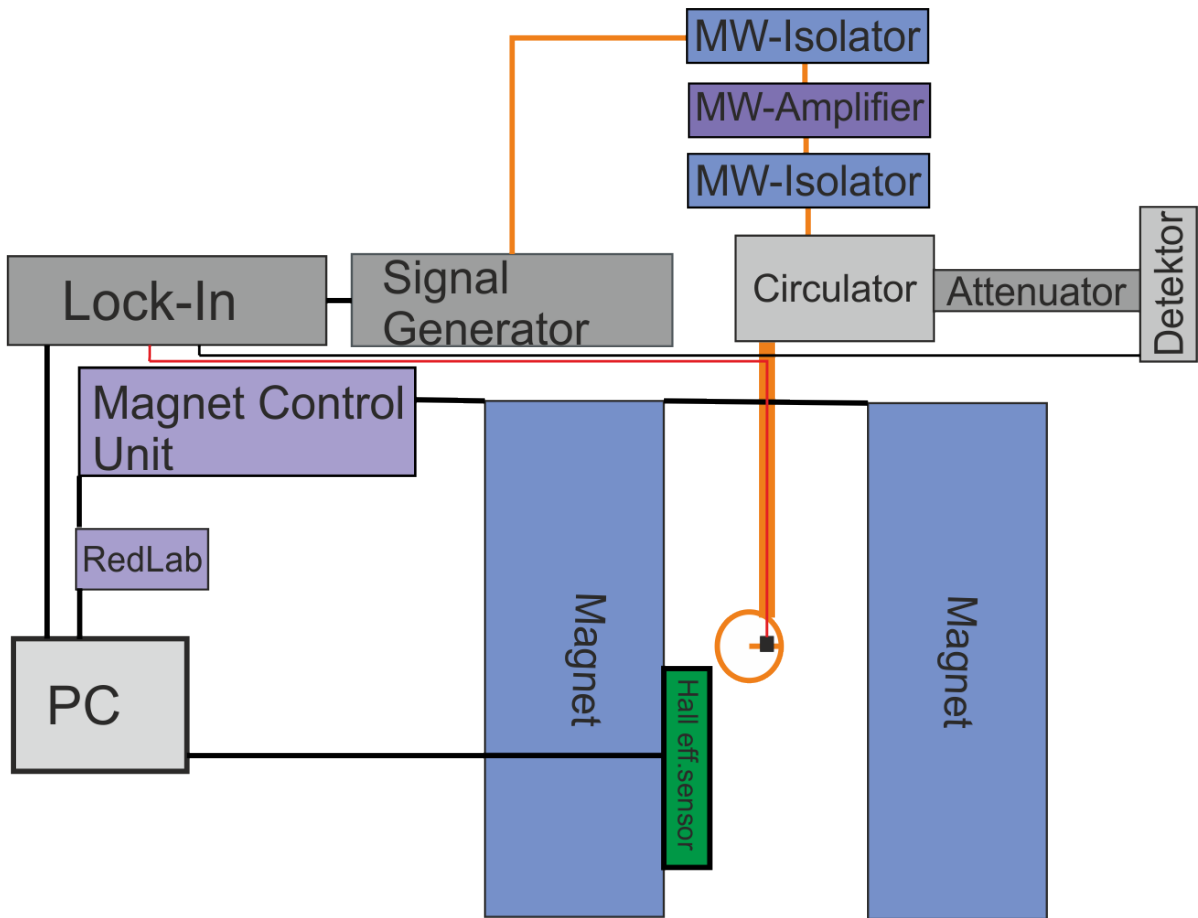
Figure 3.22: The block diagram of the setup for the frequency dependence of V_{ISHE} measurements is shown. The black, red and orange connectors represent the electrical cables, the leadwires and the microwave cable respectively. The circle in the magnet air gap represents the microwave coaxial cable short cut.

For the frequency dependence of V_{ISHE} measurements, we modified the set up as shown in Fig. 3.22 with following microwave circuit elements;

- Microwave isolator (Ditom Microwave INC., D3I-6012/SN2244) with a frequency

range 6-12.4 GHz

- Microwave circulator (Ditom Microwave INC., D3C-6012/SN2095) with a frequency range 6-12.4 GHz

- Microwave attenuator (66109/AA77053) with a frequency range 10dB/18 GHz

- Zero-Bias Schottky Diode Detectors (Ohio Microwave LLC., DZM-265AB/SN409833) with a frequency range 10 MHz-16.5 GHz

For frequency dependent V_{ISHE} measurements, no waveguide is used. Instead all microwaves are transported via microwave coaxial cable. It should be noted that instead of a cavity, during these particular measurements, we used a coaxial semirigid microwave cable (SRMC) with a diameter of 2 mm which resonates the microwaves. In order to produce a high-frequency magnetic field in the film plane and perpendicular to the external field, the SRMC is electrically shorted at its end by connecting the inner conductor and the ground shield of the SRMC (see Fig. 3.22). The direction of the short is oriented perpendicular to the external magnetic field, $\mathbf{B}_{dc}$. The electric field of the microwave induces a current along the short, which results in a magnetic field around the short and perpendicular to $\mathbf{B}_{dc}$. Detailed information for the semi-rigid cable technique can be found in Ref.[15], [37] and [38].

The sample is placed very close to the SRMC (as shown in Fig. 3.23-a). The magnetic field of microwaves are orthogonal to the external static magnetic field and to the electrodes that are attached to the edges of the Pt layer. Although this system is designed as a FMR spectrometer, we use it only to bring the Py-layer into ferromagnetic resonance. The measured quantity is the V_{ISHE} signal. Therefore, we employ the microwave detector for monitoring the microwave reflection in order to retain the microwave cable at its resonance frequencies. The microwave amplitude is modulated with a 70% amplitude modulation. Therefore, the reference signal for the lock-in amplifier is taken from the signal generator. At a constant frequency the static magnetic field is swept and the V_{ISHE} signal around the resonance field is measured.

This system allows us to take measurements in a range of 8-12 GHz which is the working range of the amplifier. With a large bandwidth amplifier, isolator, circulator and attenuators one can perform the same measurements with higher and lower frequencies.
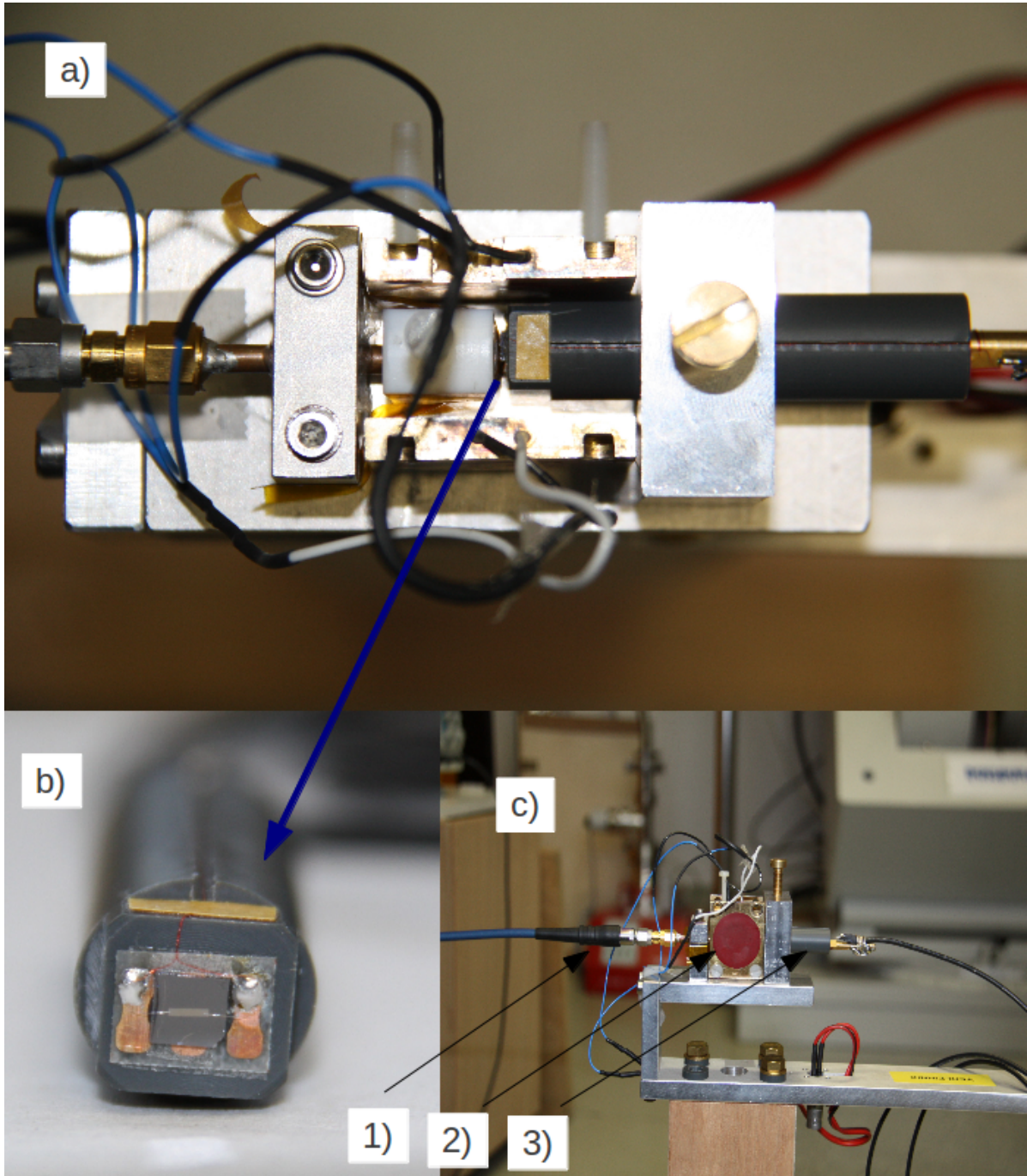
Figure 3.23: a) an overlook of the apparatus which includes the shortcut cable and the sample holder and the field modulation coils , b)a front look of the sample holder and the sample stage, c) a side view of the apparatus; 1) the microwave cable 2) field modulation coils, 3) the sample stage with leadwires

4 Results and discussion

In this work, the electromotive force V_{ISHE} induced by the spin pumping was investigated. In this system, the magnetization of the ferromagnetic Py layer is driven into ferromagnetic resonance (FMR) and relaxes by emitting a spin current into the adjacent paramagnetic Pt layer. At first, we observed the angular dependence of V_{ISHE} signal by changing the inclination of the sample to the applied field. Secondly, the change in V_{ISHE} relative to the applied microwave power was investigated. Afterwards the effects of temperature and microwave frequency was examined. The results are shown in following sections.

In this chapter, each section starts with describing the fabrication method of the samples. It should be noted that, we did not used the same sample for every measurement and due to the change in sample geometry and material concentrations, the measured V_{ISHE} value varies. For the electrical measurements, a lock-in amplifier was utilized. The sensitivity of the lock-in was set to $100\,nV$ thus the voltage error in each measurement is defined by this value.

As it is shown in figure 4.1, the amplitude of induced electromotive force V_{ISHE} is calculated by measuring the peak value from the baseline. Due to the measurement technique each V_{ISHE} spectra had an offset which has no physical meaning. In this thesis, these offset were subtracted from the baseline in the graphs that are shown.
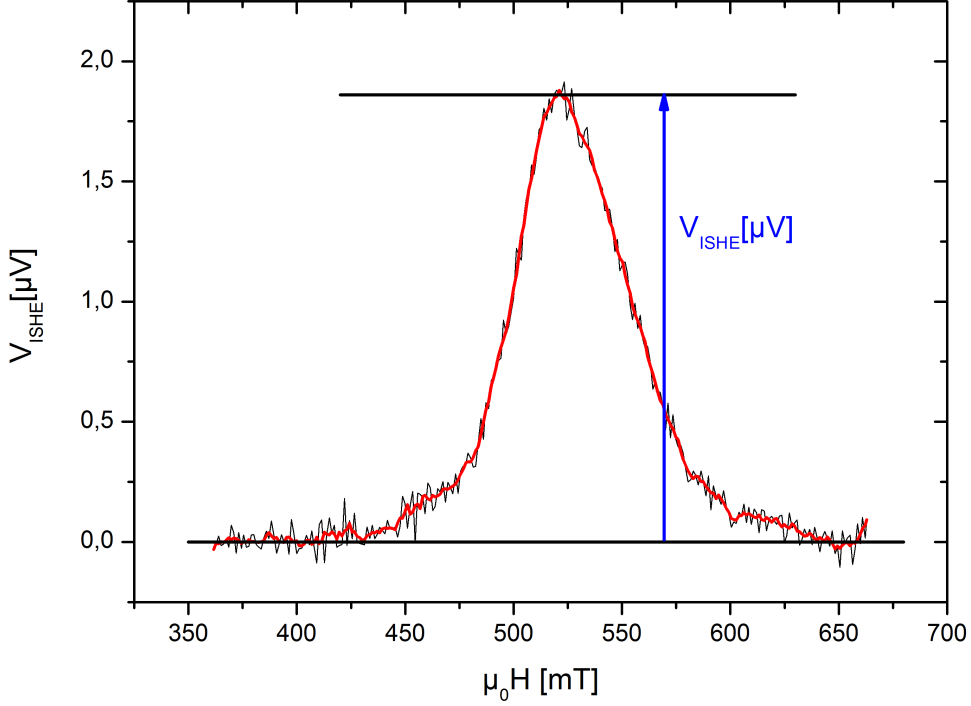
Figure 4.1: The amplitude of V_{ISHE} signal.

For the ferromagnet-paramagnet bilayer system, we decided to use permalloy Py as a ferromagnetic layer. This is due to the magnetic properties of the alloy. The permalloy that we used has about 20 % Fe and 80 % Ni content. Especially, Py with this concentration, has no resulting crystal anisotropies. Therefore, the only significant magnetic anisotropy for polycrystalline Py is the magnetic shape anisotropy. This means that the magnetization vector of the ferromagnetic layer aligns parallel with the effective field in the film plane elsewhere the shape anisotropy determines the the relation between **H** and **M**, except the exact out-of-plane orientation.

As a paramagnetic layer Pt was chosen. Because Platinum is one of the most promising materials for metallic SHE. For an inverse spin Hall effect experiment one needs to use an effective spin sink paramagnetic metal for more efficiency. A normal-metal film can be a good spin sink only with a high spin-flip probability. Pt has a large atomic number $Z = 78$, and 2 electrons (p or d electrons) in the conduction band, which are hybridized with d orbitals. These properties allow Pt to produce large spin orbit coupling [45]. Therefore, Pt is a good spin sink and thus an effective spin current into

charge current converter. On the other hand, the light metals, such as Al, Cr, and Cu, as well as heavier metals with only s electrons in the conduction band, such as Ag, Au, and Ta are less effective spin sinks since these metals have a relatively small spin-orbit coupling [45]. At the moment, the consensus for the origin of the SHE in Pt is that both intrinsic (spin orbit interaction of a host metal) and extrinsic effects (skew scattering and side jump effect via the spin orbit interaction of nonmagnetic impurities [18]) are likely to contribute to the measured spin Hall conductivities, although experimentally it is not possible to differentiate the two different physical mechanisms at the moment [46].

As a substrate, thermally oxidized Si was used. However, in advance we have investigated the possible effect of both Si and GaAs on ISHE by measuring ferromagnetic resonance of the same thin film structures which were grown simultaneously on GaAs and Si substrates. No any significant FMR linewidth deviation was observed. Any difference in linewidth would imply the change in damping constant which means a change in effective spin pumping through the Py/Pt interface. The reason of no change is due to the fact that the spin current injected into the Pt layer was completely dissipated through the layer and no current reached to the substrate-Pt interface because the Pt layer thickness kept larger than the spin flip distance $\lambda_{sd} < t_N$.

4.1 Out-of-plane angular dependence of ISHE signal

For the magnetization characterization of the sample we have performed the out-of-plane angular dependence of ferromagnetic resonance measurements. In Figure 4.2 the angular dependency of ferromagnetic resonance spectra of 10-nm-thick ferromagnetic Py and 10-nm-thick paramagnetic Py bilayer is shown. For the measurement, the sample system was placed near the center of a TE_{011} (cylindrical) cavity at which the magnetic-field component of the microwave mode is maximized while the electric-field component is minimized. During the measurement, a microwave mode with frequency $f = 9.81\ GHz$ exists in the cavity with $9.8\ mW$ microwave power and 2600 quality factor. External magnetic field was swept from 0 to $1{,}6\,\mathrm{T}$ for each angle orientation. Here, θ_H is the angle that external magnetic field makes with the film plane normal.
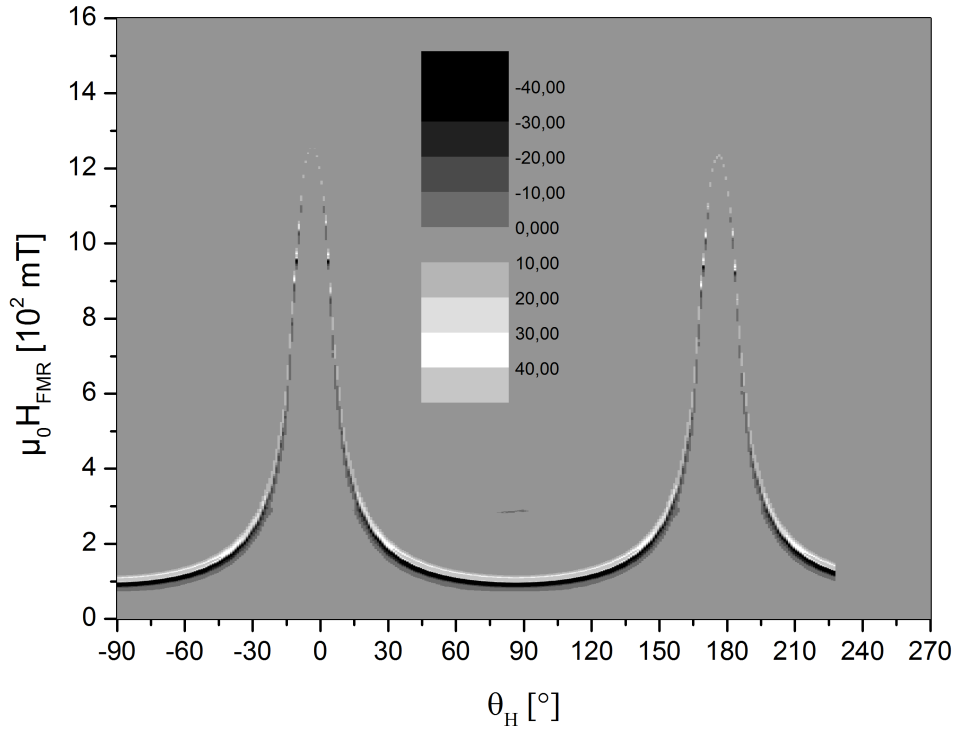
Figure 4.2: The out-of-plane angular dependence of ferromagnetic resonance spectra of 10-nm-thick ferromagnetic Py and 10-nm-thick paramagnetic Pt bilayer. $\theta_H = 0°$ was chosen to be out of plane direction (hard axis). The color contrast here represents the reflected microwave power intensity from the cavity.

As a measurement technique a field modulation with $100\,\mathrm{kHz}$ modulation frequency and

10 G modulation amplitude was used. The resulted spectra for each angle was plotted in a 3D contour plot which is shown in Fig. 4.2. The color contrast here represents the reflected microwave power intensity from the cavity. Due to lock-in detection, the derivative of the absorption signal with respect to the magnetic field is measured and the absorption signal is proportional to the imaginary part of the high-frequency susceptibility χ''.
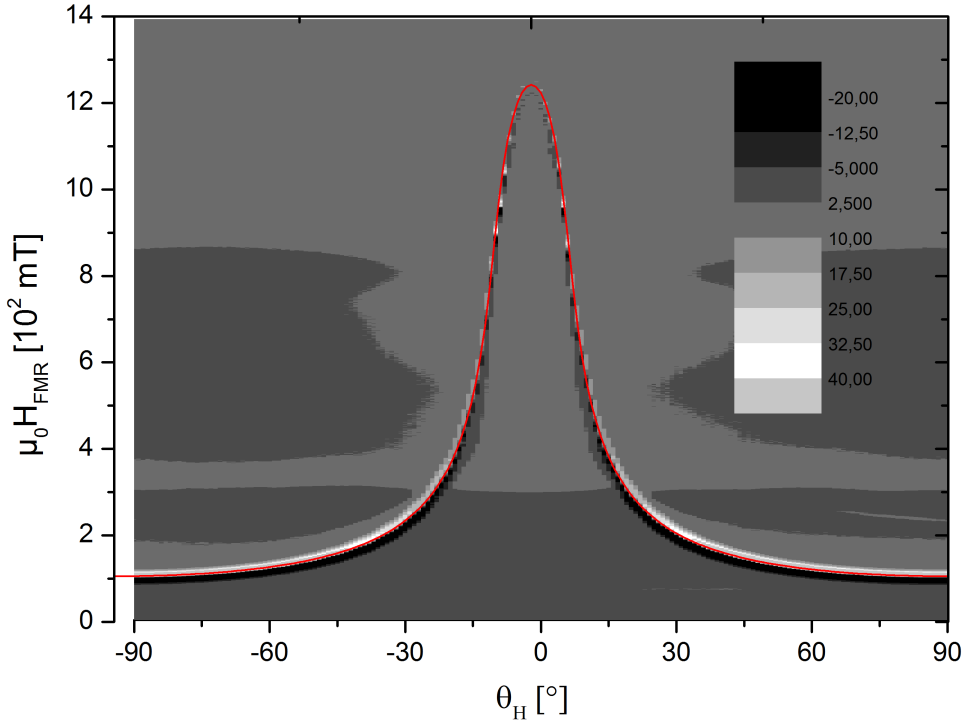
Figure 4.3: By fitting the data the effective magnetization and the g-factor for Py film was extracted.

Since the magnetocrystalline anisotropy in Py is negligibly small, the magnetization in the Py layer is uniformly aligned along the magnetic field direction when $\theta_H = 0°$ and $\theta_H = 90°$. The in-plain angular dependence measurement for the same sample was also completed and we have concluded that, expect from the shape anisotropy, other anisotropies are negligible. In order to find the effective magnetization M_{eff}, the out-of-plane measurement (4.2) was fitted by a fit program PolarC Properties (Dr. anatoli Anisimov, April 2004, Licensed to Prof. Dr. M. Farle). In the program g-factor and effective magnetization M_{eff} of Py are used as fit parameters. By the fit program we obtained g-factor $g = 2.15$ and $M_{eff} = 0.916\ T$. We have especially performed this

measurement and fitting in order to obtain the variation of θ_M from θ_H and resulted relation is shown in Fig. 2.14.

In section 2.4.2 the theoretical, θ_H dependence of electromotive force V_{ISHE} is shown. In this part, we compare it with the experimental results. During the measurements, the sample was placed to the center of TE_{102} microwave cavity, a microwave mode with frequency $f = 9.52\ GHz$ exists inside. As a microwave source a signal generator was used. As a measurement technique an amplitude modulation was employed. As explained earlier, in this technique the modulated quantity is the microwave amplitude itself with $100\ kHz$ modulation frequency and 70% modulation amplitude. Therefore the reference signal for the lock in amplifier was taken from the signal generator. All the angular dependence of the electromotive force measurements were performed at room temperature under 96.2 mW microwave excitation. The angular orientation was manipulated by a ganiometer which was attached to the cavity and sample holder. The resulted spectra are shown in Fig. 4.4.
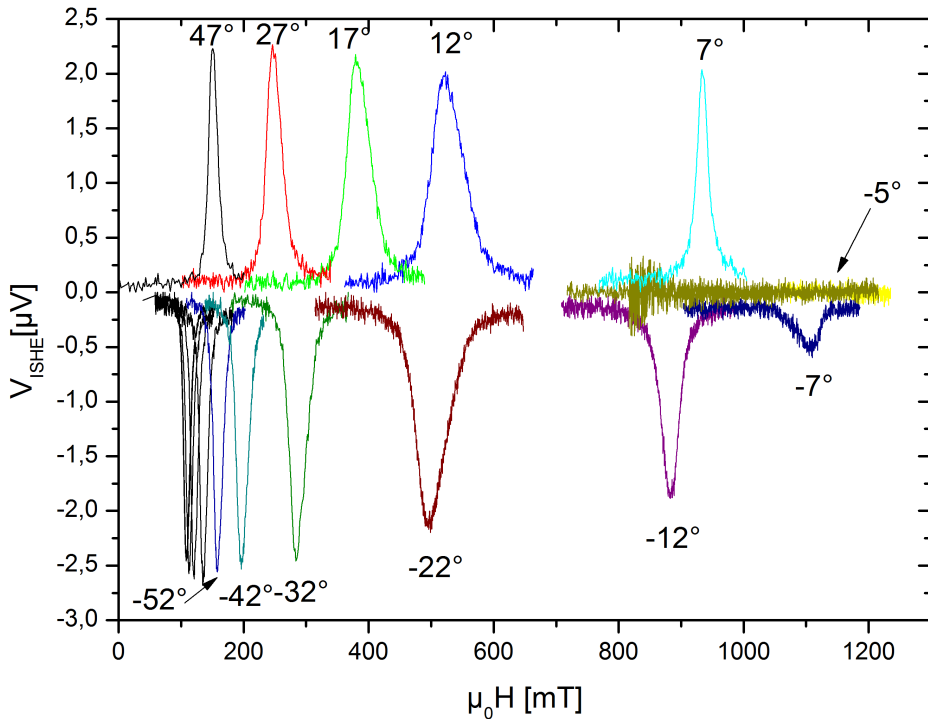
Figure 4.4: The variation of V_{ISHE} signal with respect to θ_H. θ_H values are shown above each spectra.

In this measurement, the external dc magnetic field was applied with an angle of θ_H to the normal of the film plane. Fig. 4.5 shows the magnetic field positions where the V_{ISHE} peaks occur for each θ_H orientation. As the theory indicates, when f_{FMR} and H_{FMR} fulfill the ferromagnetic resonance condition, $\mathbf{J}_s$ is resonantly injected into the paramagnetic Pt layer. The spin polarization vector σ, produced by the spin pumping mechanism is directed along the magnetization-precession axis. Therefore, σ determines the sign of V_{ISHE}. The amplitude of V_{ISHE} depends on θ_M orientation and by altering θ_H, as it is expected the amplitude of electromotive force remain almost constant about 20° away from the exact out-of-plane angle (namely $\theta_H = 0°$ orientation). Because in this region, due to the magnetic shape anisotropy, magnetization tends to stay along the film plane only with a small inclination. However, the signal disappears at $\theta_H = 0°$, due to the the relation $V_{ISHE} \propto |\mathbf{J}_s \times \sigma|$. When the precession axis of the magnetization in Py layer is along the normal axis of film plane, the polarization of a spin current σ becomes parallel to the flow direction of the spin current $\mathbf{J}_s$. Therefore, the vector product results $\mathbf{J}_s \times \sigma = 0$. Across $\theta_H = 0°$ electromotive force changes its sign because the spin polarization vector changes its direction. The drastic variation of V_{ISHE} amplitude across $\theta_H = 0°$ is due to the fast-variation of θ_M as shown in figure 2.14.

$$V_{ISHE} \propto \frac{g_r^{\uparrow\downarrow}\gamma^2 h^2 \hbar \sin\theta_M \left[4\pi M_s \gamma \sin^2\theta_M + \sqrt{(4\pi M_s)^2\gamma^2 \sin^4\theta_M + 4\omega^2}\right]}{8\pi\alpha^2 \left[(4\pi M_s)^2\gamma^2 \sin^4\theta_M + 4\omega^2\right]} \tag{4.1}$$

The experimentally obtained V_{ISHE} amplitude was fitted with the equation 4.1 [3] and shown in Fig. 4.6. Here the red line shows the theoretical and the black squares indicate the measured V_{ISHE} amplitudes. The experimental results and theoretical prediction are well comparable and this proves the validity of the ISHE and spin pumping model described in Eqs. 2.7 and 2.22 [3]. The small variation of experimental data from the theoretical value is due to the error in θ_H, since the angle was manipulated by hand.
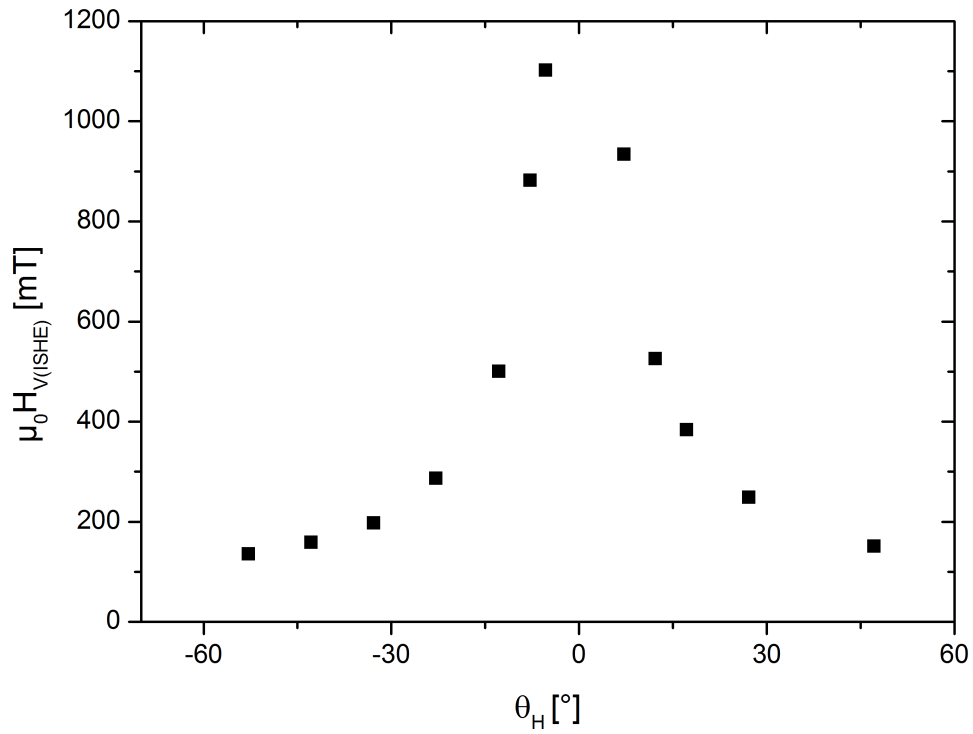
Figure 4.5: θ_H dependence of ferromagnetic resonance field for each V_{ISHE} measurement. This result is consistent with the theory of spin injection through the Pt/Py interface by the ferromagnetic resonance when f_{FMR} and H_{FMR} fulfill the resonance condition. Which means the V_{ISHE} peak positions and H_{FMR} positions coincide.
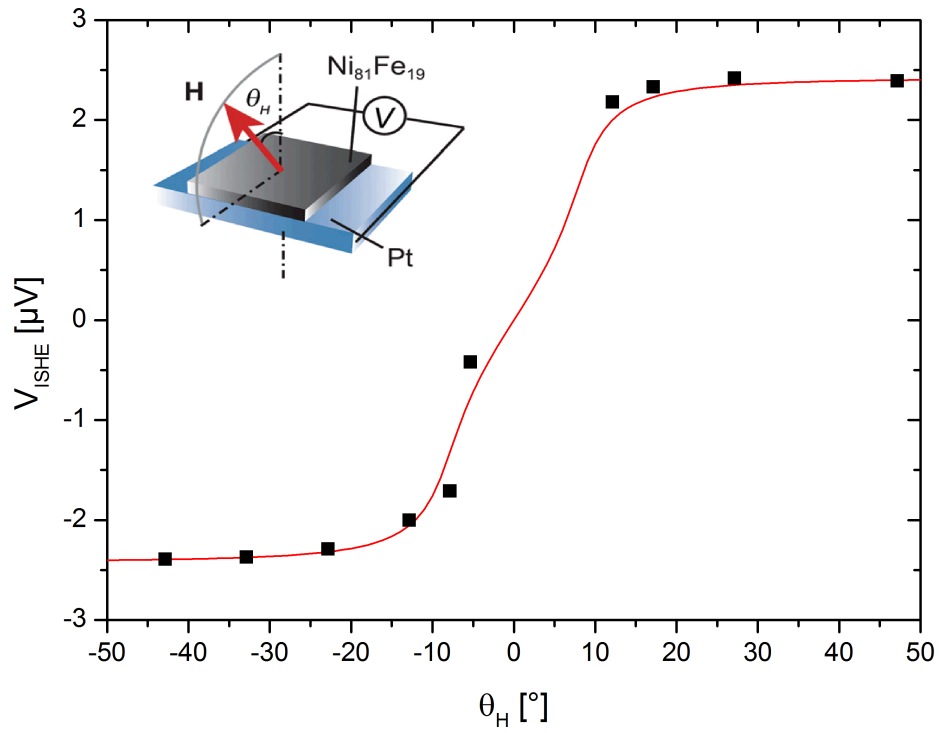
Figure 4.6: The out-of-plane angular dependence of electromotive force measurements where the red line shows the theoretical values obtained from Eq.4.1 and the black squares indicate the measured V_{ISHE} amplitudes. The inset is taken from [3].

4.2 Power dependence of inverse ISHE signal

Figure 4.7 shows the variation of the electromotive force V_{ISHE} with respect to the microwave power. In this measurement the same sample with angular dependence measurement was used. The sample was placed to the center of TE_{102} microwave cavity. During the measurements the temperature was kept constant at $300\,\mathrm{K}$ by a temperature regulator. The sample holder was mounted into a glass tube which was inserted into the cavity for nitrogen gas flow. Even though the same cavity was employed, due to this glass tube the microwave mode inside the cavity was changed to $f = 9.25\ GHz$. We used a signal generator as a microwave source. As a measurement technique, amplitude modulation was employed with $100\ kHz$ modulation frequency and 70% modulation amplitude.
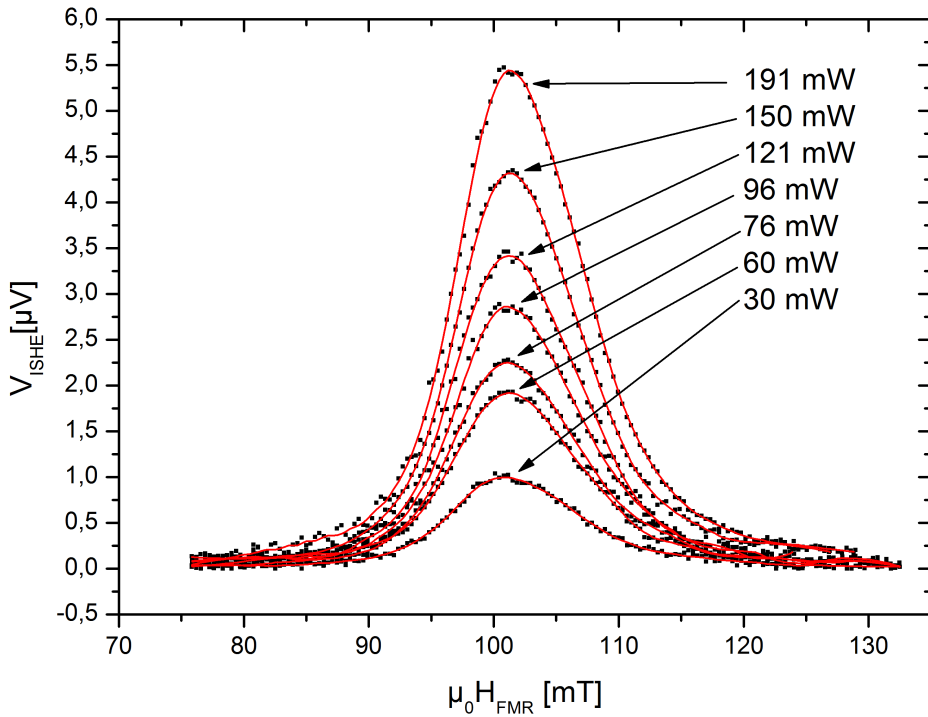
Figure 4.7: The variation of the electromotive force V_{ISHE} with respect to the microwave power. The red line obtained by averaging nearest 5 data points.

As shown in figure 4.7, the magnitude of V_{ISHE} signal increases with increasing microwave power. It is a consistent result with the spin pumping model. Since the cone angle of magnetization precession enlarges with increasing microwave power, therefore

the injected spin current into the paramagnetic layer by spin pumping also increases. projection of Therefore V_{ISHE} also increase with increasing P_{MW}.

In figure 4.8 the microwave power P_{MW} dependence of the electromotive force V_{ISHE} amplitude is shown. The amplitude of V_{ISHE} is estimated as the peak height of the V_{ISHE} spectra shown in Fig. 4.7. The linear dependence of V_{ISHE} on P_{MW}, as shown in figure 4.8, is consistent with the prediction of a direct-current-spin-pumping model [44], [3] as discussed in section 2.2. The dc component of a spin current generated by the spin pumping is proportional to the projection of $\mathbf{m} \times \mathbf{m}/dt$ onto the magnetization precession axis. This projection is proportional to the square of the magnetization-precession amplitude which is proportional to $P_{MW}^{1/2}$. Hence, the induced spin current or the electromotive force due to the ISHE is linearly proportional to the microwave power P_{MW} [3] with a relation $\mathbf{J}_s \propto \mathbf{J}_c \propto V_{ISHE} \propto P_{MW}$.
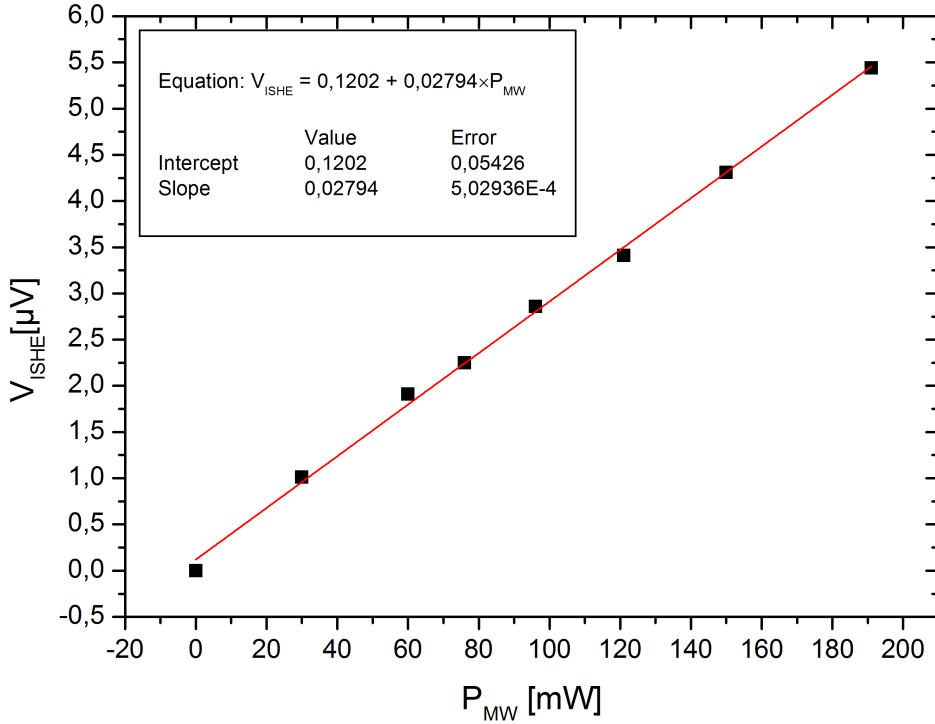
Figure 4.8: The microwave power P_{MW} dependence of the electromotive force V_{ISHE}. The magnitude of V_{ISHE} signal increases linearly with P_{MW}.

4.3 Frequency dependence of inverse ISHE signal

Frequency dependence of V_{ISHE} measurements were performed with a sample comprising a 12 nm Pt and a 12 nm Py layer. The layers were patterned on thermally oxidized Si substrate by electron beam lithograph and the films were deposited via electron beam evaporation. The difference of this measurement from the angular, temperature or the microwave power dependence measurements is the microwave excitation was provided by a semi-rigid cable. So the microwave cavity was not used. The sample was placed very close to a microstrip-microwave guide. During the measurements 60 to 191 mW microwave excitation with frequency f was generated by a signal generator and V_{ISHE} signal was measured by a lock-in amplifier. The modulated quantity was the microwave amplitude thus the reference signal for lock-in amplifier was taken from the signal generator. An external magnetic field H along the film plane was applied perpendicular to the direction across the electrodes. All the measurements were performed at room temperature. The V_{ISHE} between the electrodes attached to the Pt layer was measured electrically as a function of applied magnetic field. As it is shown in Fig. 4.9, the electromotive force peak position was moved with increasing frequency and the amplitude increased with increasing microwave power P_{MW}.

The noise on the spectra are relatively higher compare to the previous measurements. This is because of the microwave cable. In microwave cavity resonance frequency is stable but in rf-cable, several other frequencies also exist close to the resonance frequency. In order to avoid any measurement mistake or other contributions on experimental data, we have performed measurements for each frequency with three different microwave power. Similar spectral shape of each measurements with different P_{MW} proofs that the spectral shape of V_{ISHE} can be well reproduced.

We have performed the measurements in the frequency range 8 to 12 GHz. For each frequency, peaks occurred in different applied fields. This is consistent with the Kittel's formula [17],

$$\omega = \gamma\mu_0\sqrt{H_{FMR}(H_{FMR} + M_{eff})} \tag{4.2}$$

where γ is the gyromagnetic ratio of the bilayer system. The resonance field position is gradually shifted with the rising frequency as shown in figure 4.11 because the resonance the microwave frequency depends on the Larmor frequency of film magnetization. For the Py/Pt system, the gyromagnetic ratio is modified by g-factor. The g-factor for
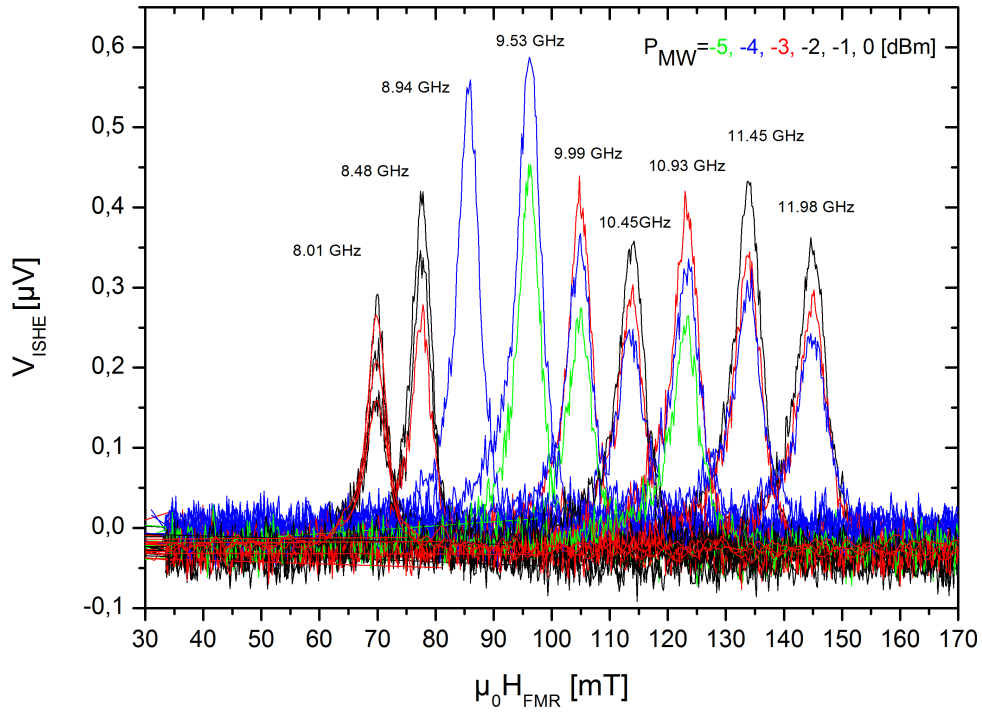
Figure 4.9: The frequency dependence of V_{ISHE} under different microwave power. Each color represents different power that shown at the upper right corner of the graph. By increasing the frequency peak positions on the magnetic field axis shift. Here the applied microwave powers are shown in dBm units and-5, -4, -3, -2, -1, and 0 dBm power correspond to 60,9, 76,5, 96,2, 121, 151 and 191 mW respectively. However, because the distance between the film and strip line was not known, the real power applied on Py is less than actual output power.
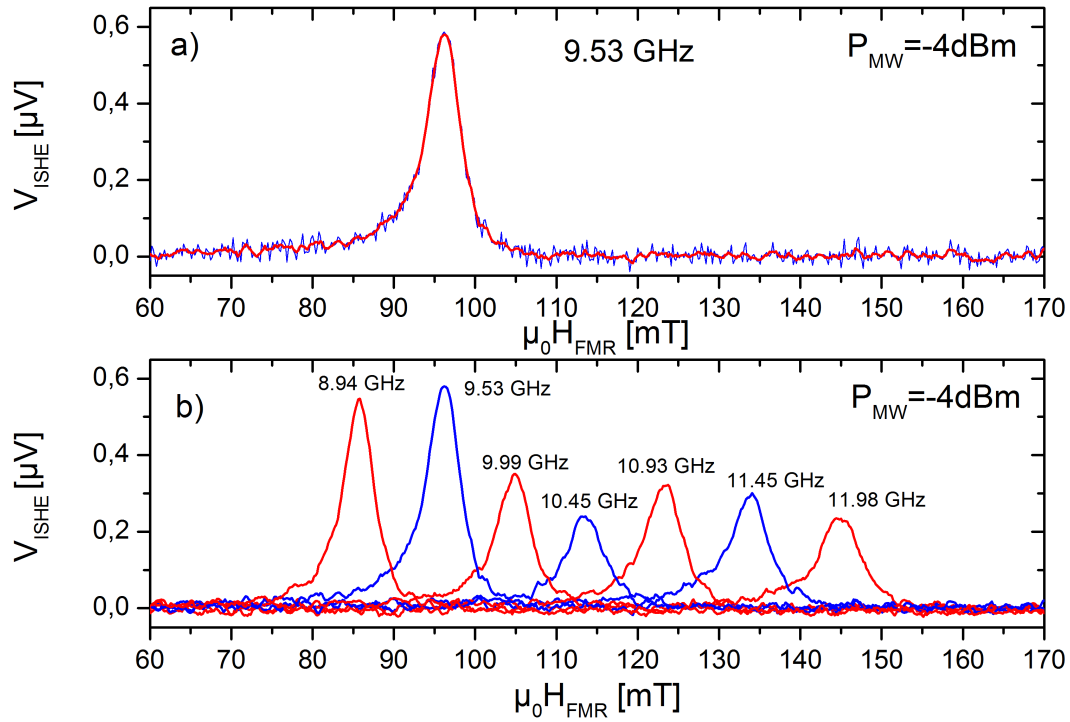
Figure 4.10: a) The blue line shows the measured V_{ISHE} signal under -4 dBm P_{MW} and the red line is the smoothed form. Due to the internal properties of the microwave cable there is a relative high noise in the signal compare to the other measurements that were dne with microwave cavity. By averaging nearest five data point we were able to reduce the noise on the base line without affecting the peak height. b) Seven measurement that were taken under different microwave irradiation frequencies under -4 dBm power. All spectra were smoothed.

bulk permalloy with 78% Ni concentration was reported as $g = 2.1$ [24]. However in our system, underlying Pt layer increases this value. Pt has large spin orbit coupling, and this spin orbit coupling induces interface magnetic anisotropy which is a consequence of the fact that surface atoms are located in a different environment than the bulk ones [10]. Therefore, g-factor at the interface of Py/Pt is considered to be larger as inside Py [26]. The g-factor was reported as $g = 2.115$ for a Pt/Py film with $10\,nm$ Py thichness by Mizukami and coworkers [26]. We fit the experimental frequency vs. resonance field values by the Kittel's formula (equation 4.2) by taking M_{eff} as a fit parameter. We assumed that the V_{ISHE} peaks coincide with the ferromagnetic resonance fields. From the fit, for this g-factor value, the effective magnetization was obtained as $780670\,A/m$ which corresponds to $\mu_0 M_{eff} = 0.98\,T$, which is an acceptable value for the Py film. With this fitting, we observed the deviation of Py/Pt g-factor from the bulk Py value.

With increasing microwave frequency the spin current and thus the electromotive force V_{ISHE} increases under the same P_{MW} and decreases lately. The variation of V_{ISHE} amplitude is shown in figure 4.12. The decrease in V_{ISHE} amplitude is explained by the compensation between the magnetization-precession frequency and the spin current generated by a cycle of the magnetization precession j_s^1 [17, 45]. Since j_s^1 is proportional to the area of magnetization-precession trajectory S. At higher ferromagnetic resonance frequencies, S decreases. This is due to the decrease in magnetization precession cone angle which is caused by the increase in the ferromagnetic resonance field H_{FMR}. As a result for the Py/Pt bilayer that we used in the measurements, with larger microwave frequencies the spin-current density decreases slightly.

Moreover, the microwave setup has a small frequency dependent amplitude contribution which is most probably responsible for the deviation from the expected linear decrease of V_{ISHE} amplitude.
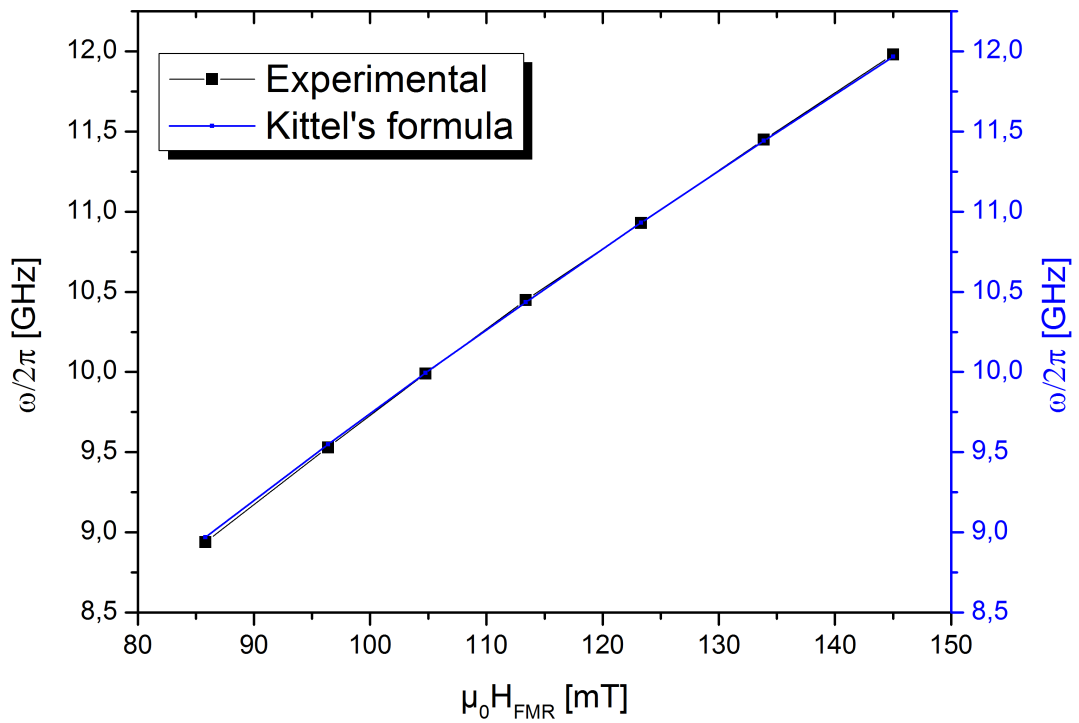
Figure 4.11: Here the dependency of ferromagnetic resonance frequency on resonance field is depicted. The black squares represents the experimental data and the blue solid line was obtained from the Kittel's function. The positions of f_{FMR} and H_{FMR} are in good agreement with the equation (4.2) when the the effective magnetization and g-factor of the film system are assumed to be $780670\,A/m$ and $g = 2.115$, respectively.
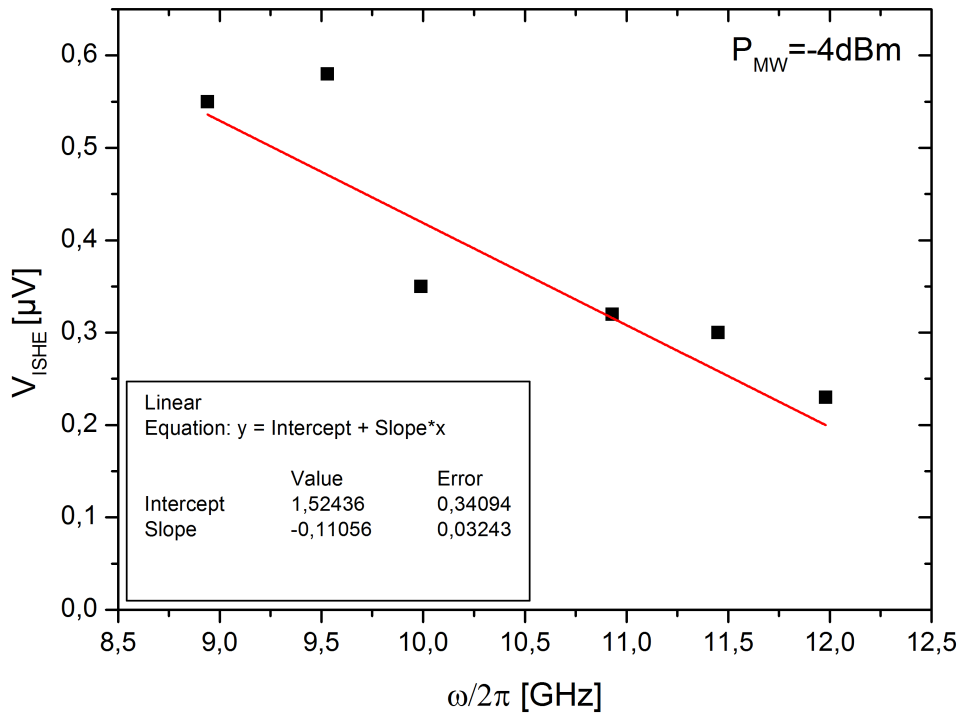
Figure 4.12: V_{ISHE} magnitude decreases with increasing ferromagnetic resonance frequency f_{FMR}. The black squares represents the experimental data that has been taken under -4 dBm microwave power and the red solid line is the linear fit. The V_{ISHE} values were calculated as a peak height of electromotive force spectra from the base line.

4.4 Temperature dependence of inverse ISHE signal

The temperature dependence of electromotive force V_{ISHE} was measured for Pt/Py bilayer film. In the power dependence of V_{ISHE} measurement, the same sample with angular dependence measurement was used. Two electrodes were attached to the both ends of the Pt layer as shown in figure 3.13. The sample was placed near the center of TE_{102} microwave cavity. As a microwave source, a signal generator was used and V_{ISHE} signal measured by lock-in amplifier under 96,2 mW microwave power. The modulated quantity was the microwave amplitude thus the reference signal for lock-in amplifier was taken from the signal generator. During the measurement, the microwave mode with the frequency $f = 9,25\,GHz$ was existed in the cavity. The external field was applied parallel to the film and perpendicular to the electrodes and this orientation was not changed during the measurements.
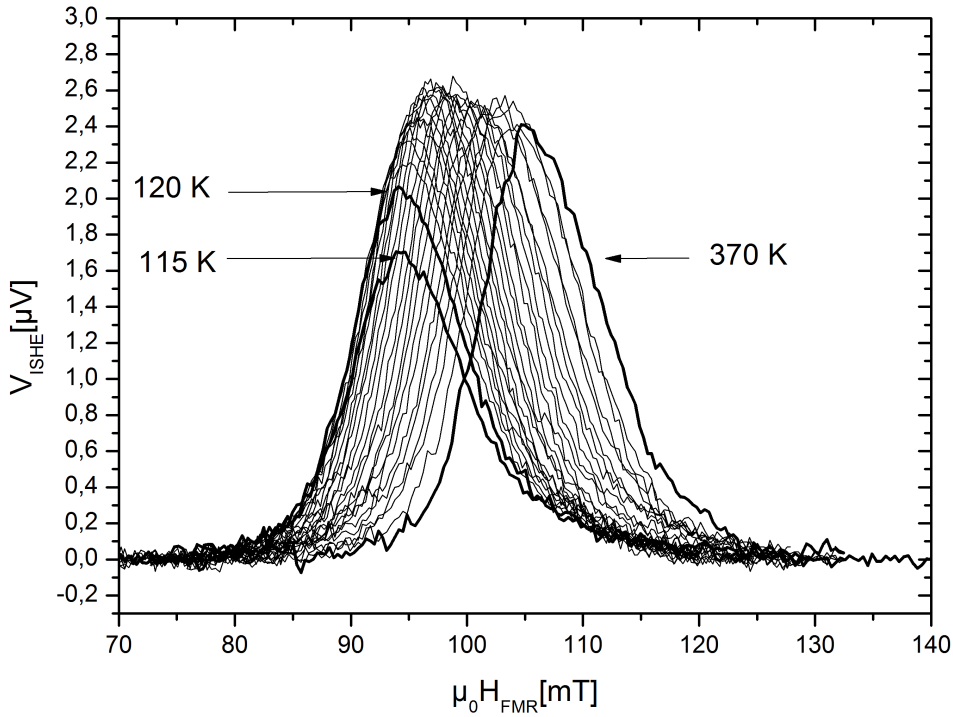
Figure 4.13: The temperature dependence of the electromotive force V_{ISHE} of Pt/Py metallic bilayer is shown. Each spectra was taken in a different temperature. The first, second and the last measurement temperatures were highlighted on the graph. V_{ISHE} signal was measured with 10 K steps between 120 K and 370 K.

V_{ISHE} was measured with increasing temperature in a range from $115\,K$ to $370\,K$ with $10\,K$ steps. The variation of V_{ISHE} signal as a function of temperature is shown in Fig. 4.13.
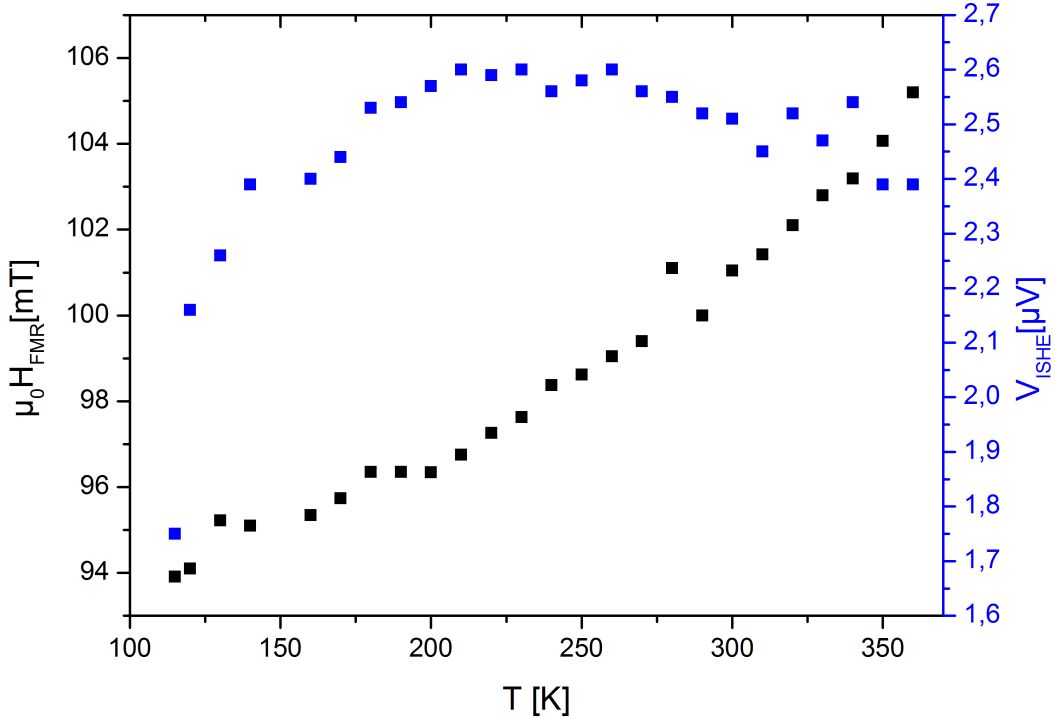
Figure 4.14: The blue data points indicate the V_{ISHE} amplitudes and the black points show the magnetic field position of corresponding peaks as a function of temperature.

In Fig. 4.14, the amplitude of the ISHE signal and the peak-applied field positions are plotted for the Py/Pt sample as a function of temperature. At low temperatures V_{ISHE} is significantly low. With the knowledge of the temperature dependence of skew scattering mechanism, the variation of V_{ISHE} amplitude as a function of temperature is consistent with the extrinsic scenario of the ISHE, in which the inelastic scattering of conduction electrons, including the electron scattering due to phonons, is incapable of generating a Hall voltage [49]. Because at these temperatures, phonons and other fluctuations are less active due to lower thermal energies. With increasing the temperature, the electromotive force amplitude increases at the beginning and around $200\,K$ becomes nearly constant. Afterwards, it drops slightly until the room temperature and above the room temperature fluctuates. By increasing the temperature to the Currie temperature,

the V_{ISHE} signal is expected to decrease and finally disappear. Because beyond that temperature the Py turns into paramagnet, thus cannot produce any spin current.

The applied field positions of the electromotive force peaks are also shifted as shown in figure 4.14. Because the amplitude of the magnetization vector decreases with increasing temperature due to the fluctuations of spins caused by thermal energy. As a result, for higher Larmor frequency higher applied fields are needed. Therefore, peak positions moves with increasing temperature.

5 Conclusion and outlook

The aim of this work was an electrical detection of an electromotive force V_{ISHE} induced by the spin pumping by the ferromagnetic resonance of a $Ni_{81}Fe_{19}$ film attached to a Pt film. The charge current in Pt layer is generated perpendicular to the magnetization direction of the $Ni_{81}Fe_{19}$ layer, and was detected by two electrodes attached to both ends of the Pt layer. The content and conclusions are summarized below:

- The theory part, starts with a brief introduction to the magnetization dynamics. Then, the spin current generation by the spin pumping mechanism in ferromagnetic-paramagnetic bilayer systems was discussed. Later on, the interactions on a charge current in paramagnetic medium namely, skew scattering and side jump mechanisms that are originated from the spin orbit interaction were shown. As these interactions produce a transverse spin current from a charge current (spin Hall effect), this lead us to the inverse process of spin Hall effect (ISHE). Finally some variables which have influences on the inverse spin hall effect induced charge current, such as applied microwave power, angular variation of dc field and film thickness, were discussed. In this chapter we have also shown the FMR linewidth enhancement of Py films with Pt capping layer. This enhancement was the proof of an spin-angular momentum transfer from Py layer into Pt, in other words: spin pumping.

- For the best possible electrical detection of the V_{ISHE} signal, the Py/Pt film system was optimized. The bilayer system was structured with metal masks or EBL method and evaporated via electron beam evaporation. For film fabrication, an additional shutter into the electron beam evaporation chamber was installed. This shutter provided evaporation of Py layer of the samples with and without Pt capping layer simultaneously. The effect of substrates (Si and GaAs) on ISHE was analyzed and no difference was observed. New sample holders and a sample stage for cavity and for multifrequency measurements were produced. These sample holders allowed us to perform electrical detection of the V_{ISHE} signal by employing lock-in technique. As a cavity, due to the optimal field distribution for the electrical detection, TE_{102} microwave cavity was utilized. By placing the disconnected

electrodes into the center of this cavity non-existence of any electric field which might have influence on the V_{ISHE} signal, was confirmed. All the measurements were performed in a conventional FMR setup which was modified intentionally for this measurement purposes.

- The ISHE induced charge current $\mathbf{J}_c$ is proportional to $\mathbf{J}_s \times \sigma$ where $\mathbf{J}_s$ and σ are the spatial direction of the spin current and the spin-polarization vector of the spin current, respectively. $\mathbf{J}_s$ directed perpendicular to the Pt/Py interface, thus the direction of $\mathbf{J}_c$ is defined by the σ which is align with magnetization precession axis. Therefore, by conventional FMR, the out-of-plane magnetic field angle dependence of the magnetization was measured. The deviation of magnetization precession axis from the effective magnetic field due to the anisotropies in Permalloy layer was observed. These results were used to calculate the out-of-plane magnetic field angle dependence of the V_{ISHE} amplitude. With the modified FMR setup, the out-of-plane magnetic field angle dependence of V_{ISHE} amplitude was measured. The theoretical and the experimental values were compared. A good agreement between these two proves the validity of the spin pumping mechanism and the ISHE model.

- According to the direct-current-spin-pumping model, the dc component of a spin current generated by the spin pumping is proportional to the projection of $\mathbf{m} \times d\mathbf{m}/dt$ onto the magnetization precession axis. The amplitude of the projection increases with increasing microwave power due to an increase in magnetization precession cone angle. The V_{ISHE} signal was measured under several applied microwave powers. Consistent with the theory, it was found that the amplitude of V_{ISHE} amplitude is linearly proportional to the applied microwave power.

- By increasing microwave frequency, it is expected that the magnetization precession trajectory is reduced due to the required higher resonance fields. The expected consequence of a smaller magnetization precession trajectory is a decrease in spin pumping. The frequency dependence of V_{ISHE} in a Pt/Py film using the inverse spin-Hall effect was measured and a gradual decrease in V_{ISHE} amplitude was observed. This is consistent with the theoretical expectation.

- The SHE is known to be a temperature dependent effect as a result ISHE is as well. The temperature dependence of these effects is related to the temperature dependence of skew scattering mechanism which is simply an electron scattering mechanism. A simple explanation of this behavior can be seen through electron

scatterings caused by phonons. At lower temperatures, due to less thermal energy, phonons are suppressed. Therefore, less scattering events occur and thus less charge current is produced from the spin current. In order to examine this behavior, the temperature dependence of V_{ISHE} signal was measured. For Pt/Py system, from $115\,\mathrm{K}$ to $200\,\mathrm{K}$ an increase in V_{ISHE} signal was observed. The amplitude of the signal decreased slightly until room temperature and then fluctuated. The decrease in amplitude is believed to be due to the reduction of magnetization amplitude which is related to the the increase in thermal energy in ferromagnet.

The ISHE very fresh and newborn research field. The unique property of the generating a charge current from a pure spin current makes the ISHE a distinct method to investigate the spin current related phenomenons. The effect required only a ferromagnetic and a paramagnetic layers. The ferromagnetic layer must not necessarily be a metallic ferromagnet. Therefore, by using a ferromagnetic insulator any possible anomalous Hall effect contribution, if there is, might be eliminated. A ferromagnetic insulator might also avoid any electric field related noise originated by ferromagnetic layer. Moreover, by optimizing the spin pumping efficiency, and the spin current to charge current conversion efficiency, one can produce higher charge currents. This can be supplied by better engineered thin-film systems. The giant SHE was already reported in a modified paramagnetic layers, by using this layers the ISHE might be enlarged. Moreover, for higher spin pumping efficiencies, an epitaxially grown single-crystalline bilayer systems can be suggested in which the ferromagnetic-paramagnetic interface is far more ordered.

Acknowledgements

I would like to thank the following people who supported me during my work:

6 Bibliography

[1] A. and Fert. Transport in magnetic alloys: Scattering asymmetries (anisotropic scattering, skew scattering, side-jump). Physica B+C, 86-88, Part 1(0):491 – 500, 1977.

[2] K. Ando, Y. Kajiwara, S. Takahashi, S. Maekawa, K. Takemoto, M. Takatsu, and E. Saitoh. Angular dependence of inverse spin˘hall effect induced by spin pumping investigated in a $ni_{81}fe_{19}$/Pt thin film. Phys. Rev. B, 78:014413, Jul 2008.

[3] K. Ando, S. Takahashi, J. Ieda, Y. Kajiwara, H. Nakayama, T. Yoshino, K. Harii, Y. Fujikawa, M. Matsuo, S. Maekawa, and E. Saitoh. Inverse spin-hall effect induced by spin pumping in metallic system. Journal of Applied Physics, 109(10):103913, 2011.

[4] K. Ando, T. Yoshino, and E. Saitoh. Optimum condition for spin-current generation from magnetization precession in thin film systems. Applied Physics Letters, 94(15):152509, 2009.

[5] S.D. Bader and S.S.P. Parkin. Spintronics. Annual Review of Condensed Matter Physics, 1(1):71–88, 2010.

[6] L. Berger. Side-jump mechanism for the hall effect of ferromagnets. Phys. Rev. B, 2:4559–4566, Dec 1970.

[7] Frei Universitaet Berlin. Ferromagnetic resonance (fmr), 2012.

[8] F. Bloch. Nuclear induction. Phys. Rev., 70, October 1946.

[9] P. W. Brouwer. Scattering approach to parametric pumping. Phys. Rev. B, 58:R10135–R10138, Oct 1998.

[10] Patrick Bruno. Dipolar magnetic surface anisotropy in ferromagnetic thin films with interfacial roughness. Journal of Applied Physics, 64(6):3153–3156, 1988.

[11] K.H.J. Buschow. Magnetic and Superconducting Meterials. Elsevier, 2005.

[12] Piers Coleman. Lending an iron hand to spintronics. Physics, 2:6, Jan 2009.

[13] M. V. Costache, S. M. Watts, C. H. van der Wal, and B. J. van Wees. Electrical detection of spin pumping: dc voltage generated by ferromagnetic resonance at ferromagnet/nonmagnet contact. Phys. Rev. B, 78:064423, Aug 2008.

[14] Hans-Andreas Engel, Emmanuel I. Rashba, and Bertrand I. Halperin. Theory of spin hall effects in semiconductors, 2007.

[15] K. Wagner L. Gathmann R. Narkowicz H. Zähres B. R. Salles P. Torelli R. Meckenstock J. Lindner M. Farle F. M. Römer, M. Möller. In situ multifrequency ferromagnetic resonance and x-ray magnetic circular dichroism investigations on fe/gaas(110): Enhanced g-factor. Applied Physics letters, 2012.

[16] Guang-Yu Guo, Sadamichi Maekawa, and Naoto Nagaosa. Enhanced spin hall effect by resonant skew scattering in the orbital-dependent kondo effect. Phys. Rev. Lett., 102:036401, Jan 2009.

[17] Kazuya Harii, Toshu An, Yosuke Kajiwara, Kazuya Ando, Hiroyasu Nakayama, Tatsuro Yoshino, and Eiji Saitoh. Frequency dependence of spin pumping in pt/y[sub 3]fe[sub 5]o[sub 12] film. Journal of Applied Physics, 109(11):116105, 2011.

[18] S. Hikino and S. Yunoki. Anomalous enhancement of spin hall conductivity in a superconductor/normal-metal junction. Phys. Rev. B, 84:020512, Jul 2011.

[19] J. E. Hirsch. Spin hall effect. Phys. Rev. Lett., 83:1834–1837, Aug 1999.

[20] Axel Hoffmann. Pure spin-currents. physica status solidi (c), 4(11):4236–4241, 2007.

[21] Y. K. Kato, R. C. Myers, A. C. Gossard, and D. D. Awschalom. Observation of the spin hall effect in semiconductors. Science, 306(5703):1910–1913, 2004.

[22] Jun Kondo. Anomalous hall effect and magnetoresistance of ferromagnetic metals. Progress of Theoretical Physics, 27(4):772–792, 1962.

[23] L. Landau and E. Lifshitz. On the theory of the dispersion of magnetic permeability in ferromagnetic bodies. Physikalische Zeitschrift der Sowjetunion, 8:153–169, 1935.

[24] Z. Frait M. Ondris. Ferromagnetic resonance in thin permalloy films. Czech.J.PHYS.B, 11:883–885, 1961.

[25] S. Mizukami, Y. Ando, and T. Miyazaki. Effect of spin diffusion on gilbert damping for a very thin permalloy layer in cu/permalloy/cu/pt films. Phys. Rev. B, 66:104413, Sep 2002.

[26] Shigemi Mizukami, Yasuo Ando, and Terunobu Miyazaki. The study on ferromagnetic resonance linewidth for nm/80nife/nm (ta, pd and pt) films. Japanese Journal of Applied Physics, 40(Part 1, No. 2A):580–585, 2001.

[27] O. Mosendz, V. Vlaminck, J. E. Pearson, F. Y. Fradin, G. E. W. Bauer, S. D. Bader, and A. Hoffmann. Detection and quantification of inverse spin hall effect from spin pumping in permalloy/normal metal bilayers. Phys. Rev. B, 82:214403, Dec 2010.

[28] O. Mosendz, V. Vlaminck, J. E. Pearson, F. Y. Fradin, G. E. W. Bauer, S. D. Bader, and A. Hoffmann. Detection and quantification of inverse spin hall effect from spin pumping in permalloy/normal metal bilayers. Phys. Rev. B, 82:214403, Dec 2010.

[29] Naoto Nagaosa. Anomalous hall effect —a new perspective—. Journal of the Physical Society of Japan, 75(4):042001, 2006.

[30] Naoto Nagaosa, Jairo Sinova, Shigeki Onoda, A. H. MacDonald, and N. P. Ong. Anomalous hall effect. Rev. Mod. Phys., 82:1539–1592, May 2010.

[31] Naoto Nagaosa, Jairo Sinova, Shigeki Onoda, A. H. MacDonald, and N. P. Ong. Anomalous hall effect. Rev. Mod. Phys., 82:1539–1592, May 2010.

[32] H. Nakayama, K. Ando, K. Harii, Y. Kajiwara, T. Yoshino, K.-i. Uchida, and E. Saitoh. Inverse spin-hall effect induced by spin pumping in different thickness pt films. Magnetics, IEEE Transactions on, 46(6):2202 –2204, june 2010.

[33] The Univetsity of Sceffield. Electron beam lithography, 2012.

[34] A. Pályi and J. Cserti. Skew scattering due to intrinsic spin-orbit coupling in a two-dimensional electron gas. Phys. Rev. B, 76:035331, Jul 2007.

[35] Oliver Posth. Spin-transfer-torque in ferro/nichtferromagnetischen saeulenstrukturen. 2010.

[36] Emerson M. Pugh. Hall effect and the magnetic properties of some ferromagnetic materials. Phys. Rev., 36:1503–1511, Nov 1930.

[37] N. Reckers, J. Cucchiara, O. Posth, C. Hassel, F. M. Römer, R. Narkowicz, R. A. Gallardo, P. Landeros, H. Zähres, S. Mangin, J. A. Katine, E. E. Fullerton, G. Dumpich, R. Meckenstock, J. Lindner, and M. Farle. Effect of microwave irradiation on spin-torque-driven magnetization precession in nanopillars with magnetic perpendicular anisotropy. Phys. Rev. B, 83:184427, May 2011.

[38] Florian M. Römer. Breitbandige in situ Ferromagnetische Resonanz und niederfrequente Suszeptibilitätsmessungen an Eisen auf III-V Halbleitern. PhD thesis, Der Fakultät Physik der Universität Duisburg-Essen, Duisburg, Germany, 2012.

[39] E. Saitoh, M. Ueda, H. Miyajima, and G. Tatara. Conversion of spin current into charge current at room temperature: Inverse spin-hall effect. Applied Physics Letters, 88(18):182509, 2006.

[40] Hasegawa Yu Mitani Seki, Takeshi. Giant spin hall effect in perpendicularly spin-polarized fept/au devices. Nat Mater, 7:125–129, Feb 2008.

[41] Janine Splettstoesser, Michele Governale, and Jürgen König. Adiabatic charge and spin pumping through quantum dots with ferromagnetic leads. Phys. Rev. B, 77:195320, May 2008.

[42] Qing-feng Sun and X. C. Xie. Definition of the spin current: The angular spin current and its physical consequences. Phys. Rev. B, 72:245305, Dec 2005.

[43] Saburo Takahashi and Sadamichi Maekawa. Spin current, spin accumulation and spin hall effect. Sci. Technol. Adv. Mater., 9:11, March 2008.

[44] Yaroslav Tserkovnyak, Arne Brataas, and Gerrit E. W. Bauer. Enhanced gilbert damping in thin ferromagnetic films. Phys. Rev. Lett., 88:117601, Feb 2002.

[45] Yaroslav Tserkovnyak, Arne Brataas, and Gerrit E. W. Bauer. Spin pumping and magnetization dynamics in metallic multilayers. Phys. Rev. B, 66:224403, Dec 2002.

[46] KOONG CHEE WENG. SPIN-ORBIT INTERACTION INDUCED SPIN-SEPARATION IN PLATINUM NANOSTRUCTURES. PhD thesis, National University of Singapore, 2009.

[47] Lalani K. Werake, Brian A. Ruzicka, and Hui Zhao. Observation of intrinsic inverse spin hall effect. Phys. Rev. Lett., 106:107205, Mar 2011.

[48] S. A. Wolf, D. D. Awschalom, R. A. Buhrman, J. M. Daughton, S. von Molnár, M. L. Roukes, A. Y. Chtchelkanova, and D. M. Treger. Spintronics: A spin-based electronics vision for the future. Science, 294(5546):1488–1495, 2001.

[49] K Sasage Y Kajiwara, K Ando and E Saitoh. Spin pumping and spin-hall effect observed in metallic films. Journal of Physics: Conference Series, 150:042080, 2009.

Hiermit erkläre ich, dass ich die Arbeit selbstständig verfaßt, Zitate kenntlich gemacht und keine anderen als die hier angegebenen Quellen und Hilfsmittel benutzt habe.

Duisburg, den 07.März 2012